UNIVERSIDADE DE SÃO PAULO
INSTITUTO DE FÍSICA DE SÃO CARLOS

Luiz Henrique Bugatti Guessi

Linear and non-linear transport properties of quantum-dot devices

São Carlos

2021

Luiz Henrique Bugatti Guessi

Linear and non-linear transport properties of quantum-dot devices

Thesis presented to the Graduate Program in Physics at the Instituto de Física de São Carlos, Universidade de São Paulo, to obtain the degree of Doctor in Science.

Concentration area: Basic Physics

Supervisor: Prof. Dr. Luiz Nunes de Oliveira
Co-supervisor: Prof. Dr. Antonio Carlos Ferreira Seridonio

Corrected version
(original version available on the Program Unit)

São Carlos
2021

Guessi, Luiz Henrique Bugatti
Linear and non-linear transport properties of quantum-dot devices / Luiz Henrique Bugatti Guessi; advisor Luiz Nunes de Oliveira; co-advisor Antonio Carlos Ferreira Seridonio - corrected version -- São Carlos 2021.
118 p.

Thesis (Doctorate - Graduate Program in Basic Physics) -- Instituto de Física de São Carlos, Universidade de São Paulo - Brasil , 2021.

1. Bound state in the continuum. 2. Kondo effect. 3. Two channel Kondo effect. 4. Numerical renormalization group. 5. Density matrix renormalization group. I. Oliveira, Luiz Nunes de, advisor. II. Seridonio, Antonio Carlos Ferreira, co-advisor. III. Title.

To my dear wife Sibeli Ap. de Souza Cruz.

ACKNOWLEDGEMENTS

I would like to start expressing my gratitude to my supervisor, Prof. Luiz Nunes de Oliveira. Along these five years, I truly appreciate all our physical discussions. Thanks to them, I evolved professionally and personally in such a way that I've never imagined. I thank you too for you always challenge and believe on me. I will never forget my first five-minute lesson about python in your blackboard, the simple way that you explain complex problems and connect them to everyday problems via analogies. All of these helped me to spread my wings and set fly to new horizons.

I would like to thank my co-supervisor Antonio Carlos Ferreira Seridonio for motivate me to keep investigating condensed matter problems in my undergrad course, my master degrees and now in my PhD. Your orientation changed my life and made me persist following my dreams.

I would like to thank Prof. Harold U. Baranger for host me at Duke University for a whole year. The internship was a unique experience that made me grow personally and professionally. I will never forget all our physical discussion and everything that you taught me. Although you are not formally linked to this thesis, I consider you as my second co-supervisor.

I also would like to thank Prof. Thomas Barthel for all our discussion about Density Matrix Renormalization group (DMRG) and the opportunity to use his DMRG code. This collaboration allowed me to perform the time-dependent numerical calculations presented in this thesis and showed me a new world of high-performance codes in a cluster environment.

I could not forget to thank Prof. Juarez L. F. Da Silva and QTNano Group. I've learned a lot about Density Function Theory and Quantum Chemistry along QTNano group meetings. The short collaboration with the group allowed me to improve my programming skills, expand my vision about numerical calculations and discover a new world about supercomputers.

My deepest thanks to Krissia Zawadzki and Celso Rego. I cannot express my gratitude for the way that you welcomed me at the beginning of my PhD. In addition, I would like to thank all your support, advice and friendship until today. Of course, I could not forget our physical discussions and our long chats in the tea time on sunny Brazilian summer afternoons. In special, I would like to thank Krissia for all her patience and support along the first months of my PhD. Without that, I would probably take two or even three times longer to implement my first NRG code. I hope to keep in touch and collaborate with both of you soon.

I would like to thank Xin Zang, Alexey Bondarev (The Pilot) and Moritz Binder for welcome and support at Duke University. I also have to thank for all your formal physical discussion in the office and the informal ones along the coffee time and in the group meetings. Particularly, I want to thank Moritz to introduce me to a very nice social group which helped me a lot to develop my communication skills and refreshing my mind after intense hours of works.

I would like to express my gratitude to Diego Guedes-Sobrinho, Naidel Caturello, Carlos M. O. Bastos, Luciana Reis, Vinicius Aurichio, Nícolas Morazotti, João V. Costa, Julian Zanon and Ronaldo Araújo that directly or indirectly supported me along my PhD. See all these names together brings me up a mix of memories that goes from physics to philosophy at different levels of consciousness. I will never forget all the support with endless exercise lists, all the group meeting, the physical discussion about Density Functional Theory, Solid-State and Many-Body physics, the compilation problems with LAPACKE and VASP, the physical discussion about fundamental concepts and many other things.

I have to thank my best friend Diego Henrique de Oliveira Machado to be at my side at the hardest moments of my PhD. Without his friendship, I would probably not overcome all my sad moments, my doubts and could not hold on the right path. Definitely, all his support and advices make me strong. Of course, I could not forget our discussions where you share with me your expertise in experimental physics.

I do not have words to express my gratitude for all my family support. I just wanna thanks my mother Maria de Lourdes Bugatti Guessi, my father Luiz Carlos Guessi, my sister Alana Bugatti Guessi and my aunts Joana and Dinalva Ap. Bugatti. I truly believe that they know what I want to express with the simple words “thank you”.

I could not forget to my lovely wife Sibeli Ap. de Souza Cruz that holds my hand since the beginning of my journey in the physics world. I have to thank for your support, your funny way that made me laugh in the most difficult times of my life and keep loving me unconditionally. I cannot express my gratitude for you understand my choice to went to Duke University for a whole year and you stay in São Carlos alone facing unimaginable problems. I will always be grateful for that.

My final thanks go to São Paulo Research Foundation (FAPESP) for the financial support (Grants number: 2015/26655-9 and 2018/10582-0).

"Never give up of your dreams. There is no problem that cannot be overcome with honest, solid and hard work."

ABSTRACT

GUESSI, L. H. **Linear and non-linear transport properties of quantum-dot devices**. 2021. 118p. Thesis (Doctor in Science) - Instituto de Física de São Carlos, Universidade de São Paulo, São Carlos, 2021.

This thesis investigates (i) the correlation effects in the emergence of bound states in the continuum (BIC); and (ii) non-equilibrium effects of the asymmetric two-channel Kondo problem. BICs are discrete states embedded in the continuum. They have localized wave-function and are originated by the quantum interference effects. In the first project of this thesis, we investigate the correlation effects in the emergence of a BIC in a two identical quantum dot device coupled to a quantum wire. This device was modeled by the two-impurity Anderson Hamiltonian and diagonalized via the Numerical Renormalization Group method. Given the symmetry between the quantum dots, the system was projected on the bonding and antibonding orbital representation resulting from the symmetric and antisymmetric combinations of the quantum dots, respectively. In the non-interacting regime, the antibonding orbital is a Friedrich-Wintgen BIC. As the Coulomb interaction grows, the antibonding orbital is indirectly coupled to the continuum via spin-spin and isospin-isospin interactions with the bonding orbital. In addition, at zero-temperature, the Coulomb interaction triggers a quantum phase transition between a magnetic and a non-magnetic phase. The magnetic phase is associated to the emergence of a bound spin state in the continuum (spin-BIC). The phase transition results from competition between a singlet isospin state, formed by the isospin-isospin interaction, and a triplet spin state, formed by the spin-spin interaction, between the two orbitals. The two phases are due to the conservation of the spin of the antibonding orbital. At low temperature, the spin-BIC interacts ferromagnetically with the conduction band, and the interaction renormalizes to zero as $T \to 0$. In the second project of this thesis, motivated by a recent experiment [Z. Iftikhar *et al.*, Nature 526, 233 (2015)], we investigate the transport properties of a macroscopic metallic island coupled to two leads. In the low-energy regime, only two charging states of the island are energetically accessible, which mimic a pseudospin-1/2. The charge fluctuations on the island emulate a spin-flip mechanism. Therefore, the low-energy physics of this device is well described by the anisotropic two-channel Kondo model. To explore the non-linear electronic transport, the system is driven out of equilibrium by the sudden application of a bias voltage between the leads. Time-dependent Density Matrix Renormalization Group computations follow the time evolution of the electrical current for times longer than the transient regime, although not long enough to reach the steady state. In the symmetric-coupling regime, the time-dependent current and differential conductance measurements show the universal behavior of the two-channel Kondo effect. In this limit, the differential conductance scales with the square root of the Kondo temperature and vary with the square of the bias voltage. In the presence of asymmetry, the transient behavior

can be explained via energy-time uncertainty principle. As a function of the bias voltage, the conductance displays the expected crossover from non-Fermi liquid to Fermi-liquid behavior.

Keywords: Bound state in the continuum. Kondo effect. Two channel Kondo effect. Numerical renormalization group. Density matrix renormalization group.

RESUMO

GUESSI, L. H. **Propriedades de transporte linear e não linear em dispositivos de ponto quântico**. 2021. 118p. Tese (Doutorado em Ciências) - Instituto de Física de São Carlos, Universidade de São Paulo, São Carlos, 2021.

Esta tese investiga (i) os efeitos de forte correlação eletrônica na emergência de estados ligado no contínuo (BICs - bound states in the continuum); e (ii) os efeitos de não-equilíbrio no problema Kondo anisotrópico de dois canais. BICs são estados discretos embebidos no contínuo. Eles possuem função de onda localizada e são originados por efeito de interferência quântica. No primeiro projeto desta tese, investigamos os efeitos de correlação eletrônica na emergência de um BIC em um dispositivo de dois pontos quânticos idênticos acoplados a um fio quântico. Esse dispositivo foi modelado pelo Hamiltoniano de Anderson de duas impurezas e diagonalizado pelo grupo de Renormalização Numérico. Dada a simetria entre os pontos quânticos, o sistema foi projetado na representação de orbitais ligante e antiligante obtida pela combinação simétrica e antissimétrica dos pontos quânticos, respectivamente. No regime não interagente, o orbital antiligante é um BIC de Friedrich-Wintgen. Conforme a interação de Coulomb cresce, o orbital antiligante se acopla indiretamente com o contínuo, via interação de spin-spin e isospin-isospin, com o orbital ligante. Além disso, à temperatura zero, o aumento da interação de Coulomb desencadeia uma transição de fase quântica entre uma fase magnética e outra não magnética, sendo o magnetismo resultado da emergência de um estado ligado no contínuo de um único spin (spin-BIC). A transição de fase se deve a competição entre um estado singleto de isospin, formado pela interação isospin-isospin, e um estado tripleto de spin, formado pela interação spin-spin, entre os orbitais. As duas fases refletem a conservação do spin do orbital antiligante. No limite de baixas temperaturas, o spin-BIC interage ferromagneticamente com a banda de condução, mas a interação é renormalizada para zero para $T \to 0$. No segundo projeto, motivado por um experimento recente [Z. Iftikhar *et al.*, Nature 526, 233 (2015)], estudamos o transporte eletrônico em uma ilha metálica macroscópica acoplada a dois terminais. No regime de baixas temperaturas, dois estados de carga da ilha são energeticamente acessíveis, que emulam um pseudo spin-1/2. A flutuação de carga induzida pela transferência de elétrons entre os terminais e a ilha simula um mecanismo de spin-flip. A física de baixas energias desse dispositivo é bem descrita pelo modelo Kondo anisotrópico de dois canais. Para explorar o transporte eletrônico não-linear, o sistema é tirado do equilíbrio pela aplicação repentina de uma diferença de potencial entre os terminais. Cálculos de Grupo de Renormalização da Matriz da Densidade permitem atingir tempos longos o suficiente para descrever o regime de transiente, mas não longo o suficiente para atingir o estado estacionário. Medidas de corrente e condutância diferencial dependente do tempo revelaram um comportamento universal do efeito Kondo de dois

canais. A condutância diferencial escala com a raiz quadrada da temperatura Kondo e varia com o quadrado da diferença de potencial aplicada. Na presença de assimetria de carga, o regime transiente pode ser explicado pela relação de incerteza energia-tempo. A condutância diferencial em função da diferença de potencial mostra um crossover de uma fase de não-líquido de Fermi para uma de líquido de Fermi.

Palavras-chave: Estado ligado no contínuo. Efeito Kondo. Efeito Kondo de dois canais. Grupo de renormalização numérico. Grupo de renormalização da matrix da densidade.

LIST OF FIGURES

LIST OF TABLES

LIST OF ABBREVIATIONS AND ACRONYMS

BIC	Bound state in the continuum
spin-BIC	Bound spin state in the continuum
CD-2CK	Charge-degenerate two channel Kondo
DMRG	Density Matrix Renormalization group
MPO	Matrix product operators
MPS	Matrix product states
NRG	Numerical Renormalization group
RG	Renormalization group
SIAM	Single-impurity Anderson model
tDMRG	Time-dependent Density Matrix Renormalization group
TIAM	Two-impurity Anderson model

CONTENTS

1 INTRODUCTION

The development of nanotechnology has taken semiconductor nanostructures to a level of controllability that allows the experimental materialization of condensed-matter models. For example, Anderson[3] and Kondo[4] models precisely describe the low-energy physics of a single-electron transistor (SET),[5–7] constituted by a central region coupled to metallic terminals. More complex semiconductor nanostructures can probe exotic condensed matter phenomena.[1,8–10] The electronic transport properties of a single-electron transistor count the number of electrons that leave the source, cross a central region and reach the drain. Despite the apparent simplicity of the problem, the experimental and theoretical results cannot be trivially understood. The challenge comes from quantum mechanical effects, i.e., wave interference and the electron-electron interaction.

Interference effects in a SET-like device are usually explained in the framework of Fano theory, which describes the interference among different tunneling paths through a discrete set of states and a continuum.[11,12] Depending on the configuration of the system, the electronic transport can be enhanced or suppressed, due to constructive or destructive interference, respectively. Other non-trivial phenomena are consequences of the electron-electron interaction. At first glance, Coulomb blockade physics seems to provide classical description of the transport properties. However, it fails when higher-order tunneling processes become relevant at low temperature. In special, spin-flip scattering enhances the electronical conductance from near zero to nearly ballistic transport across the central region of a SET, due to the Kondo effect.

In this thesis, we focus on these two phenomena. First, we investigate the effect of the electron-electron interaction upon the emergence of a bound state in the continuum, a physical effect due to interference.[13,14] Second, we focus on the electronic transport properties of a hybrid metal-semiconductor single-electron transistor, which accommodates the charge-degenerate two channel Kondo effect.[1,15]

1.1 Bound state in the continuum

Basic quantum mechanic textbooks share the common wisdom that free particle eigenvalues belong to a continuous spectrum, while bound states form discrete sets.[16–18] Bound state are usually illustrated by the example of a particle in a box. A third class of states comes with partial confinement of an electron, known as resonant states. In this case, the partial electronic confinement acquire a finite lifetime, well described by the Fermi golden rule. Finally, there is a fourth class of state, called bound states in the continuum (BICs), a term that describes the electronic confinement of particles with kinetic energy above the continuum threshold. Even though the last class is less discussed,

recent quantum mechanics textbooks have started to briefly mention it.[19]

In 1929, only three years after the development of the Schrödinger equation, von Newmann and Wigner proved that the wave interference can confine particles with energy above the continuum threshold.[20] Via the potential engineering approach, von Newmann and Wigner found that a damped oscillatory potential can bind a wave function with energy embedded in the continuous, i.e., a bound state in the continuum. Despite purely mathematical, this result hallmarks the search for physical systems that hold a BIC. Motivated by evidences of atomic and molecular systems supporting a BIC, Stillinger and Herrick revisited and generalized the von Newmann and Wigner approach for different classes of potential. In addition, via variational approach, they found a BIC in a two-electron atom.[21] Thereafter, they also independently proposed an epitaxial heterostructure superlattice that would hold a BIC.[22,23] Despite their failed attempt, Capasso *et al.* has been the first to experimentally investigate the existence of BICs in heterostructure superlattice. In fact, Capasso *et al.* observed a bound state. However, it was a positive-energy defect state with energy in the bandgap.[24]

A more practical platform to engineer BICs is constituted by multiple resonances coupled by conduction channels. The main advantage of this platform is the tunability of the physical parameters of the system. Exploring such idea, C. W. Hsu *et al.*[14] have divided the BICs engineered by the perfect interference of resonances into two classes Fabry-Pérot BICs and Friedrich-Wintgen BICs. The former class covers the states generated by the interference of two or more resonances far apart. Due to the perfect reflection among them, the resonances trap waves between them and generate a bound state. The second class also emerges due to wave interference. However, the BIC is now due to a decoupled resonance. Specifically, as the resonances are coupled at the same spot of the continuum, the interference between them broads some resonances and squeezes other. In this platform, BICs emerge for the set of parameters that give rise to completely destructive interference among them.

In mode details, Friedrich-Wintgen BICs can be explained following Ref.[13] In that paper, Friedrich and Wintgen investigates the interference of two resonances spatially coupled to the continuum at the same spot. Fig. 1 shows their main results. In Panel (a), the effective energy of the resonances as a function of the energy difference displays an avoided crossing induces by their coupling via continuum. In addition, Panel (b) shows that while one of the resonance doubles its original breadth, the width of the second one goes to zero at the symmetric point and, hence, defines a BIC.

BICs are a general wave phenomenon that are not restricted to quantum mechanics. They are also observed in classical wave system, such as water waves,[25] acoustic waves[26] and electromagnetic waves.[27] The perfect destructive interference among scattered waves usually happens at the symmetric points. This is the case described by Fabry-Pérot and

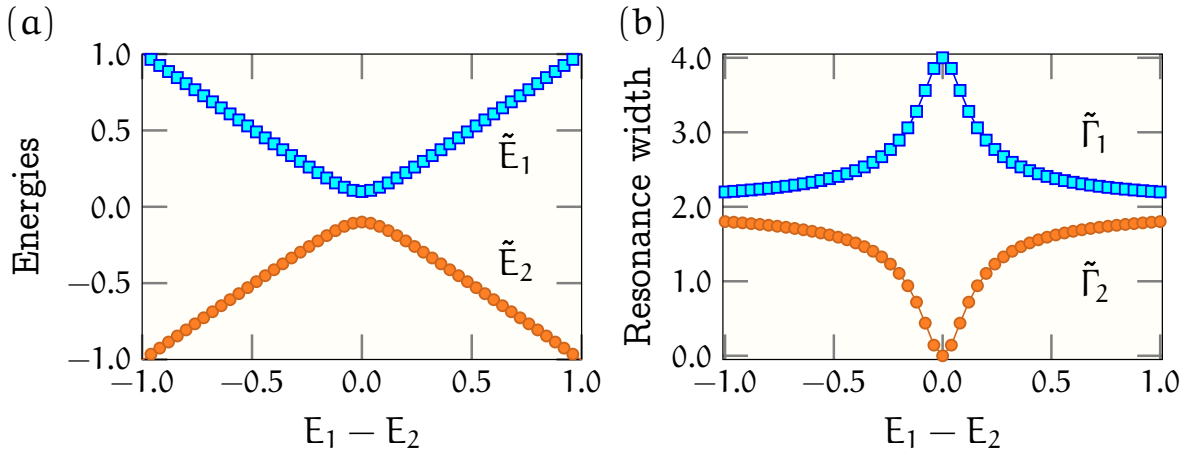

Figure 1 – Panel (a): Effective energies of two interfering resonances as a function of the energy separation $E_1 - E_2$ of the uncoupled resonances. Panel (b): Effective resonance width of two interfering resonances as a function of the energy separation $E_1 - E_2$.
Source: By the author.

Friedrich-Wintgen BICs. In other words, when both resonances are identical, i.e., the system preserves reflection or rotational symmetry, the scattered waves interfere perfectly with each other in such a way to confine waves between them. Out of the symmetric point, BICs leaks to the continuum. These states are also known as symmetry-protected BICs. However, in more complex systems, multiple sources of scattering waves can also generates accidental BICs out of the symmetric point.[28,29] Different from the symmetric-protect BIC, accidental BICs cannot be predicted by simple analyzes.

By definition, bound state are zero-width states, with integrable square wave function and infinite lifetime. Of course, BICs must follow the same definition too, but with energy above the continuum threshold. In this thesis, BICs follow this standard definition. Before processeding, we emphasize that certain authors diverge from the previous definition. Using S-matrix approach, A. K. Jain and C. S. Shastry[30] were the first to highlight that the BIC found by von Newmann and Wigner[20] does not have zero width. Non-zero width BICs have recently been proposed in multi quantum impurity platforms adsorbed in a graphene sheet.[31,32] In these works, the authors investigate the destructive interference between two impurities and, fine-tuning the parameters of the model, they verify the formation of a non-zero width BIC. Another non-zero width BICs are known as quasi-BIC. These states slightly diverges from the standard definition and they appear as very narrow resonant states.[33] The notion of quasi-BICs bring us close to the reality, since it is almost impossible to achieve the perfect conditions for the emergence of a BIC in experiments.

In the last decade, the number of works on BICs has increased exponentially after experimental detection and the applicability of these states in quantum optics and

nanophotonics.[33,34] In both fields, these states are usually known as dark states. Due to their high-quality factor, BICs became a trend topic in nanophotonics[35] and they have been applied in engineering of high intense lasers.[36] These states have also been applied to the engineering of sensors and filters.[14]

BICs have never been experimentally detected in electronic system, such as semiconductor nanostructures. Because of that, our discussion focus only on theoretical works. Seridonio's group[31,32,37–39] and Orellana's group[40–42] have investigated the emergence of BICs in quantum dot and quantum impurity devices. Some of their works also verify the existence of Majorana bound state in the continuum[37,39,43] in a quantum dot device couple to a Kitaev chain. Even though both groups provide insightful discussions about BICs in quantum impurity and quantum dot devices, and discuss a wide range of applications, their results are valid only in the non-interacting regime or in the framework of mean-field approach. To our knowledge, Zitko *et al.* have been the first to verify the existence of a BIC properly considering the Coulomb interaction.[44] Specifically, the authors investigate the electronic properties of a parallel double quantum dot device via Numerical Renormalization Group. As their work has focused on the comparison between the Bethe Anzatz approach and NRG results, they superficially mentioned the existence of a BIC.

Motivated by the recent studies of BICs in quantum dot device and the inaccuracy of the description of the strong correlation effects in these setups, this thesis investigates the influence of strong correlation upon the emergence of BIC. To accomplish this goal, we study the electronic properties of two identical quantum dots coupled to a quantum wire. At low-energy, the electronic properties of the experimental setup is precisely described by the two-impurity Anderson model (TIAM). This is the simplest and most suitable platform to support this study because the TIAM accommodates a Friedrich-Wintgen BIC in the non-interacing regime and allows gradual inclusion of the intra-dot Coulomb interaction.

Exploring inversion symmetry between the quantum-dot orbitals, we rewrite the TIAM Hamiltonian in terms of the bonding and antibonding orbitals defined by the symmetric and anti-symmetric linear combinations of the dots. To monitor the effects of electronic correlation, we calculate the bonding and antibonding spectral densities, which explicitly provides information about the spectrum and lifetimes. In addition, we discuss the magnetic susceptibility of these orbitals. Both quantities were accurately calculated via Numerical Renormalization Group.

Combining the numerical results with Hamiltonian analyses, we have observed, via spectral density calculation that the antibonding orbital, which is a Friedrich-Wintgen BIC in the non-interacting regime, gradually broaden as the Coulomb interaction increases. The antibonding spectral density also displays a threshold behavior that follows the Nozières-De Dominicis and Doniach-Sunjic power laws in the weak and strong coupling regime,

respectively. This mechanism shows us that the ground state of the TIAM Hamiltonian is composed by an isolated component of the antibonding orbital. At zero temperature, the magnetic susceptibility as a function of the Coulomb interaction shows a quantum phase transition from a non-magnetic to a magnetic phase. The phase transition is triggered by the unexpected emergence of a bound spin state in the continuum, which we just call it as spin-BIC. Different from the ordinary BICs, that emerge as a result of interference, the spin-BIC emerges due to correlation.

1.2 Charge-degenerate two channel Kondo problem

Quantum many-body system are fascinating condensed matter problems. As a result of the collective behavior, quasi-particle excitation originates unexpected physical properties entirely different from the initial conditions. For example, certain systems can display phase transition,[45,46] fractional excitations[47–50] and non-Fermi liquid behavior.[51,52]

The Kondo effect is a well-known example of nontrivil many-body system, which has attracted the attention of many scientists. For historical reasons, the Kondo model is offen associated with magnetic impurities. In 1964, J. Kondo showed that, at low temperatures, the spin-flip scattering of the itinerant electron by the magnetic impurities enhances the electronical resistivity of metals.[4,53] Straightforward generalizations of this model allowed investigation of phase transitions,[54,55] fractional excitations[56,57] and non-Fermi liquid behavior.[51,52] For example, in multi-impurity problems, the competition between the antiferromagnetic coupling among the local moments and Kondo screening generates a quantum phase transition between a magnetic and non-magnetic phase. In addition, the multiple impurity models also show non-Fermi liquid behavior if the Kondo interaction does not fully screen the total local moment. Another example is the multi-channel Kondo model,[51,52] which displays non-trivial physics due to the competition between independent channels in the screening of a local moment. In particular, the two-channel Kondo model displays a quantum phase transition from a Fermi liquid to non-Fermi liquid phase, driven by asymmetry between the couplings, and fractional excitation associated with Majorana quasi-particles.[56–58]

The development nanostructure fabrication has allowed the realization of many-body physics in a well-controllable platform. One example is the observation of the Kondo effect in quantum dot devices.[5,6,59] In these setups, the electronic confinement in the central region induces the formation of a local moment due to the strong electron-electron interaction. As the local moment is coupled to the continuum, at low temperatures, this experimental setup reproduces the Kondo physics originally found in dilute magnetic alloys. The only difference is that in a single-electron transistor, the Kondo effect enhances rather than opposing electron transport through the dot. In 1998, Goldhaber-Gordon *et al.*[5] and Cronenwett *et al.*[59] experimentally encountered the Kondo physics in a quantum-dot

device. Two years later, van der Wiel *et al.* achieved unitary conductance regime.[6] These are some examples that explain why the Kondo physics is still being investigated, until today.[60]

As a next step, Goldhaber-Gordon generalized the single electron transistor to display two-channel Kondo physics. Although a single electron transistor is composed by two conduction channels, the transport between them is coherent, which makes the system act as a single channel. To overcome this limitation, Oreg and Goldhaber-Gordon theoretically proposed an experimental setup composed by a standard single-electron transistor plus a huge quantum dot, in which the second dot emulates an independent second lead. In this setup, coherent transport between the leads and the dots is barred by the finite energy necessary to change the large dot.[61] Five years latter, R. M. Potok *et al.* experimentally implemented the two-channel Kondo model,[8] they offered data confirming the occurence of two channel Kondo effect and found the anomalous power-law $\sqrt{T}$ for the differential conductance. Following the same idea, in 2015, A. J. Keller *et al.* reproduce the crossover and the universal behavior for the two channel Kondo effect in a semiconductor nanostructure.[9]

The Kondo effect arises when two degenerate quantum states are coupled to a continuum.[52] For example, the Kondo physics can explain the enhancement of electronic transport in a superconducting quantum dot,[62] in a spinless quantum dot device,[63,64] in a carbon nanotubes quantum dot[65] and the screening of the charging degrees of freedom on a metallic island.[15] In the last setup, the degenerate states are two charge states of a metallic island. At low temperature, the charge degrees of freedom of the island is restricted to $N+1$ and N electrons, where N is the number of electrons. These two states mimics a pseudospin-1/2 and charge fluctuation emulates a spin-flip mechanism. Based this reasoning on, Matveev has been able to describe the low-energy of this system by the anisotropic Kondo Hamiltonian.[15,66–68] The device is known as the charge-degenerate two channel Kondo Hamiltonian.

Following Matveev's ideas,[15,68] Iftikhar *et al.* fabricated a hybrid metal-semiconductor single-electron transistor that exhibits the charge-degenerate two-channel[1] and three-channel[10] Kondo effect. The setup comprises a huge metallic island coupled to three large electrodes through quantum point contacts. In the Fig.2, the quantum point contacts act as source and drain ($\mathrm{QPC}_{1,2}$); the third one (QPC_p) is used to probe the *in situ* conductance in the two channel Kondo regime. The red lines represent the spin-polarized edge channels in an integer quantum-Hall regime induced by a magnetic field, $B \approx 3.9\mathrm{T}$. To reach the three channel Kondo regime, the coupling at QPC_p becomes comparable to the ones at $\mathrm{QPC}_{1,2}$. A gate potential V_g tunes the charging energy of the metallic island to reach the charge-degenerate point.

In Refs.[1] and,[10] the authors have verified the emergence of two and three channel

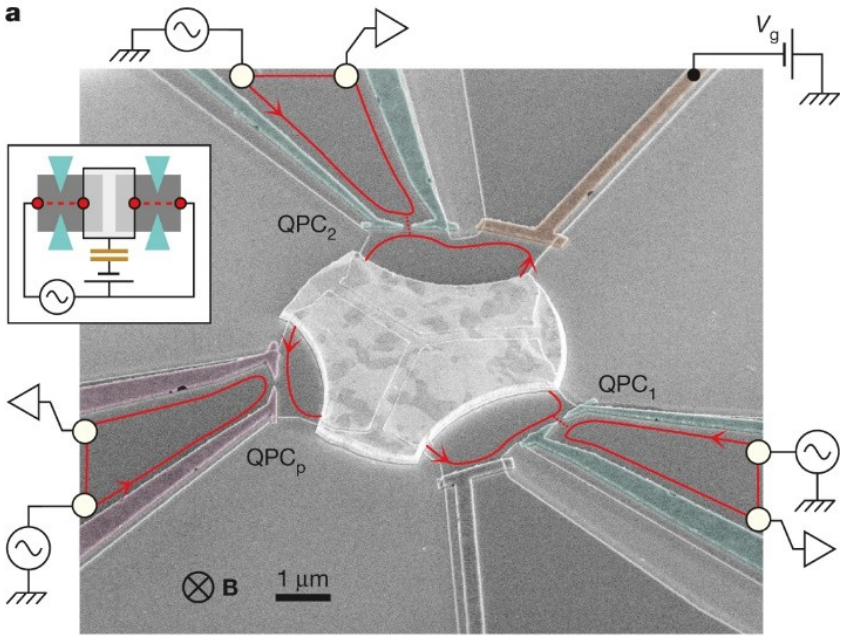

Figure 2 – Experimental setup of a hybrid metal-semiconductor single-electron transistor. The central metallic island is coupled with three large electrodes through quantum point contacts. While two quantum point contacts act as a source and drain ($QPC_{1,2}$), the third one (QPC_p) is used to probe the *in situ* conductance of the device. A gate potential V_g tunes the charging energy of the metallic island. The red lines represent a spin-polarized edge channels of an integer quantum Hall effect induced by a magnetic field $B \approx 3.9$T. The inset schematically displays the single-electron transistor.
Source: Adapted from IFTIKHAR. *et al.*[1]

Kondo phases via linear-conductance measurement as a function of the temperature. Specifically, they have observed the characteristic amplitudes $G_{2K} = 0.5e^2/h$ and $G_{3K} \approx 0.691e^2/h$ and the universal behavior of the linear conductance as a function of temperature for the two-channel and three-channel Kondo phases, respectively. In addition, for the two-channel Kondo experiment, they observed the crossover from the two-channel to the single-channel Kondo phase and, in the three-channel case, the crossover from a three-channel to a single-channel or a two channel-Kondo phase in Ref.[10]

In Ref.,[69] Mitchell and co-authors studied the nonuniversal behavior of the linear conductance as a function of the temperature measured by Iftikhar *et al.*[1] Via Numerical Renormalization Group, they have been able to reproduce the experimental conductance curves and compute the difference between the universal and nonuniversal conductances. The universal conductance was calculated for $T \ll T_{2CK} \ll D$, where T_{2CK} is the two channel Kondo temperature and D is the bandwidth. In addition, the authors have briefly discussed the non-equilibrium conductance, on the basis of the Emery-Kivelson solution. In another work, van Dalum and Fritz, in colaboration with Mitchell, have explored in more detail the electrical and heat transport properties for the Emery-Kivelson solution.[70]

In the context of Kondo physics, Emery-Kivelson solution does not precisely describe the charge-degenerate two channel Kondo effect. To obtain the quadratic form of the Hamiltonian, it must set by hand an azimutal coupling between the pseudospin-1/2 and the leads. The Emery-Kivelson solution was studied in the 1990s by Shiller and Hershfield.[71–73] On the basis of this solution, they calculated the low-temperature and low-voltage scaling laws for the differential conductance. In a technical work, Shiller and Hershfield in colaboration with Majumdar have emphasized that including terms previously not considered in the Emery-Kivelson solution changes the low-temperature and low-voltage scaling coefficient, indicating nonuniversal behavior. However, they point our that in a wideband regime the universal behavior is restored.[74]

Motivated by the recent experiment of Iftikhar *et al.*,[1] we investigate the non-equilibrium properties of the charge-degenerate two channel Kondo (CD-2CK) model. Specifically, we focus on the time-dependent current and differential conductance. This part of the project analyzes the universal and nonuniversal behavior of the differential conductance. To go beyond the Emery-Kivelson solution, we employ the time-dependent Density Matrix Renormalization Group (tDMRG),[75,76] which precisely describes the dynamic properties of the Kondo effect with relatively small computation effort.[77,78] The system is driven out of equilibrium by the sudden application of a bias voltage between the source and drain. Based on tDMRG, we are able to follow the time evolution for times longer than the transient regime, although not long enough to reach the steady state.

Throughout the development of this project, we noticed that the problem is more complex than we had initially expected. Because of that, we have not been able to conclude it, yet. Up to now, our numerical results show that: in the two-channel Kondo phase, the differential conductance shows a universal as a function of the bias, when the differential conductance is scaled by $\sqrt{T_{2CK}}$. For finite gate potential applied to the island, we show that the transient regime can be explained by the energy-time uncertainty principle. As the bias voltage is increased, the differential conductance shows the expected crossover from Fermi-liquid to non-Fermi-liquid behavior.

1.3 Outline

We organize this thesis as following. Chap. 2 discusses the electronic transport properties of semiconductor nanostructure in the framework of model Hamiltonians. First, we summarize the main features of the Kondo model and its straightforward generalizations. Thereafter, we focus on the electronic properties of a single electron transistor and discuss the Coulomb blockade. Finally, we focus on two SET-like devices, one composed by a tiny central region, such as a quantum dot, and another given by a huge metallic island. In the low-energy regime, these experimental devices are described by the Anderson and Kondo Hamiltonians, respectively.

To include all correlation effects into the Anderson and Kondo Hamiltonian, we have carried out NRG and DMRG computations, respectively. In Chap. 3 we present technical details on the Numerical Renormalization Group and Density Matrix Renormalization Group methods. These two approaches are necessary to compute the equilibrium and non-equilibrium properties of the two models, respectively.

Chap. 4 summarizes the main results concerning correlation effects in the emergence of a bound state in the continuum. Briefly, we model a two quantum dot device coupled to a quantum wire by a two-impurity Anderson Hamiltonian. Thereafter, a fixed point analysis of the model provides an overview of the physical behavior. The numerical results show us that the intra-dot coulomb interaction indirectly connects the BIC with the continuum and induces the emergence of a bound spin state in the continuum.

In Chap. 5, we summarize the non-equilibrium transport properties of the charge-degenerate two channel Kondo model. Our numerical results focus on the transient regime induced by the sudden application of a bias voltage between the leads, and the physical analysis is guided by the energy-time uncertainty principle.

Finally, in Chap. 6 we summarize the main conclusions of the two projects.

2 KONDO EFFECT IN NANODEVICES

The electrical resistivity of pure metals decreases with decreasing temperature. This effect is a result of the suppression of the crystal lattice vibration caused by the temperature. However, in the 1930s, measurements showed that, for temperature lower than a special temperature, nowadays known as Kondo temperature (T_K), the electrical resistivity increases logarithmically.[79] This anomalous behavior, associated with magnetic impurities,[80] was only explained 30 years after its first detection. Based on perturbation theory, J. Kondo showed that the spin-flip scattering induced by magnetic impurity logarithmically increases the electrical resistivity.[4]

The complete theoretical description of the Kondo effect was accomplished via Numerical Renormalization Group by Wilson in 1975.[81] Until today, this method stands as a powerful tool that precisely describes dynamics and thermodynamics properties for the whole range of temperatures and physical parameters. Thereafter, the Kondo Hamiltonian was also solved in the framework of other methods, such as the Bethe Ansatz,[82] conformal field theory,[83] bosonization,[84,85] Fermi liquid theory[86] and Density Matrix Renormalization Group[77,78] (DMRG). The two projects developed in this thesis focus on the NRG and the DMRG approaches. More details about them are presented in Chap. 3.

Even though it is a well-known phenomenon, which has been over 60 years, the Kondo effect continues instigating physicist.[60] Nowadays, with the development of nanotechnology, the Kondo physics can be probed on isolated adatoms in metallic surfaces via Scanning Tunneling Microscope (STM).[87] Although the STM has spatial resolution and probes the density of state, this tool does not tune, as far as I know, the atomic properties of the impurities. By contrast, semiconductor quantum dots offer a flexible and well controlled platform. The high controllability of the experimental parameters allows direct correspondence between condensed matter Hamiltonians and experiments.[5,6]

To connect experiment with theory, this chapter is organized as follows. Sec. 2.1 presents the anisotropic Kondo Hamiltonian. It also introduces the idea of multi-impurity and multi-channel Kondo Hamiltonian via straightforward generalization. Thereafter, Sec. 2.2 specifies the characteristic energies of a single electron transistor (SET) of any size and geometric shape. In Sec. 2.3 the transport properties of a SET device is described by the Coulomb blockade concept. Finally, in Secs. 2.4 and 2.5 discuss microscopic models used to theoretically investigate the electronic properties of a quantum dot and a metallic island in the SET geometry.

2.1 Kondo model

In its simplest form, the Kondo effect deals with the spin-flip scattering between the conduction electrons and a local magnetic moment. The Kondo physics is captured by

$$\mathcal{H}_{\mathrm{K}} = \sum_{k\sigma} \varepsilon_k c^{\dagger}_{k\sigma} c_{k\sigma} + \frac{J_{\perp}}{2} \sum_{kk'} \left(S^{+} c^{\dagger}_{k\downarrow} c_{k'\uparrow} + S^{-} c^{\dagger}_{k\uparrow} c_{k'\downarrow} \right) + \frac{J_z}{2} \sum_{kk'} S_z \left(c^{\dagger}_{k\uparrow} c_{k'\uparrow} - c^{\dagger}_{k\downarrow} c_{k'\downarrow} \right), \quad (2.1)$$

where the first term describes a non-interacting, half-filled conduction band with semi-bandwidth D and linear dispersion ε_k. The second and third terms describe the perpendicular and parallel component of the spin-spin interaction between the magnetic moment and the free electrons, respectively. For spin-1/2, $\mathbf{S} = (S^{+}, S^{-}, S_z)$ is given by the Pauli matrices. Spin-flip scattering dynamically generates a low-energy scale, known as Kondo temperature (T_K), that depends on the coupling amplitudes $J_{\perp}$, J_z and the density of state of the metallic host.

Specifically, the Kondo Hamiltonian describes the spin-flip scattering of a conduction electron with momentum k and spin σ to a new state with momentum k' and spin $\bar{\sigma}$, where $\bar{\sigma} = -\sigma$. This mechanism changes the electronic properties of the system only if the local moment flips at a rate that distinguishes it from the conduction electrons. For example, at high-temperatures, $T \gg T_K$, the spin-degrees of freedom play no role because the rate of flipping is much smaller than the thermal energy. For $T \ll T_K$, the coupling energy exponentially increases due to the renormalization of $J_{\perp}$ and J_z. In this regime, the average time between spin flips is smaller than the characteristic thermal time $\hbar/k_B T$. In other words, the spin flips so fast that the conduction electrons cannot follow it. As a result, the conduction electrons surround the local moment and screen it, due to the time-delay in the scattering process. This phenomenon originates the Kondo cloud with correlation length $\xi_K = \hbar v_F / k_B T_K$ and a resonant peak with semi-width $k_B T_K$ pinned at the Fermi level.

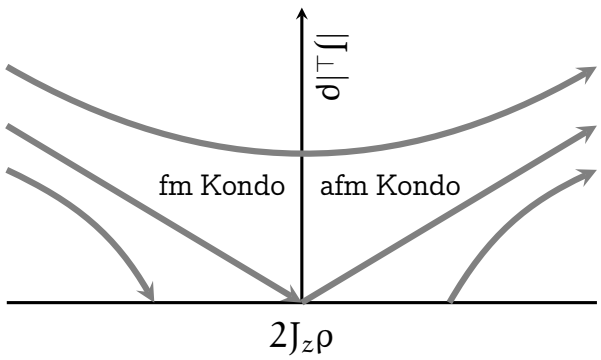

Figure 3 – Sketch of the scaling trajectories for the anisotropic Kondo model obtained via Poor man's scaling.
Source: By the author.

Poor man's scaling explains the renormalization of the spin-flip scattering terms in

the Kondo Hamiltonian. Integrating out the high-energy states of the conduction band, Anderson verified that this approach conserves the conventional form of the Hamiltonian and only corrects the coupling parameters $J_\perp$ and J_z.[88] The renormalization of the coupling parameters are displayed in the flow diagram sketched in Fig. 3. For $J < 0$, i.e., ferromagnetic coupling, the left side of the diagram shows that the coupling parameter flows to zero at low-energy. The local moment decouples from the continuum. In the opposite regime, the right side of the diagram shows that the antiferromagnetic coupling ($J > 0$) diverges. The exponential growth of the coupling parameter is the key mechanism to explain the Kondo screening.

The Kondo Hamiltonian can be straightforwardly generalized by substituting the local moment with spin-1/2 to another with spin-$N/2$ and adding M independent conduction channels. As each channel is capable of fully screening a local moment with spin-1/2, three different regimes are identified. For $M = N$, the total local magnetic moment is *exactly screened* by the conduction electrons. In particular, Eq. 2.1 illustrates the case $N = M = 1$. The *under-scrennned* regime occurs for $N > M$. As the continuum can not fully screen the total magnetization of the system, there will always be a residual magnetic moment at low temperature. Finally, the *over-screened* case is achieved by $M > N$. The latter generates an unstable phase when the M-channels equally screen the local moment. Even though the magnetic moment is fully screened, the system keeps scattering electrons at zero energy.

Two local moments with spin-1/2 and one channel reproduces the *under-screened* case when both spins couple ferromagnetically. For this configuration, the Kondo Hamiltonian is rewritten as

$$\mathcal{H}_{\text{2IK}} = \sum_{k\sigma} \varepsilon_k c^\dagger_{k\sigma} c_{k\sigma} + \sum_{i=1,2} J_i \boldsymbol{S}_i \cdot \boldsymbol{s} + I \boldsymbol{S}_1 \cdot \boldsymbol{S}_2, \tag{2.2}$$

where $\mathbf{S}_i$ is the spin operator of the i-th local moment, for $i = 1, 2$, and $\mathbf{s}$ is the spin-operator of the conduction electrons. Despite being defined differently, the two first terms of $\mathcal{H}_{\text{2IK}}$ have the same structure as Eq. 2.1 for $J_\perp = J_z$. In addition, the third term on the right-hand side describes the direct spin-spin interaction between $\mathbf{S}_1$ and $\mathbf{S}_2$. For $I > 0$, the direct coupling is antiferromagnetic and it favors the formation of a singlet state. Since there is no magnetic moment, the Kondo effect is suppressed. In the opposite regime, i.e., $I < 0$, the ferromagnetic coupling recombines the local moments in a triplet state. In this regime, the conduction electrons screen only half of the local moment of the triplet state. The competition between the antiferromagnetic coupling between the local moments and the Kondo screening triggers a quantum phase transition (QPT). This model has been studied in multiple quantum dots devices and impurity systems. More details about this QPT is in Chap. 4, in the framework of two-impurity Anderson model.

The two-channel Kondo model is the simplest configuration that describes the

over-screened regime. Mathematically, the Hamiltonian is given by

$$\mathcal{H}_{\text{2CK}} = \sum_{k\sigma,j=1,2} \varepsilon_k c^\dagger_{jk\sigma} c_{jk\sigma} + \sum_{j=1,2} J_j \boldsymbol{s}_j(0) \cdot \boldsymbol{S}. \tag{2.3}$$

For $T \ll T_K$, two non-coherent conduction channels compete to screen the localized spin-1/2. This Hamiltonian was first proposed in the 80s by Nozières and Blandin in the context of magnetic impurities.[51,52] In special, the two-channel Kondo model describes a non-Fermi liquid phase and a quantum critical point when the two channels compete in equal footing to screen the local moment. In the presence of a coupling asymmetry or magnetic field, the system crosses over to a Fermi liquid phase described by the single-channel Kondo effect or a non-Kondo phase, respectively.

2.2 Single electron transistor

A single electron transistor, or just SET, is a nanodevice that controls the electron flow through a central region. Fig. 4 sketches the device composed by a metallic island of any size and geometric shape coupled to three electrodes. From the two electrodes, electrons tunnel in and out of the central region. The electrodes act as a source and drain. The electron flow between them is modulated by a potential barrier and an applied bias voltage ($eV = V_L - V_R$). In addition, a gate potential (V_g) controls the electron flow between the leads. Specifically, V_g shifts the density of states and controls the charging energy of the island. The high controllability of such device makes it a suitable platform to reproduce condensed matter models, such as the Kondo and Anderson model.

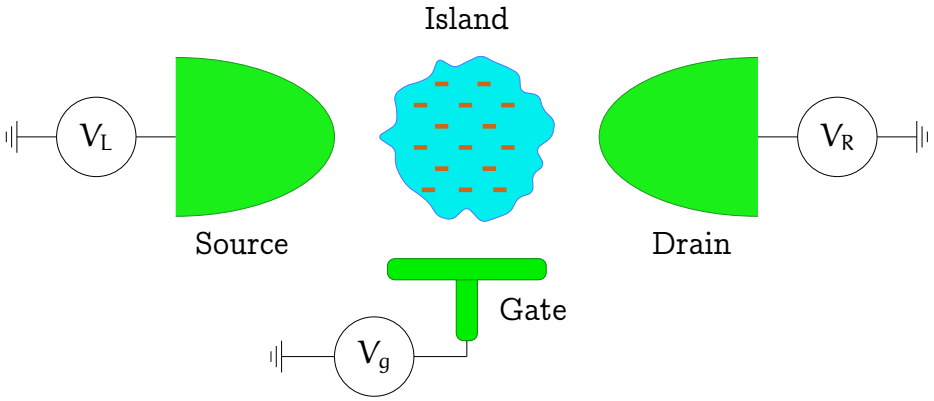

Figure 4 – Sketch of a single electron transistor. The irregular blue circle illustrates a metallic island, of any size and geometry. The two green semi-ellipses describe the source and drain, while the green rectangle represents the gate voltage V_g. Source: By the author.

Charge quantization and the strong electron-electron interaction in the central region controls the electronic transport in the SET. These two physical phenomena originates the Coulomb blockade physics that, at first glance, explains the classical electronic transport in a SET. However, according to the size and geometry of the island

and the temperature of the experimental setup, a variety of quantum effects emerges, and a microscopic theory must be used. Specifically, in this thesis we use the Anderson Hamiltonian to investigate the electronic properties of a quantum dot device and the Kondo Hamiltonian to describe the transport properties of a huge metallic island.

Different physical regimes described by a SET-like device are closely related to its characteristic energies. For example, the Coulomb energy and the mean level energy space play an important role as a consequence of the electronic confinement on the island. Both characteristic energies can be tuned by the geometry shape and size of the island. In addition, different transport regimes can be accessed by tuning other characteristic energies, such as the coupling, thermal energy and external bias voltage.

The *Coulomb energy* plays an important role, due to the electronic confinement in the central region. For $V_g = 0$, the electrostatic energy of the island with N electrons is defined by

$$E_{el}(N) = \frac{e^2 N^2}{2C} \tag{2.4}$$

where C is the capacitance of the central region. The Coulomb, or charging energy, is the energy necessary to add/remove an electron to/from the island. It can be estimated by

$$E_c(N \pm 1) \equiv E_{el}(N \pm 1) - E_{el}(N) = \frac{e^2}{C}(\pm N + 1/2). \tag{2.5}$$

Traditionally, however, in a quantum dot physics the term charging energy is associated by the energy difference between the charging energy for $N \pm 1$ and N electrons. Mathematically,

$$\Delta E_c = E_c(N \pm 1) - E_c(N) = \frac{e^2}{C}, \tag{2.6}$$

and modulates the energy to add (+) and remove (-) an electron from the central region. In addition, as the capacitance is directly proportional to the size of the island, the charging energy become inversely proportional to the size of the island.

Like in the particle-in-a-box problem, the electronic confinement on the island generates quantized states. As a consequence, a new energy scale, known as *mean level energy space* (δ_s), arises. This characteristic energy is defined by the average of the energy difference between two successive discrete states.

To estimate the magnitude of these two characteristic energies, let us suppose that the central region is a metallic cubic of size L. From Coulomb's law, the *charging energy* in Eq. 2.6 become $E_c \simeq e^2/L$. In addition, the *mean level energy space* can be estimated by the Fermi energy (E_F) divided by the number of electrons on the central region, i.e., $\delta_s \simeq E_F/N$. Considering that there is one valence electron per atom, the number of atoms can be roughly estimated by $(L/a)^3$, where a being the interatomic distance. The ratio

between the two characteristic energies is

$$\frac{\delta_s}{E_c} \simeq \frac{E_F L}{e^2 N} = \frac{E_F a}{e^2}\frac{L}{aN} \simeq N^{-2/3}. \tag{2.7}$$

Here we have used $e^2/a \simeq E_F$. Now, suppose that $E_c \simeq 1\text{meV}$ is a fixed parameter. If the island is huge enough to host billions of electrons, $\delta_s \simeq 10^{-8}\text{eV}$. In this case, δ_s does not play any role because $\delta_s \ll E_c$. The opposite regime can be observed in a tiny metallic island with several electrons. For example, if $N = 30$, the ratio $\delta_s/E_c \simeq 0.1$. This number shows that even though the Coulomb energy predominates, the discreteness of the island influences into the electronic transport of a SET like-device.

The *coupling energy*, usually represented by Γ, defines the coupling strength between the leads and the central region. The tunneling rate is estimated by the Fermi golden rule

$$\frac{1}{\tau} = \frac{\Gamma}{\hbar} \tag{2.8}$$

with $\Gamma = 2\pi\mathcal{V}^2\rho_0$, ρ_0 being the density of state of the leads, and $\mathcal{V}$ being the hybridization amplitude between the leads and the island.

To achieve the Coulomb blockade regime, the coupling energy must be weak enough to suppress the charge fluctuation and strong enough to quantize the electronic number on the island. The energy-time uncertainty principle provides a good estimate of the resistance R_t of the potential barrier in the system to achieve the such configuration. Assuming that the time for an electron to tunnel into the island can be defined by $\Delta t = R_t C$, as in an RC-circuit, and $\Delta E = E_c$, the resistance become

$$R_t > h/e^2. \tag{2.9}$$

R_t must be larger than h/e^2 for the charge be quantized.

Different from the previous characteristic energies discussed in this section, the *thermal energy* is an external energy. In the equilibrium framework, the thermal energy modulates electronic excitation processes in units of $k_B T$, where k_B is the Boltzmann constant. Therefore, the Coulomb blockade regime is achieved for $k_B T \ll E_c$. Outside of this condition, there is no charge quantization.

The *bias voltage* (eV) is also an external energy, however, it is suddenly introduced into the leads. The bias shifts the Fermi level of the source and drain by a factor $\pm eV/2$ and drives the system out-of-equilibrium. In addition, it generates an electrical field that induces electron flow through the island. In non-equilibrium, time-translation symmetry is broken and all excitation processes become time dependent. At first glance, in the limit $t \to \infty$, known as steady-state regime, the bias voltage induces excitation processes with energy eV. This behavior is similar to thermal excitations. However, in the short time limit, known as transient regime, energy excitation become time dependent and the previous analogy cannot be used anymore. The non-equilibrium regime in a SET-like device is discussed in more detail in the Chapter 5.

2.3 Coulomb blockade regime

In a SET-like device, the Coulomb blockage regime is reached for E_c much larger than δ_s, k_BT and Γ. Despite the complexity introduced by the Coulomb interaction, the electronic transport is qualitatively explained by classical arguments when only real tunneling processes are considering.

For finite V_g, the electrostatic energy in Eq. 2.4 is generalized by

$$E_{el} = E_c \left(N - \frac{q}{e} \right)^2 \tag{2.10}$$

with $E_c \equiv e^2/2C$. The induced charge q/e on the island is a continuous parameter modulated by the gate potential V_g. Panel (a) in Fig. 5 plots the electrostatic energy as a function of q/e for $N-1$, N and $N+1$ electrons on the island. Whenever q is half-integer, the charging energy with N to $N \pm 1$ electrons are degenerate. This charge degenerate point allow charge fluctuation on the island. Outside of this condition, the island takes the configuration with lower energy.

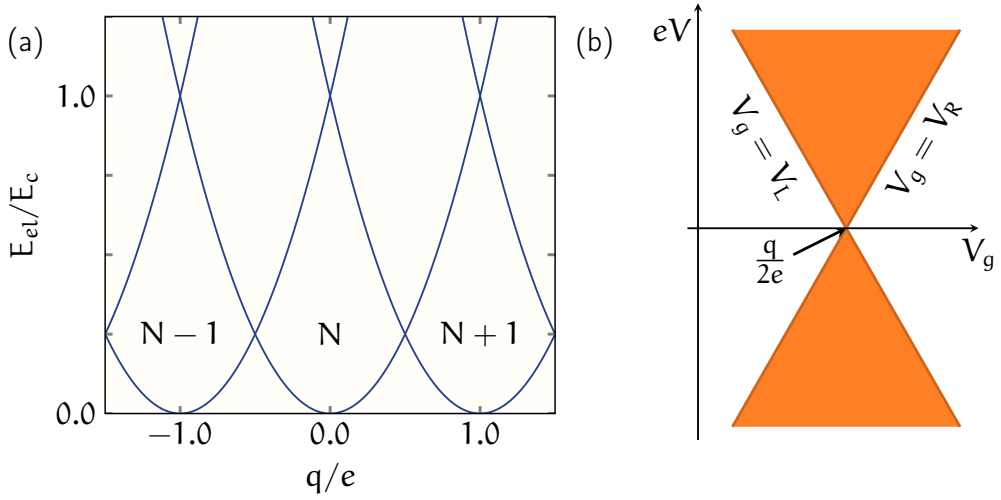

Figure 5 – Panel (a): Electrostatic energy as a function of the charge q/e. The three curves represent the electrostatic energy of the island with $N-1$, N and $N+1$ electrons. Panel (b): Schematic Coulomb blockade diagram as a function of the bias voltage (eV) and the gate potential (V_g). Current flows in the orange region.
Source: By the author.

Applying a zero-bias voltage ($eV \to 0$) between the source and drain, an electron crosses the island only if q/e is half-integer. At this special point, an electron tunnels in and out of the island without changing the energy of the system. For other q/e, the tunneling is blocked by the Coulomb interaction. This pattern is known as Coulomb blockade. Note that this behavior is $e-$*periodic* because the charging energy is the only relevant energy into the system. The periodicity is missed when the mean level space energy is of the same order as E_c.

Panel (b) of Fig. 5 shows the Coulomb blockade diagram as a function of the bias voltage and the gate potential. For finite bias voltage, an electron crosses the island whenever the bias voltage is larger than the charging energy. Such regime is achieved for the set of parameters indicated in the orange region. In the white region, the charging energy blocks the current. The zero-bias regime corresponds to the point $q/2C$.

2.4 Quantum dot device

A semiconductor quantum dot is a SET-like device able to host a few dozens of electrons. Due to the size of the island, the electronic confinement induces a mean energy level scale comparable to the charging energy. Specifically, $\delta_s/E_c = 0.1 - 0.5$ for a tiny quantum dot. The Coulomb blockade physics also explain the electronic transport properties of a quantum dot when only real tunneling process are under consideration. As higher order tunneling processes become relevant at low temperature, the classical arguments used so far fails. Thus, a microscopic theory must be adopted to completely describes the electronic properties of the dot.

There are two higher order tunneling processes in a quantum dot: i) cotunneling; and ii) spin-flip scattering. These two processes describe virtual tunneling involving two electrons; however, only in the second one does the spin degree of freedom of the dot change. In the cotunneling process, an electron tunnels from the source to the drain due to the intermediation of a nonresonant state. For example, let us suppose that the dot is full of electrons at $k_BT = 0$. An electron from the source can only tunnel into the dot to a non-occupied state and, thereafter, tunnel to the drain. Another possibility is an electron from the dot going to an excited empty state and, subsequently, tunneling to the drain while one electron from the source occupies the vacant position. We should emphasize that there are infinities possibilities of cotunneling thought the dot; however, we only describe the most probables one. Cotunneling is only relevant at low temperatures because the time prescribed by the energy-time uncertainty principle for the system to achieve the energy resolution k_BT is longer than the time for the virtual process.

In a quantum dot device, spin-flip scattering is also a virtual tunneling process involving two electrons. This process is predominant when the dot has an odd number of electrons at low temperature. For example, let us assume that a quantum dot is fully occupied and has only an up-spin valence electron. For this initial configuration, an electron tunnels from the source to the drain due to two intermediate virtual processes. First, an electron from the source with spin down tunnels into the dot and, subsequently, an electron from the dot with spin up tunnels to the drain. Second, an electron with spin up from the dot tunnels into the source or drain and, thereafter, an electron with spin down from the source tunnels into the dot. In these processes the initial and final spin orientation of the quantum dot are different. As this process mimics the spin-flip scattering in the

Kondo Hamiltonian, discussed in Sec. 2.1, at low temperatures one expects a Kondo effect to arise in quantum dot devices.

To contemplate real and virtual tunneling processes, in this section we model a quantum dot by the single-impurity Anderson Hamiltonian. Despite its simplicity, this microscopic model captures the charge fluctuations in the quantum dot and the Kondo effect induced by the strong correlation effects.

2.4.1 Anderson model

Fig. 6 illustrates the energy representation of a quantum dot device in a SET geometry. The blue lines describe the discrete states of the dot while the green rectangles represent the source and the drain. The quantum dot state can be empty, simply or doubly occupied according to its energy position relative to the Fermi level. Assuming that a state is above or below, it must be empty or doubly occupied, respectively. Furthermore, for large Coulomb interactions, the valence state of the dot must be singly occupied. See for example the configuration in Fig. 6.

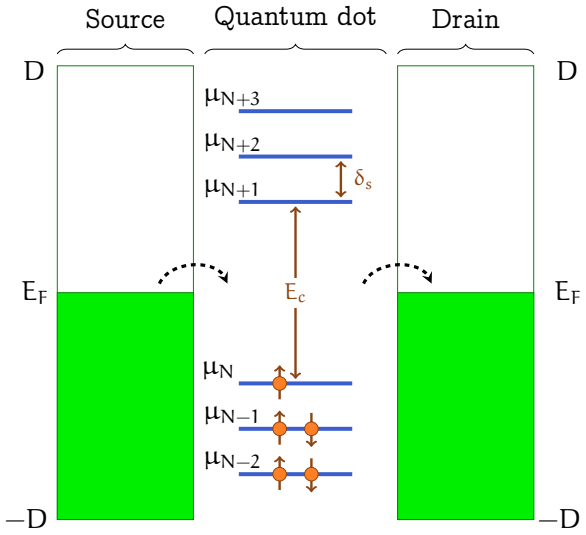

Figure 6 – Energy representation of a quantum dot device. The green rectangles illustrate a non-interacting, half-filled conduction band with bandwidth $2D$, while the blue lines between them defines the discrete states of the dot. The orange circles represent the electrons with spin orientation indicated by the arrows.
Source: By the author.

At low-energy, only the quantum dot states around the Fermi level are energetically accessible, while all the other states are frozen. Under these circumstances, the low-energy physics of the quantum dot can be precisely described by the single-impurity Anderson model (SIAM), in which the dot state closest to the Fermi level can be empty, simply or doubly occupied. In the framework of the Anderson model, the empty configuration corresponds to the level μ_N in Fig. 6 without the spin-up electron. In the presence of an extra electron, as displayed in Fig. 6, the energy level of the dot gets energy ε_d. Finally, in

the presence of a spin-down electron, the dot acquires energy $2\varepsilon_d + \mathcal{U}$. In this model, $\mathcal{U}$ describes the charging energy of the dot. Note that the other states do not interfere in the low-energy physics of the dot, because the system does not have enough energy to modify them. Furthermore, even if V_g is high enough to shift the higher energy states close to the Fermi level, the same properties must be observed, because the states are energetically periodic.

Mathematically, the single-impurity Anderson Hamiltonian is given by

$$\mathcal{H}_{\text{SIAM}} = \sum_{k\alpha} \varepsilon_k c^\dagger_{k\alpha} c_{k\alpha} + \varepsilon_d d^\dagger d \ + \mathcal{U} n_{d\uparrow} n_{d\downarrow} + \frac{1}{\sqrt{\mathcal{N}}} \sum_{k\alpha} (\mathcal{V}_\alpha c^\dagger_{k\alpha} d \ + \text{H.c.}). \tag{2.11}$$

The first term on the right-hand side of Eq. 2.11 describes the left and right leads ($\alpha = L, R$) as a non-interacting, half-filled conduction band with bandwidth $2D$ and linear dispersion relation ε_k. The second and third terms represents the energy ε_d of the dot level d and the Coulomb repulsion $\mathcal{U}$ resulting whenever it is doubly occupied. The final term couples the dot to the two leads.

2.4.2 Even-odd transformation and channel concept

The single-impurity Anderson model is simplified by the even-odd transformation

$$\begin{pmatrix} c^\dagger_{kL} \\ c^\dagger_{kR} \end{pmatrix} = \begin{pmatrix} \cos\theta & -\sin\theta \\ \sin\theta & \cos\theta \end{pmatrix} \begin{pmatrix} c^\dagger_{ke} \\ c^\dagger_{ko} \end{pmatrix}, \tag{2.12}$$

with $\tan\theta = \mathcal{V}_R/\mathcal{V}_L$. This linear transformation explores the parity symmetry between the source and drain and works even for $\mathcal{V}_R \neq \mathcal{V}_L$. As a result, the Anderson Hamiltonian defined on Eq. 2.11 become $\mathcal{H}_{\text{SIAM}} = \mathcal{H}^e_{\text{SIAM}} + \mathcal{H}^o_{\text{SIAM}}$, with

$$\mathcal{H}^e_{\text{SIAM}} = \sum_k \varepsilon_k c^\dagger_{ke} c_{ke} + \varepsilon_d d^\dagger d \ + \mathcal{U} n_{d\uparrow} n_{d\downarrow} + \frac{\tilde{\mathcal{V}}}{\sqrt{\mathcal{N}}} \sum_k \left(c^\dagger_{ke} d \ + \text{H.c.} \right) \tag{2.13}$$

where $\tilde{\mathcal{V}} = \sqrt{\mathcal{V}_L^2 + \mathcal{V}_R^2}$, and

$$\mathcal{H}^o_{\text{SIAM}} = \sum_k \varepsilon_k c^\dagger_{ko} c_{ko}. \tag{2.14}$$

The linear transformation shows that the dot level only couples to the conduction band with even-parity symmetry, while the conduction states with odd-parity symmetry are decoupled from it.

The even-odd transformation help us to understand the definition of channel used in Sec. 2.1. Even though the Anderson Hamiltonian be initially defined by two conduction channels (source and drain), the electron exchange between them generates coherent transport. As a result, the source and drain act as an effective conduction channel. A different behavior is expected in the Kondo Hamiltonian because the spin-flip mechanism never exchange electrons between the channels. Therefore, they act independently because

there is no coherent transport between them. In addition, note that the two-channel Kondo Hamiltonian is invariant under even-odd transformation. This transformation is explicitly shown in Ref.[72]

2.4.3 Schrieffer-Wolff transformation

The virtual spin-flip scattering processes dominates the physics of the Anderson model for $\mathcal{U} + \varepsilon_d \gg \Gamma$, with $\varepsilon_d < 0$. For this set of parameters, the dot level is restricted to the simply occupied configuration and mimics the physics of the Kondo problem at low temperature. The correspondence between Anderson and Kondo models is explicitly shown by the Schrieffer-Wolff transformation.[89]

The Schrieffer-Wolff transformation integrates out the empty and double occupied configurations of the dot and perturbative includes it in an effective Hamiltonian. As a result, the Anderson model become

$$\mathcal{H}_{\mathrm{K}}^{\mathrm{SW}} = \sum_{k\sigma} \varepsilon_k c_{k\sigma}^{\dagger} c_{k\sigma} + J\boldsymbol{S}\cdot\boldsymbol{s}(0) \tag{2.15}$$

where the first term is a non-interacting, half-filled conduction band with bandwidth $2D$ plus a spin-flip scattering term. The spin $\mathbf{S}$ defines the local moment of the singly occupied dot level and $\mathbf{s}$ is the spin-operator of the conduction electrons. In addition, this transformation shows that the spin-flip amplitude is given by

$$J = \frac{2\mathcal{V}^2\mathcal{U}}{|\varepsilon_d|(\varepsilon_d + \mathcal{U})}. \tag{2.16}$$

The derivation of Eq. 2.16 neglects ε_k in comparison with $|\varepsilon_d|$ or $\mathcal{U}$. This result emphasizes that the spin-spin interaction between the conduction electrons and the continuum is antiferromagnetic.

2.5 Huge metallic island

In this section, we discuss the transport properties in a spinless SET-like device capable of host several billions of electrons in its central region. Different from a quantum dot device, the mean level energy space δ_s is irrelevant compared with other energy scales.

Panel (a) of Fig. 7 sketches the energy representation of a SET for energy lower than E_c, i.e. $k_BT \ll E_c$ and $eV \ll E_c$. The rectangles are non-interacting, half-filled conduction band with semi band-width E_c. The green ones represent the left (source) and right (drain) leads, while the blue ones describes the island as two independent electron gases. In the device, the island is large enough to suppress coherent transport between both sides. In addition, a gate potential (V_g) controls the electrostatic energy on the island, as defined in Eq. 2.10. For V_g such that the induced charging on the island is $q = e/2$, only the charging states displayed in Panel (b) of Fig. 7 contributes to the system. The energy difference between the charging states with $N+1$ and N electrons is given by eU.

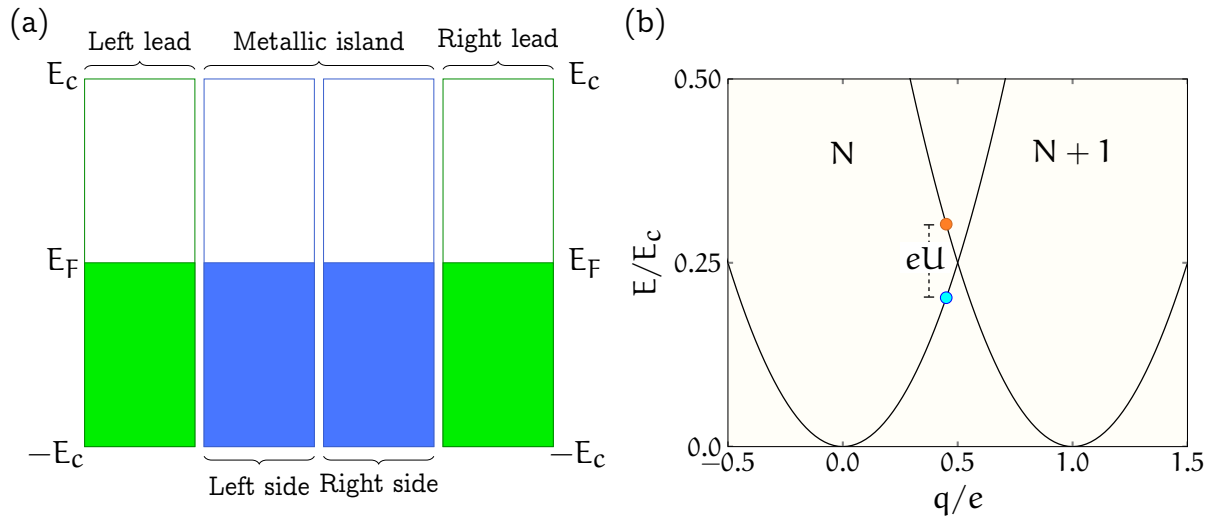

Figure 7 – Panel (a): Energy representation of a single electron transistor composed by a huge metallic island. The rectangles represent a non-interacting, half-filled conduction band with semi band-width E_c. The green and blue rectangles represents, respectively, the leads and the island. Panel (b): Electrostatic energy as a function of q/e. The blue and orange circle indicates the charge energy of the island with N and $N+1$ electrons. eU is the energy difference between the two charge configurations.
Source: By the author.

The electronic transport through the island follows the Coulomb blockade physics when only tunneling process are considering. However, as the temperature decreases, cotunneling process become relevant and the classical description fails. To capture the charging fluctuation on the island induced by cotunneling, we follow the microscopic formalism proposed by Matveev.[15,66–68]

The microscopic properties of the huge SET-like device is described by Hamiltonian

$$\mathcal{H}_{\text{Huge}} = \sum_{k,\alpha} \varepsilon_k c^\dagger_{k\alpha} c_{k\alpha} + \sum_{p,\alpha} \varepsilon_p c^\dagger_{p\alpha} c_{p\alpha} + \sum_{k\alpha,p} \left(J_{k\alpha,p} c^\dagger_{k\alpha} c_{p\alpha} + \text{H.c.} \right) + \frac{\hat{Q}^2}{2C} \tag{2.17}$$

where $c^\dagger_{k/q,\alpha}$ ($c_{k/q\alpha}$) creates (annihilates) an electron with energy $\varepsilon_{k/q}$ in the lead/island with momentum k/q in the α side of the lead/island. $\alpha = L, R$ labels the left and right sides of the system. The third term of the right-hand side of Eq. 2.17 describes the tunneling mechanism of an electron from the leads into the island and vice-verse. Finally, the last term describes the charging energy of the island, with

$$\hat{Q} = \sum_{p,\alpha} c^\dagger_{p\alpha} c_{p\alpha}, \tag{2.18}$$

with C is the capacitance of the island. The last one is the only mechanism that connects the two electron gases on the island.

Adjusting the external potential energy V_g, such that $\left\langle \hat{Q} \right\rangle = e(N + 1/2)$, and restricting $k_B T$ and eV to much lower than E_c, the transport properties are governed only

by the charging states with N and $N+1$ electrons. Therefore, projected into the subspace Ψ_{N+1} and Ψ_N, the Hamiltonian in Eq 2.17 is rewritten as

$$\mathcal{H}_{\text{2CK}} = \sum_{k,\alpha} \varepsilon_k c^\dagger_{k\alpha} c_{k\alpha} \begin{pmatrix} 1 & 0 \\ 0 & 1 \end{pmatrix} + \sum_{p,\alpha} \varepsilon_p c^\dagger_{p\alpha} c_{p\alpha} \begin{pmatrix} 1 & 0 \\ 0 & 1 \end{pmatrix} + eU \begin{pmatrix} 1 & 0 \\ 0 & 0 \end{pmatrix} + \sum_{k,p,\alpha} \left[J_{k\alpha,p} c^\dagger_{k\alpha} c_{p\alpha} \begin{pmatrix} 0 & 0 \\ 1 & 0 \end{pmatrix} + \text{H.c.} \right]$$

where the 2×2 matrices are the projection operators $\hat{P}_{N+1}$ and $\hat{P}_N$, that act on the subspace

$$\hat{\psi} = \begin{pmatrix} \Psi_{N+1} \\ \Psi_N \end{pmatrix}. \tag{2.19}$$

In the Hamiltonian, eU modulate the charging energy difference between the configurations with N and $N+1$ electrons on the island and is controlled by the gate potential V_g, as indicated in Panel (b) of Fig. 7.

Finally, in order to simplify Eq. 2.19, we label the states in the leads by the index $\sigma = \uparrow$ and the states of the island by $\sigma = \downarrow$. In addition, we also label the charging states as $\Psi_{N+1} \rightarrow \Uparrow$ and $\Psi_{N+1} \rightarrow \Downarrow$. Therefore, the Hamiltonian is rewritten as

$$\mathcal{H}_{\text{2CK}} = \sum_{k,\alpha,\sigma} \varepsilon_k c^\dagger_{k\alpha\sigma} c_{k\alpha\sigma} + \sum_{k,p,\alpha} \left(J_{k\alpha,p} c^\dagger_{k\alpha\uparrow} c_{p\alpha\downarrow} S^- + \text{H.c.} \right) - eUS_z \tag{2.20}$$

where the matrices in Eq. 2.19 were substituted by the spin operators. The mapping results in the anisotropic Kondo Hamiltonian. However, as the charge degenerate states of the island mimic a pseudospin-1/2, we prefer to call it the charge-degenerate two-channel Kondo (CD-2CK) Hamiltonian. On the spin basis, the cotunneling processes emulates a spin-flip scattering and the charging energy splitting eU mimics a Zeeman splitting in a Kondo impurity problem. Table 1 summarizes the rules of the mapping.

Although the CD-2CK Hamiltonian differs from the two-channel Kondo Hamiltonian in Eq. 2.3, they reproduce the same universal physics. Specifically, the parallel component of the spin-flip scattering only modifies the Kondo temperature. Another difference from the Hamiltonian of CD-2CK is the presence of a local magnetic field that breaks the spin degeneracy of the local moment.

Table 1 – Rules of the mapping of the Real system into the Kondo Hamiltonian.

Real system	**Kondo basis**
Charging energy (E_c)	Bandwidth (E_c)
Tunneling (J_L and J_R)	Exchange coupling (J_L and J_R)
Gate voltage (eU)	Magnetic field (eU)
Leads	Spin up electrons
Metallic Island	Spin down electrons
Occupation number	Local moment

Source: By the author.

3 NUMERICAL METHODS

Quantum impurity models, as the ones discussed in Chap. 2, are non-trivial many-body problems that involves an infinite number of degrees of freedom. Usually, these problems are composed by a quantum impurity with strong Coulomb interaction coupled to a non-interacting conduction states. The coupling between them results in small energy excitation that induces infrared divergences in perturbation theory treatments. A well-known example is the divergence of the perturbative approach applied in the Kondo problem.

To precisely describes the correlation effects of quantum impurity models and avoid divergences at low temperature, in this thesis we investigate quantum impurity models in the framework of Numerical Renormalization group (NRG) and time-dependent Density Matrix Renormalization group (tDMRG). The first approach is used to calculate the dynamical and thermodynamical properties of the two-impurity Anderson Hamiltonian in Chap. 4. Such method is essential to include all correlation effects of bound states in the continuum. The second one is necessary to investigate the non-equilibrium properties of the charge-degenerate two channel Kondo model in Chap. 5.

In this chapter, we summarize the main concepts of these numerical methods based on simple systems. In Sec. 3.1, the NRG approach is discussed in the framework of the single-impurity Anderson model. Following the main steps presented in this section, the method can be easily adapted for other cases studied in this thesis. The DMRG and tDMRG are discussed in Sec. 3.2 in the framework of Matrix product states (MPS) and Matrix product operators (MPO). That section follows a general explanation of the method and all mathematical details are illustrated by tensor schemes.

3.1 Numerical Renormalization Group

The Numerical Renormalization Group, or NRG, is a numerical tool that iteratively solve a many-body Hamiltonian with small computation cost. The NRG is vastly used to solve quantum impurity problems coupled to a continuous spectrum. This method also holds accurate results for multi-impurity[44,90–93] and multi-channel[2,94] Hamiltonians.

The NRG is underpinned by Renormalization Group theory. Shortly, that theory offers a framework supporting the development of energy-scale transformations. In practice, such transformations map a Hamiltonian $\mathcal{H}(\mathbf{K})$ onto another, with the same symmetry. Conceptually, or formally, in special cases, the transformed Hamiltonian can be identified with the original Hamiltonian with renormalized parameters, that is, $\mathbf{K} \to \mathbf{K}'$. For the single-impurity Anderson model, the interacting parameters are given by $\mathbf{K} = (\varepsilon_d/D, \mathcal{U}/D, \Gamma/D)$.

Mathematically, the transformation is defined by

$$\tau[\mathcal{H}(\mathbf{K})] = \mathcal{H}(\mathbf{K}'). \tag{3.1}$$

where τ defines the RG transformation. This transformation follows the same principle of the Poor Man's scaling approach discussed in Sec. 2.1. In other words, according the high-energy conduction band states are integrated out via a course-grain transformation and, the interacting parameters are renormalized while the Hamiltonian keeps its form. Different from Poor Man's scaling approach, in the NRG approach such transformation is carried out nonperturbatively.

The beauty of the RG theory lies in simple physical concepts hidden along the mathematical machinery given in Eq. 3.1. Specifically, the full physical behavior of a many-body Hamiltonian can be described in terms of: (i) RG trajectories in the parameter space $\mathbf{K}$; (ii) fixed points; and (iii) crossover between them. The trajectories through the phase space are directly obtained from RG transformation in Eq. 3.1. In addition, a sequence of transformations τ takes the system into or close to a fixed point. Formally, such special point is reached when $\tau[\mathcal{H}(\mathbf{K}^*)] = \mathcal{H}(\mathbf{K}^*)$, for $\mathbf{K}^*$ being the parameters in the phase space. The latter tell us that the system is invariant under RG transformation in a fixed point.

In the neighborhood of a fixed point, the RG transformation can be linearized. Such approximation allows us to identify the operators that take the system into or away from a fixed point. In the theory, these operators are known as relevant, irrelevant or marginal. As the own name says, a relevant operator increases along the RG transformation and drives the RG flow away from a fixed point. An irrelevant operator decreases as the Hamiltonian is renormalized and, hence, does not play any role in the RG flow. Finally, a marginal operator is invariant under RG transformations. These three kinds of operators take us to two types of fixed points: (i) stable and (ii) unstable. In the first type, there are only irrelevant operators nearby, hence, the Hamiltonian remains the same under RG transformations. In the opposite case, the instability of the fixed point is due to relevant operators that diverts the RG flow. All these simple concepts allow us to map the phase space and explain the physical behavior of a complex many-body Hamiltonian, based on fixed points and the crossover between them.

Based on the previous RG concepts, in the next subsections we introduce the mathematical formalism of NRG. Basically, this method perform the RG transformation nonperturbatively. In addition, the concepts of fixed point and RG flow are used to explain the physical results in Chapters 4 and 5.

3.1.1 Numerical implementation

The numerical implementation of the NRG method is summarized in the following steps:

- Firstly, the NRG approach reduces the conduction states to logarithmic intervals and, for each energy interval, the method associates a discrete set of states. The logarithmic mesh is essential for the NRG to accesses the excitation spectrum, from excitations of the order of the semi-bandwidth D to excitations close to zero.

- Next, the Lanczos transformation projects the discretized states on a tridiagonal basis, suitable to allow diagonalization of the full Hamiltonian, iteratively. On this basis, the conduction states became a semi-infinite tight-binding chain with hopping terms that decay exponentially. Besides being essential for iterative diagonalization, there are two extra motivations for the Lanczos transformation: (i) all the discrete states coupled to the quantum impurity are precisely included in the iterative diagonalization procedure and; (ii) it allows definition of an infrared cutoff. The latter makes the tight-binding chain finite and numerically tractable.

- From the technical point of view, the third step, namely the iterative diagonalization is the most methodologically complex part of NRG. This procedure is governed by a simple RG transformation, as the one expressed in Eq. 3.1. To make this step numerically tractable, an ultraviolet cutoff truncates out the high-energy states.

- At the end of each iteration, the eigenvalues and eigenvectors obtained from NRG are used to calculate the physical quantities of interest. Specifically, in this section we discuss the calculation of the magnetic susceptibility and the spectral density.

Before we discuss the technical detail, I would like to compare the NRG approach with a microscope that measures the electronic excitation in a well-defined energy interval. Specifically, the microscope is composed by many microscope lenses labeled by the index N, which varies from 0 to N_{max}. The latter defines the maximum number of lenses into the macroscopic. The energy-magnification ratio between two consecutive lenses is given by $\Lambda^{1/2}$, with Λ being a real number bigger than 1. These lenses give access to excitation processes of the order of $\Lambda^{-N/2}$.

All measurements performed by the NRG-like microscope must start from the 0-th lens and gradually increase until the microscope reaches the energy scale of interest. This restriction is imposed because the excitations processes measured by the N-th lens corrects the low-lying excitations processes measured by the $(N+1)$-th lens. In other words, the microscope measures the same electronic excitations in the N-th and $(N+1)$-th lenses, but in the $(N+1)$-th lens the eigenstates are readjusted due to the incorporation of the high-energy excitation processes into the low-lying excitation processes. Conceptually, this procedure is identical to the coarse-grain transformation performed in the Poor Man's scaling discussed in Sec. 2.1.

In the next subsection we shortly introduce the technical details of the fourth previous NRG steps for the single-impurity Anderson model defined in Eq. 2.11. The following subsections are based on Refs.[81,95,96] and.[97]

3.1.1.1 Logarithmic discretization

The NRG approach starts with the logarithmic discretization of the conduction band. The two dimensionless parameters $\Lambda > 1$ and $0 < z \leq 1$ defines a discrete logarithmic mesh with energies $\varepsilon^z_{\pm 0} = \pm D$ and $\varepsilon^z_{\pm j} = \pm D\Lambda^{1-j-z}$ $(j = 1, 2, ...)$. The sign $+/-$ represents the energies above/below the Fermi level. The parameter z, proposed in Ref.,[98] gives access to energies left out of the logarithmic mesh defined by the parameter Λ. For each interval $I^z_{\pm j} = [\varepsilon^z_{\pm(j+1)}, \varepsilon^z_{\pm j}]$ $(j = 0, 1, 2, ...)$, a single operator $a_{\pm j} = \int_{I_{\pm j}} c_k d\varepsilon_k/\gamma_j$ is defined, with γ_j being a normalization factor. Based on that, a complete orthonormal base is defined. Projecting conduction states in the discrete base

$$\sum_k \varepsilon_k c^\dagger_k c_k \rightarrow \sum_{m\pm} E_{\pm m} a^\dagger_{\pm m} a_{\pm m}, \tag{3.2}$$

where $E_{\pm m}$ is the discrete kinetic energy given by the alternative discretization procedure in Ref.[99]

3.1.1.2 Lanczos transformation

Next, the Lanczos transformation projects the conduction band into a tridiagonal diagonal Hamiltonian. The transformation reads

$$\sum_{m\pm} E_{\pm m} a^\dagger_{\pm m} a_{\pm m} \rightarrow \sum_{n=0}^{\infty} t_n \left(f^\dagger_n f_{n+1} + f^\dagger_{n+1} f_n \right), \tag{3.3}$$

where f_n's $(n = 0, 1, ...)$ form an orthonormal basis that replaces the operators $a_{m\pm}$'s $(m = 0, 1, ...)$. The codiagonal coefficients $t_n \propto \Lambda^{-n/2}$ and, for $z \neq 1$, t_n must be calculated numerically. The site f_0 is defined by

$$f_0 = \frac{1}{\sqrt{2}} \sum_k c_k = \frac{1}{\sqrt{2}} \sum_m \int_{\pm I_m} a_m, \tag{3.4}$$

and contains all information of the conduction states directly coupled to the impurity. Therefore, none information about the coupling between the impurity and the conduction states is lost along the iterative diagonalization procedure.

In the tridiagonal representation, or more simply Wilson's basis, the single-impurity Hamiltonian becomes

$$\mathcal{H}^N_{\mathrm{SIAM}} = \frac{1}{\mathcal{D}_N} \left[\sum_{n=0}^{N-1} t_n (f^\dagger_n f_{n+1} + \mathrm{H.c.}) + \varepsilon_d d^\dagger d \ + \mathcal{U} n_{d\uparrow} n_{d\downarrow} + \tilde{\mathcal{V}} (f^\dagger_0 d \ + \mathrm{H.c.}) \right], \tag{3.5}$$

where the conduction band was substituted by a tight-binding chain with hopping terms t_n. Different from Eq. 3.3, the tight-binding chain now has a finite number of sites. Such

restriction, known as infrared truncation, is necessary to make the Hamiltonian numerically tractable. In addition, the maximum iteration is achieved when the Hamiltonian in Eq. 3.5 become invariant under the RG transformation. Finally,

$$\mathcal{D}_N = D\frac{(1-\Lambda^{-1})}{\log\Lambda}\Lambda^{-(N-1)/2} \tag{3.6}$$

defines the reduced bandwidth at each iteration.

3.1.1.3 Iterative diagonalization and ultraviolet cut

The iterative diagonalization procedure follows the RG transformation

$$\mathcal{H}^{N+1}_{\text{SIAM}} \equiv \tau[\mathcal{H}^{N}_{\text{SIAM}}] = \sqrt{\Lambda}\mathcal{H}_N + \frac{t_N}{\mathcal{D}_N}(f^\dagger_{N+1}f_N + \text{H.c.}), \tag{3.7}$$

where $\mathcal{H}^{N+1}_{\text{SIAM}}$ is built up based on the information of $\mathcal{H}^{N}_{\text{SIAM}}$. This equation follows the same principle of the Eq. 3.1.

The iterative procedure starts in the iteration $N = -1$ with the diagonalization of the impurity Hamiltonian. As a result, four eigenvalues E^{-1}_m and four eigenvectos $|m\rangle_{-1}$ are easily obtained. At this stage, the matrix element ${}_{-1}\langle m|d^\dagger|n\rangle_{-1}$ between the eigenvectos of the Hamiltonian is calculated too. These quantities are necessary to calculate the next iteration and the spectral density of the quantum impurity.

The next iteration is composed by the following processes: i) the base set composed by the tensor product of the following four states $|0\rangle$, $f^\dagger_{0\uparrow}|0\rangle$, $f^\dagger_{0\downarrow}|0\rangle$ and $f^\dagger_{0\uparrow}f^\dagger_{0\downarrow}|0\rangle$ and the $|m\rangle$ states is built up; ii) the Hamiltonian is projected on the new states; iii) and it is diagonalized. After that, iv) all eigenvalues are re-scaled with respect to the ground state and the matrix elements v) ${}_N\langle m|d^\dagger|n\rangle_N$ and ${}_N\langle m|f^\dagger_N|n\rangle_N$ are calculated in the iteration $N = 0$. The same procedure is repeated until the Hamiltonian become invariant under RG transformation.

The exponential growth of the matrix dimension is controlled by the dimensionless parameters E_{UV}. This parameter, known as ultraviolet cutoff, controls the computational cost and accuracy of the numerical diagonalization. At the end of each iteration, only eigenvalues and eigenvectors with scaled energy $E^N_m/\mathcal{D}_N$ below E_{UV} are kept and used into the next iteration.

3.1.2 Symmetries

The numerical cost of the iterative diagonalization is reduced taking into account the symmetries and conserved quantities of the Hamiltonian. For example, the single-impurity Anderson Hamiltonian conserves: (i) the total charge

$$Q = (\hat{n}_d - 1) + \sum_n(\hat{n}_{f_n} - 1), \tag{3.8}$$

where $\hat{n}_d$ and $\hat{n}_{f_n}$ are, respectively, number operator of the impurity and the Wilson chain orbitals; and (ii) the $\mathrm{SU}(2)_{\mathrm{spin}}$ spin symmetry with total spin operator defined by

$$\vec{S} = \frac{1}{2}\sum_{\alpha\alpha'} d^{\dagger}_{\alpha}\vec{\sigma}_{\alpha\alpha'}d_{\alpha'} + \sum_{n}\frac{1}{2}\sum_{\alpha\alpha'} f^{\dagger}_{n\alpha}\vec{\sigma}_{\alpha\alpha'}f_{n\alpha'}, \tag{3.9}$$

where $\vec{\sigma}_{\alpha\alpha'}$ are the Pauli matrices. In both definitions, the sum over n runs over all sites of the Wilson chain. As $\mathcal{H}$, Q, $\vec{S}^2$ and S_z form a Complete Set of Commuting Observables (CSCO), the Hamiltonian is rewriting in sub-blocks defined by the quantum numbers Q and S. In addition, the S_z component is eliminated by the Wigner-Eckart theorem, in the absence of a magnetic field.

When the Hamiltonian becomes particle-hole symmetric, i.e., $\mathcal{U} = -2\varepsilon_d$, an additional conservation law arises: the conservation of isospin.[90,91] The isospin operator of a quantum impurity is defined by

$$\vec{I}_{\mathrm{Imp}} = \sum_{\alpha\alpha'} \eta^{\dagger}_{\alpha}\vec{\sigma}_{\alpha\alpha'}\eta_{\alpha'}, \tag{3.10}$$

where $\eta^{\dagger}$ is the Nambu spinor of the impurity defined by

$$\eta^{\dagger}_{\alpha} = \begin{pmatrix} d^{\dagger}_{\uparrow} \\ -d_{\downarrow} \end{pmatrix}. \tag{3.11}$$

The total isospin operator of the Wilson chain ($\vec{I}_{\text{W-chain}}$) conserves the same form of $\vec{I}_{\mathrm{Imp}}$, but, now there is a sum that runs over all the n indexes of the Wilson chain and the Nambu spinor is substituted by

$$\xi^{\dagger}_{n\alpha} = \begin{pmatrix} f^{\dagger}_{n\uparrow} \\ (-)^n f_{n\downarrow} \end{pmatrix}. \tag{3.12}$$

As $\vec{I}^2_{\mathrm{Total}}$ and I^z_{Total} commute with $\mathcal{H}$, Q, $\vec{S}^2$ and S_z, where $\vec{I}_{\mathrm{Total}} = \vec{I}_{\mathrm{Imp}} + \vec{I}_{\text{W-chain}}$, the isospin becomes a good quantum number whenever there is particle-hole symmetry. Like S_z, the I^z_{Total} contribution can be eliminated by the Wigner-Eckart theorem. The physical meaning of this symmetry can be understood looking for the components $I^{+} = d^{\dagger}_{\uparrow}d^{\dagger}_{\downarrow}$ and $I^{-} = (I^{+})^{\dagger}$ of the impurity, defined by $I^{\pm} = I^x \pm iI^y$. When the system is particle-hole symmetric, the energy necessary to create and destroy two particles are equal.

Other symmetries can be explored for more general Hamiltonian. For example, in the two-impurity Anderson model discussed in Chapter 4, the parity-symmetry between quantum impurity orbitals divides the Hamiltonian into two orthogonal subspaces given by the symmetric and antisymmetric linear combinations between the orbitals. Physically, the two-impurity orbitals recombine themselves in a bonding and antibonding orbitals.

3.1.3 Magnetic susceptibility

The magnetic susceptibility of the single-impurity Anderson model follows the standard definition

$$\frac{k_B T\chi}{(\mu_B g)^2} = \frac{1}{\mathcal{Z}}\sum_m \left(\exp(-\bar{\beta}E_m)\,\langle m|\,S_z^2\,|m\rangle\right) - \frac{1}{\mathcal{Z}_0}\sum_m \left(\exp(-\bar{\beta}E_m^0)_0\,\langle m|\,S_{0z}^2\,|m\rangle_0\right) \quad (3.13)$$

where $|m\rangle$ is the eigenstate of the truncated Hamiltonian $\mathcal{H}_{\mathrm{SIAM}}^N$ with eigenvalue E_m, while $|m\rangle_0$ is the eigenstate with eigenvalue E_m^0 of a non-interacting electron gas described by the first term in the right-hand side of Eq. 3.5. $\mathcal{Z}$ ($\mathcal{Z}_0$) is the partition function of the truncated (electron gas) Hamiltonian, $\bar{\beta} = \mathcal{D}_N/k_B T$, g is the gyromagnetic ratio and μ_B is the Bohr magneton. In the brakets, S_z and S_{0z} are, respectively, the total parallel component of the spin operator of the single-impurity Anderson model and the non-interacting electron gas.

Numerically, the magnetic susceptibility is given by the average between two NRG runs for $z = 0.5$ and $z = 1.0$. As discussed in Ref.,[100] the undesirable non-physical oscillations introduced by the logarithmic discretization are canceled out because the parameter z introduces a phase shift in the oscillations. As in the single-impurity Anderson model the oscillations are phase shifted by a factor π. The averaging over z cancels them out perfectly out and emulates the continuum limit.

3.1.4 Spectral density calculation

The spectral density calculation is based on the z-interleaved approach proposed in Ref.[98] Mathematically, the spectral density is defined by

$$\rho_d(\varepsilon) = \int_0^1 \rho_d(\varepsilon, z)dz \quad (3.14)$$

that is the integral of the spectral weight $\rho_d(\varepsilon, z)$ over the interval $0 \leq z \leq 1$. The parameter z was introduced by hand in the logarithmic discretization procedure in order to cover the whole energy interval of the conduction states. The main advantage of this extra discretization parameter is that it cancels the artifacts of the logarithmic discretization procedure, as discussed in Subsec. 3.1.3, and corrects the amplitude of the spectral density.

The spectral weight is given by

$$\rho(\varepsilon, z) = \begin{cases} \sum_{\mathrm{N}} \left|\langle \mathrm{N}|\,d^\dagger\,|\mathrm{GS}\rangle\right|^2 \delta(E_{\mathrm{N},z} - \varepsilon) & \varepsilon > 0 \\ \sum_{\mathrm{N}} \left|\langle \mathrm{N}|\,d\,\,|\mathrm{GS}\rangle\right|^2 \delta(E_{\mathrm{N},z} + \varepsilon) & \varepsilon < 0 \end{cases} \quad (3.15)$$

where $|\mathrm{GS}\rangle$ and $|\mathrm{N}\rangle$ are, respectively, the ground state and an excited state obtained via the NRG approach. This equation tell us that the positive and negative spectral weights are given by the creation of a particle and a hole into the impurity orbital, respectively.

Two technical details about the spectral density calculation have to be emphasized in this subsection. The first one is related to the numerical derivative in the denominator

of Eq. 3.15. In order to decrease the numerical error along the derivative, we run the NRG two for z and $z + \Delta z$, where Δz is an infinitesimal number. Along the calculation performed in Chap. 4, we consider $\Delta z = 10^{-5}$.

The second one is related to the numerical integration in Eq. 3.14. As we are dealing with discrete values of z, we have integrated out in intervals of 0.1. As the run for each z is totally independent of the others, all the states in a given sector (Q, S) must be enumerated order of increasing z. This is a very difficult task because if all symmetries and conserved quantities are not taken into account in the numerical implementation of the iterative diagonalization procedure, these states may cross each other as a function of z. This is not a problem for the single-impurity Anderson model because, as a rule, the diagonalization is implemented considering all the symmetries of the model. For example, let us suppose that the NRG was implemented taking into account only the charge and spin conservation. For the symmetric case, the states in each sector can cross because in the particle-hole symmetric regime the isospin operator is also conserved. In general, the crossing of different state is not a huge problem in the single-impurity Anderson model. However, for more complex system, it plays an important rule along the numerical integration.

Even though the NRG provide to us precise quantitative results in thermodynamic equilibrium, the method can not be applied for non-equilibrium problems. There are three key points that make NRG not work in the non-equilibrium regime: (i) the truncation procedure throws out important states along the iterative procedure; (ii) the nonphysical oscillations introduced by the logarithmic procedure does not cancel averaging over many values of z; and (iii) the Wilson chain is not a thermal reservoir.[101] To avoid such problems in non-equilibrium study, in the next section we discuss the Density Matrix Renormalization Group that allow us to describe the leads as a tight-binding chain and follows a different truncation procedure.

3.2 Density Matrix Renormalization Group

Density Matrix Renormalization Group (DMRG) is a powerful variational method that yields essentially exact results with relatively small computational efforts. Historically, DMRG has it origin in the context of the failure of real-space Renormalization group.[102] Steven White overcame this problem by building up a one dimensional chain iteratively.[75,103] The method starts with the minimum size of a system and gradually grows it iteratively. To keep the system numerically tractable, the truncation procedure is guided by the eigenvalues of the reduced density matrix. In more details, the one dimensional chain is bipartite in two orthogonal pieces via Schmidt decomposition, and the smallest eigenvalues of the reduced density matrix are integrated out. Following the previous scheme, DMRG was able to precisely optimize the computation of the ground

state of a many-body Hamiltonian.

The truncation procedure is better understood with reference to the von Neumann entanglement or entanglement entropy in the framework of Quantum information theory. The entanglement entropy is defined by

$$S_{A|B} = -\mathrm{Tr}\rho_A \log_2 \rho_A = -\sum_{\alpha} w_\alpha \log_2 w_\alpha \tag{3.16}$$

where ρ_A is the reduced density matrix of the block A connected with the block B. Via Eq. 3.16, the entanglement entropy decays logarithmically as a function of w_α. As DMRG truncation procedure traces out the smallest w_α, it conserves the maximum A-B entanglement of the system at each iteration.

The truncation scheme reflects the key difference between NRG and DMRG. While the first one controls the bonding dimension of the system integrating out the high-energy state, the second throw away the states with low entanglement between two bipartite subspaces. This truncation scheme allows DMRG to deal with system in the real-space representation and systems with mixed energy scales. The latter is found in the Hubbard Hamiltonian and non-equilibrium problems. Another difference between these two methods is that DMRG only provides the ground state of the system at zero temperature, while NRG provides information about the ground state and several low-lying excited states for the whole range of temperature.

3.2.1 Matrix product states and Matrix product operators

DMRG achieved its hegemony with its new formulation based on matrix product states (MPS) and matrix product operators (MPO).[76] Shortly, MPS and MPO are able to represent a huge vector and matrix as a product of tensors with smaller dimension. In addition, the new formulation optimizes the computational calculation and allows the graphic representation of the system. For example, Fig. 8 shows three different kinds of tensors that can compose an MPS. The tensor $A^{\sigma_i}_{a_i,a_{i+1}}$ is represented by a sphere, where the indexes σ_i and (a_i, a_{i+1}) represent, respectively, the local state space and the dimension of the tensor. These indexes are described by a solid line in Fig. 8. The left and right tensors describe the sites in the corner of a chain of MPS. Such representation can be easily extended to MPO with the addition of an extra index σ_i'. In more details, a MPO is represented by the tensor $W^{\sigma_i,\sigma_i'}_{b_i,b_{i+1}}$ in Fig. 9. The indexes (σ_i, σ_i') and (b_i, b_{i+1}) describe, respectively, the local state space and its respective dimension. The left and right tensors describe a corner operator. Based on the graphical representation, all the mathematical complexity can be substituted by friendly figures.

To illustrate the versatility of these tools, we start with a general definition of a many-body state

$$|\Psi\rangle = \sum_{\sigma_1,..,\sigma_L} c_{\sigma_1,..,\sigma_L} |\sigma_1,..,\sigma_L\rangle\,, \tag{3.17}$$

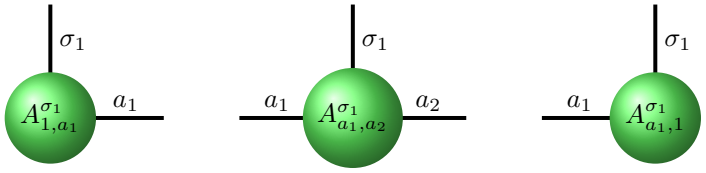

Figure 8 – Sketch of the $A-$tensors in the edge and middle of an MPS. The vertical solid lines describe the local degrees of freedom and the horizontal ones defines the dimension of each tensor.
Source: By the author.

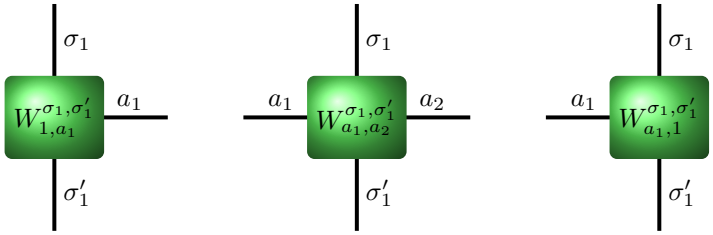

Figure 9 – Sketch of the $W-$tensors in the edge and middle of a one dimensional chain. The tensor W describes a local Hamiltonian that act in each bond of the MPS. The vertical solid lines describe the local degrees of freedom of each site and the vertical ones define the dimension of each tensor.
Source: By the author.

where $c_{\sigma_1,..,\sigma_L}$ are the coefficients and $\sigma_1,..,\sigma_L$ are the quantum numbers that describes the state. The previous state is rewritten in terms of an MPS via Singular Value Decomposition (SVD). This linear algebra tool decomposes a matrix M as a product of $USV^\dagger$, where U and V are two distinct matrix (or two distinct subspaces) with orthogonal columns and rows, respectively. In addition, S is a diagonal matrix with non-negative eigenvalues which describes the singular values. Such approach is directly recognized as a Schmidt decomposition, where U and V describe two independent subspaces and the singular values are eigenvalues of the reduced density matrix.

Applying SVD in Eq. 3.17, the coefficients $c_{\sigma_1,..,\sigma_L}$ are decomposed as

$$c_{\sigma_1,..,\sigma_L} = \sum_{a_1} U_{\sigma_1,a_1} S_{a_1,a_1} V^\dagger_{a_1,(\sigma_2,...,\sigma_L)} \equiv \sum_{a_1} U_{\sigma_1,a_1} c_{a_1,\sigma_2,..,\sigma_L} \equiv \sum_{a_1} A^{\sigma_1}_{1,a_1} c_{a_1,\sigma_2,..,\sigma_L}, \tag{3.18}$$

where it was decomposed in one MPS times a new state. After successive application of SVD, the state $|\Psi\rangle$ is defined by

$$|\Psi\rangle = \sum_{\boldsymbol{\sigma}} A^{\sigma_1}_{1,a_1} A^{\sigma_i}_{a_1,a_2} ... A^{\sigma_L}_{a_{L-1},1} |\boldsymbol{\sigma}\rangle \tag{3.19}$$

where $A^{\sigma_i}_{a_i,a_{i+1}}$ is a tensor that describes the i-th site of a 1D lattice. Such process is illustrated in Fig. 10.

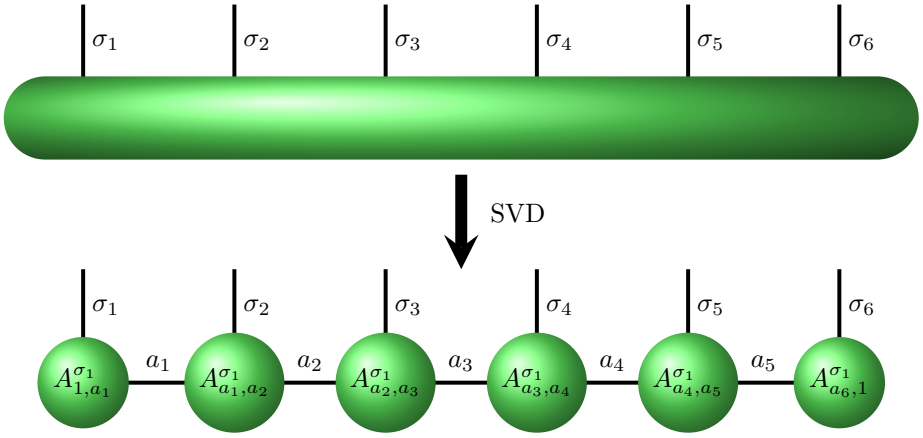

Figure 10 – Sketch of an arbitrary quantum state as an MPS. The vertical solid lines and the spheres represents, respectively, the states and the tensor that represents a local site of the real system.
Source: By the author.

The methematical representation of an operator as an MPO is given by

$$\hat{O} = \sum_{\boldsymbol{\sigma},\boldsymbol{\sigma'}} W^{\sigma_1,\sigma'_1}_{1,b_1} W^{\sigma_2,\sigma'_2}_{b_1,b_2} ... W^{\sigma_L,\sigma'_L}_{b_{L-1},1} \left|\boldsymbol{\sigma}\right\rangle \left\langle\boldsymbol{\sigma'}\right| \tag{3.20}$$

where $W^{\sigma_i,\sigma'_i}_{b_i,b_{i+1}}$ describes the i-th local operator. The main advantage of this approach is the numerical calculation of local and global physical properties. An example is illustrated in Fig. 11, where an MPO is being applied to an MPS. The shape of the MPS is maintained, however, the dimension of the local MPS is $(\tilde{a}_i, \tilde{a}_{i+1}) = (a_i b_i, a_{i+1} b_{i+1})$. In addition, the dimension of the MPS is truncated via Schmidt decomposition.

Different algorithms can be done based on DMRG ideas in the framework of MPS and MPO, such as the Ground State DMRG (GS-DMRG) and time-dependent DMRG (tDMRG). These two algorithms are discussed in the next subsections.

3.2.2 Ground state Density Matrix Renormalization group

GS-DMRG is defined via variational approach. First, an attempt for MPS with finite size and small dimension is defined and, thereafter, it is locally optimized via relation

$$\frac{\partial^2}{\partial A^{\sigma_i} \partial A^{\sigma_{i+1}}} \left(\left\langle \Psi \right| \mathcal{H} \left| \Psi \right\rangle - \lambda \left\langle \Psi \right| \left. \Psi \right\rangle \right) = 0 \tag{3.21}$$

where λ is a Lagrangian multiplier that describes the energy of the ground state. The local optimization on the MPS i and $i+1$ is illustrated in Fig. 12. Systematically, the GS optimization run from the left to right side of the MPS. The same procedure is done in the opposite direction. The back and forth procedure is called sweeps and, at each optimization step, a sparse matrix is diagonalized. Usually, ground state optimization procedure (or sweeps) are repeated until $\langle \mathcal{H}^2 \rangle - \langle \mathcal{H} \rangle^2$ be smaller than a certain precision.

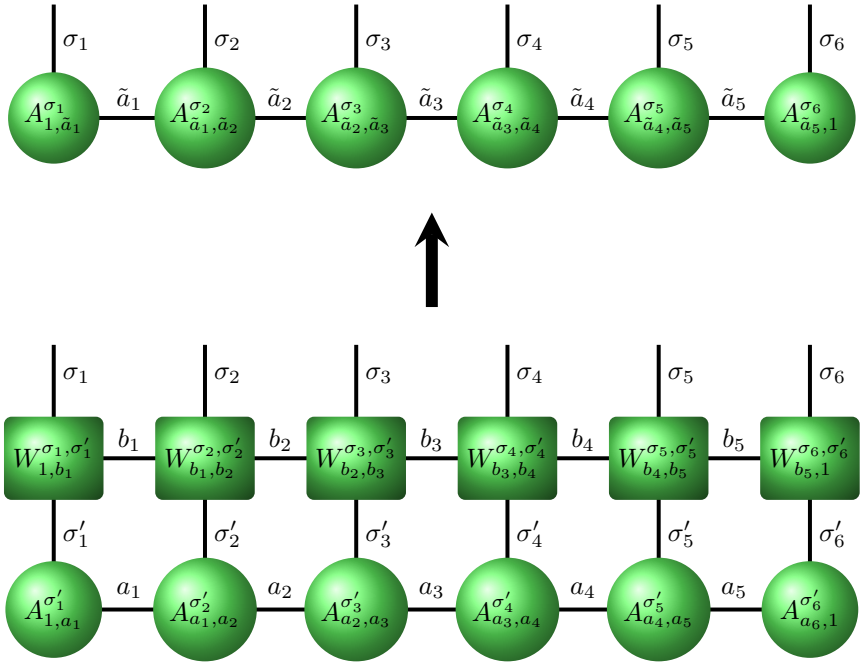

Figure 11 – Sketch of MPO acting on an MPS. Due to the contraction of the indexes σ'_i, a new MPS with same shape and with higher bond dimension is obtained, i.e., $(\tilde{a}_i, \tilde{a}_{i+1}) = (a_i b_i, a_{i+1} b_{i+1})$.
Source: By the author.

To control the exponential growth of the MPS bond dimension at each local optimization, the MPS must be truncated. To accomplish that, we employ the Schmidt decomposition to obtain the reduced density matrix of one side of the MPS connected to the other. Therefore, the truncation procedure integrates out the eigenvalues of the reduced density matrix lower than a predefined truncation error.

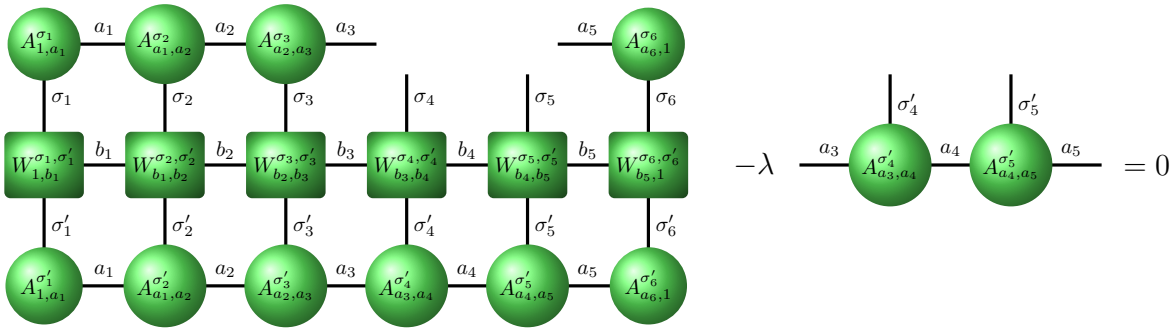

Figure 12 – Graphical representation of the MPS optimization via variational approach.
Source: By the author.

3.2.3 Time-dependent Density Matrix Renormalization group

Based on tDMRG, the optimal ground state MPS can be driven far-from-equilibrium via real-time evolution. The time-evolution is guided by the operator

$$e^{-i\mathcal{H}t}, \tag{3.22}$$

that is the time-evolution operator for real time. Due to the locality of the Hamiltonian operators, the time evolution is performed in the framework of the Suzuki-Trotter (ST) decomposition. ST decomposition exploits the locality of the Hamiltonian and decompose it terms that only act in the even and odd bonds of the MPS. Mathematically,

$$e^{-i\mathcal{H}t} \approx e^{-ih_{\text{even}}\delta t}e^{-ih_{\text{odd}}\delta t} + O(\delta t^2) \tag{3.23}$$

where $O(\delta t^2)$ is the error obtained by $[h_{\text{even}}, h_{\text{odd}}] \neq 0$ and it is known as ST error. The application of the time evolution operator illustrated in Fig. 13 is divided in two sweeps. In the first sweep, only h_{even} is applied in the MPS. Subsequently, start from left to right, another sweep time evolve the odd bonds of the MPS. At first order ST decomposition, these two sweeps evolve the MPS in one time step. In addition, via Schmidt decomposition, the bond dimension of the MPS is truncated.

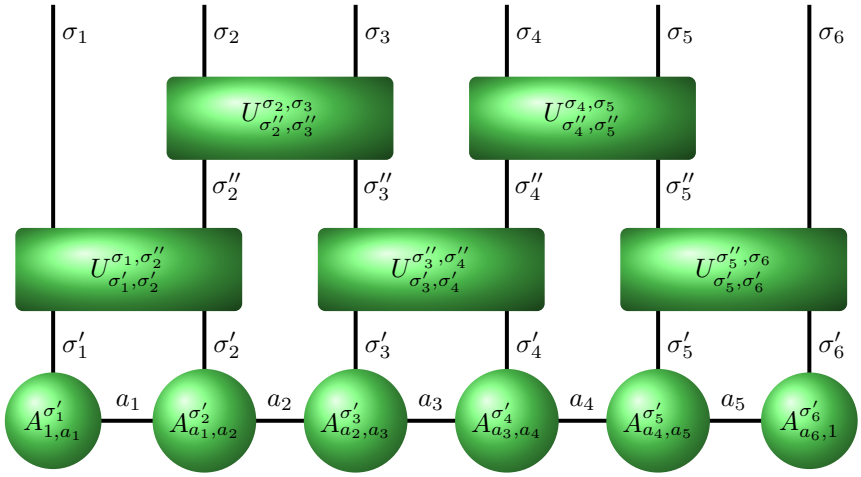

Figure 13 – Suzuki-Trotter decomposition illustration in MPS and MPO language. In the first order of the decomposition, the time evolution is performed in two sweeps. First, from left to right, only all odd bonds is time evolved. The time evolution of even bonds are performed by the sweeps in the opposite direction.
Source: By the author.

ST decomposition is a practical approach, however, at lower order of expansion it introduces huge error along the time evolution. The error is reduced going to higher orders of the ST decomposition. In this project, we go up to 4-th order ST decomposition[76] defined by

$$e^{-i\mathcal{H}\delta t} = \hat{U}(\delta t_1)\hat{U}(\delta t_2)\hat{U}(\delta t_3)\hat{U}(\delta t_2)\hat{U}(\delta t_1) \tag{3.24}$$

where

$$\hat{U}(\delta t_i) = e^{-ih_{\text{odd}}\delta t_i/2} e^{-ih_{\text{even}}\delta t_i} e^{-ih_{\text{odd}}\delta t_i/2} \tag{3.25}$$

and

$$\delta t_1 = \delta t_2 = \frac{1}{4 - 4^{1/3}}\delta t \quad \text{and} \quad \delta t_3 = \delta t - 2\delta t_1 - 2\delta t_2. \tag{3.26}$$

At this level, the ST error is of the order $O(\delta t^5)$.

4 CORRELATION EFFECTS IN THE EMERGENCE OF BOUND STATE IN THE CONTINUUM

In this chapter, we investigate the correlation effects in the emergence of a bound state in the continuum (BIC) in the framework of a two quantum dot device coupled to the edge of a quantum wire. The experimental setup displayed on Panel (a) of Fig. 14 is well described by the two-impurity Anderson model (TIAM). The spectrum of this model contains a Friedrich-Wintgen BIC[13] in the non-interacting limit. More generally, the model accounts for the electron-electron interaction between two localized electrons in the dots. To our knowledge, this is the simplest and most suitable platform to perform studies of the kind.

We organize this chapter as follows. First, we explicitly define the TIAM Hamiltonian and project it onto a bonding and antibonding basis. This representation provides a clear view of the correlation effects in the emergence of a BIC, as shown in Panel (b) of Fig. 14. In the non-interacting regime, the antibonding orbital becomes a BIC. As the Coulomb interaction grows, however, the antibonding orbital gradually couples to the bonding orbital and, indirectly, to the continuum.

Thereafter, in Sec. 4.2, we define the TIAM Hamiltonian in the Numerical Renormalization Group formalist. Specifically, this method is used to calculate the spectral density and the magnetic susceptibility of the bonding and antibonding orbital. While the first quantity provides information about the single-particle excitation spectrum of the two orbitals, the magnetic susceptibility probes the magnetic properties of the system. The latter is crucial to unveil the existence of a bound spin state in the continuum, which we prefer to call it by spin-BIC.

In Sec. 4.3, we identify the fixed points and the crossover between them in order to provide an overview about the physical regimes of the TIAM Hamiltonian. This section helps us to understand the numerical results in Sec. 4.4, where we show the spectral density and the magnetic susceptibility of the bonding and antibonding orbital. Both quantities are analyzed in the weak and strong coupling regime. While the first regime is dominated by the Coulomb interaction, the coupling energy dominates the second one.

4.1 Two-impurity Anderson Hamiltonian

To recover the Friedrich-Wintgen results in the non-interacting limit,[13] we consider two identical quantum dots equally coupled to the wire. In standard notation, the TIAM is described by the Hamiltonian

$$\mathcal{H}_{\mathrm{TIAM}} = \sum_{k} \varepsilon_k c_k^\dagger c_k + \varepsilon_d \sum_{j=1}^{2} d_j^\dagger d_j + \mathcal{U} \sum_{j=1}^{2} n_{d_j\uparrow} n_{d_j\downarrow} + \frac{\mathcal{V}}{\sqrt{\mathcal{N}}} \sum_{kj} (c_k^\dagger d_j + \mathrm{H.c.}). \tag{4.1}$$

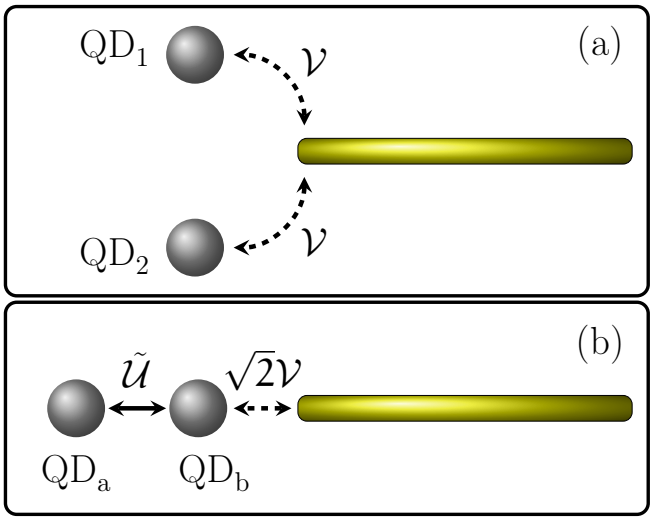

Figure 14 – (a) Schematic representation of two identical quantum dots (gray spheres) coupled to the edge of a quantum wire (yellow bar). The dashed arrows represent the coupling between the wire and the dots with hybridization amplitude $\mathcal{V}$. (b) Bonding (QD_b) and antibonding (QD_a) orbital presentation of the same system. The antibonding orbital is decoupled from the quantum wire, but it interacts with the bonding orbital. The Coulomb interaction $\tilde{\mathcal{U}}$, represented by the solid arrow, sets the strength of the interaction.
Source: By the author.

The first term on the right-hand side of Eq. 4.1 is a non-interacting, half-filled conduction band with bandwidth $2D$ and linear dispersion ε_k. The second and third terms represent the energy ε_d of the two dot levels d_j ($j = 1, 2$) and the Coulomb repulsion $\mathcal{U}$ resulting whenever one of them is doubly occupied. The final term couples the two dots to the conduction states. The sum over the spin index was not specified in Eq. 4.1.

4.1.1 Bonding and antibonding representation

Taking advantage of the parity symmetry between the orbitals $d_1 \leftrightarrow d_2$ exchange, the TIAM Hamiltonian can be rewritten in terms of the bonding (b) and antibonding (a) operators

$$d_{b/a} \equiv \frac{1}{\sqrt{2}}(d_1 \pm d_2), \tag{4.2}$$

defined by the symmetric and anti-symmetric linear combination of the quantum dots orbitals d_1 and d_2. Substitution of $d_{b/a}$ for d_1 and d_2 on the right-hand side of Eq. 4.1 yields a more instructive expression, which we prefer to write in the form

$$\mathcal{H}_{\text{TIAM}} = \mathcal{H}_b + \mathcal{H}_a + \mathcal{H}_{ab}, \tag{4.3}$$

where we have split the Hamiltonian into the three terms on the right-hand side, associated with the bonding orbital, the antibonding orbital, and the interaction between electrons in the two orbitals, respectively. Specifically, the first term on the right-hand side of Eq. 4.3

is a single-impurity Anderson Hamiltonian:

$$\mathcal{H}_b = \sum_k \varepsilon_k c_k^\dagger c_k + (\varepsilon_d + \frac{\mathcal{U}}{4}) d_b^\dagger d_b + \frac{\mathcal{U}}{2} n_{d_b\uparrow} n_{d_b\downarrow} + \sqrt{\frac{2}{N}} \mathcal{V} \sum_k (c_k^\dagger d_b + \text{H.c.}), \tag{4.4}$$

while the second term has the structure of the impurity Hamiltonian in the Anderson model:

$$\mathcal{H}_a = (\varepsilon_d + \frac{\mathcal{U}}{4}) d_a^\dagger d_a + \frac{\mathcal{U}}{2} n_{d_a\uparrow} n_{d_a\downarrow}. \tag{4.5}$$

Finally, the last term on the right-hand side of Eq. 4.3 comprises two cross-orbital contributions:

$$\mathcal{H}_{ab} = -\mathcal{U} \overrightarrow{S}_b \cdot \overrightarrow{S}_a + \mathcal{U} \overrightarrow{I}_b \cdot \overrightarrow{I}_a. \tag{4.6}$$

The two terms on the right-hand side of Eq. 4.6 define the spin-spin interaction and isospin-isospin interaction between the bonding and antibonding orbitals, respectively. In more detail, the last one is defined by

$$\overrightarrow{I}_a \cdot \overrightarrow{I}_b = \frac{1}{2} \left(I_+^b I_-^a + I_-^b I_+^a \right) + I_z^a I_z^b, \tag{4.7}$$

with

$$I_{j=b/a}^+ = d_{j\uparrow}^\dagger d_{j\downarrow}^\dagger, \tag{4.8}$$

$$I_{j=b/a}^- = d_{j\downarrow} d_{j\uparrow} \tag{4.9}$$

and

$$I_{j=b/a}^z = \frac{1}{2} \left(d_{j\uparrow}^\dagger d_{j\uparrow} + d_{j\downarrow}^\dagger d_{j\downarrow} - 1 \right). \tag{4.10}$$

This term characterizes the charge interaction between the orbitals. Specifically, the first term of the right-hand side of Eq. 4.7 couples an empty and a doubly occupied orbital. The second one corrects the energies of each orbital and describes the repulsive interaction between electrons with opposite spins in each orbital.

Panel (b) in Fig. 14 schematically depicts the structure of Eq. 4.3. The left sphere represents the antibonding orbital and, by extension, the antibonding Hamiltonian H_a. The sphere in the center represents the bonding orbital, which is coupled (double-headed dashed arrows) to the segment representing the quantum wire. The pair hence represents the bonding Hamiltonian H_b. Finally, the double-headed solid arrow represents the spin-spin and isospin-isospin interactions.

The previous simplifications allow us to verify that the spin of the antibonding orbital is conserved. Mathematically,

$$\left[\mathcal{H}_b + \mathcal{H}_a + \mathcal{H}_{ab}, \vec{S}_a^2 \right] = 0, \tag{4.11}$$

where $\overrightarrow{S}_a$ is the spin operator of the antibonding orbital. The spin conservation of the antibonding orbital divides the eigenstates of the TIAM Hamiltonian into two orthogonal subspaces given by the quantum numbers $s_a = 0$ and $s_a = 1/2$. As a result of the spin conservation, the inter-orbital Hamiltonian in Eq. 4.6 acts differently in each subspace. Since the antibonding orbital is always empty or doubly occupied for $s_a = 0$, only the isospin-isospin interaction plays an important role. Therefore, the low-lying eigenstates of the Hamiltonian are

$$|\text{Isopin}\rangle = \frac{1}{\sqrt{2}}(d^\dagger_{b\uparrow}d^\dagger_{b\downarrow} \mp d^\dagger_{a\uparrow}d^\dagger_{a\downarrow})\,|0\rangle\,, \tag{4.12}$$

which describes a singlet $(-)$ and a triplet $(+)$ isospin state. Since the isospin interaction is antiferromagnetic in $\mathcal{H}_{ab}$, the singlet has lower energy. In contrast, only the spin-spin interaction is non-zero for $s_a = 1/2$. Therefore, the eigenstates of this subspace are a composition of states defined by

$$|\text{Spin}\rangle = \frac{1}{\sqrt{2}}(d^\dagger_{b\uparrow}d^\dagger_{a\downarrow} \mp d^\dagger_{b\downarrow}d^\dagger_{a\uparrow})\,|0\rangle\,, \tag{4.13}$$

which describes a singlet $(-)$ and a triplet $(+)$. As the spin interaction between the orbitals is ferromagnetic, the triplet has lower energy.

4.2 Two-impurity Anderson Hamiltonian in the framework of the Numerical Renormalization group

Following the NRG procedure in Sec. 3.1, the truncated two-impurity Anderson Hamiltonian is defined by

$$\begin{aligned}\mathcal{H}^N_{\text{TIAM}} = \frac{1}{\mathcal{D}_N}\Bigg[&\sum_{n=0}^{N-1} t_n(f^\dagger_n f_{n+1} + \text{H.c.}) + (\varepsilon_d + \frac{\mathcal{U}}{4})d^\dagger_b d_b + \frac{\mathcal{U}}{2}n_{d_b\uparrow}n_{d_b\downarrow} \\ &+ \frac{2\mathcal{V}}{\sqrt{N}}(f^\dagger_0 d_b + \text{H.c.}) + \mathcal{H}_a + \mathcal{H}_{ab}\Bigg]\,,\end{aligned} \tag{4.14}$$

where the conduction band was substituted by a semi-infinity tight-binding chain with N sites. The first site of the chain is defined by $f_0 = \sum_k c_k/\sqrt{2}$, the hopping terms $t_n \propto \Lambda^{-n/2}$ and $\mathcal{D}_N$ is the reduced bandwidth defined in Eq. 3.6.

From NRG, the spectral function of the bonding and antibonding orbitals are obtained by

$$\rho_{b/a}(\varepsilon) = \int_0^1 \rho_{b/a}(\varepsilon, z)dz, \tag{4.15}$$

where $\rho_{b/a}(\varepsilon, z)$ is defined by

$$\rho_{b/a}(\varepsilon, z) = \begin{cases} \sum_{\text{N}} \left|\langle \text{N}|\, d^\dagger_{b/a}\,|\text{GS}\rangle\right|^2 \delta(E_{\text{N},z} - \varepsilon) & \varepsilon > 0 \\ \sum_{\text{N}} \left|\langle \text{N}|\, d_{b/a}\,|\text{GS}\rangle\right|^2 \delta(E_{\text{N},z} + \varepsilon) & \varepsilon < 0 \end{cases}. \tag{4.16}$$

In this equation, $|\mathrm{GS}\rangle$ and $|\mathrm{N}\rangle$ are, respectively, the ground state and the single-particle excited state obtained via NRG. The spectral density calculation follows Sec. 3.1.4.

The bonding and antibonding magnetic susceptibility can be obtained from the standard definition

$$\frac{k_B T\chi}{(\mu_B g)^2} = \frac{1}{\mathcal{Z}}\sum_m \left(\exp(-\bar{\beta}E_m)\,\langle m|\,S_z^2\,|m\rangle\right) - \frac{1}{\mathcal{Z}_0}\sum_m \left(\exp(-\bar{\beta}E_m^0)_0\,\langle m|\,S_z^2\,|m\rangle_0\right) \quad (4.17)$$

where $|m\rangle$ is the eigenstate of the truncated Hamiltonian $\mathcal{H}^N_{\mathrm{TIAM}}$ with eigenvalue E_m, while $|m\rangle_0$ is the eigenstate with eigenvalue E_m^0 of a non-interacting electron gas described by the first term in the right-hand side of Eq. 4.14. $\mathcal{Z}$ ($\mathcal{Z}_0$) is the partition function of the truncated (electron gas) Hamiltonian, $\bar{\beta} = \mathcal{D}_N/k_B T$, g is the gyromagnetic ratio and μ_B is the Bohr magneton. In both brakets, S_z is the total spin operator for each system. Since the trace of S_z operator is invariant under basis change, the magnetic susceptibility is the same in the bonding and antibonding or TIAM basis.

4.3 Fixed points

An overview of all physical regime of the truncated Hamiltonian in Eq. 4.14 is given by its different fixed points and the crossover between them under Renormalization Group transformation τ^2. This transformation is defined by

$$\mathcal{H}^{N+1}_{\mathrm{TIAM}} \equiv \tau[\mathcal{H}^N_{\mathrm{TIAM}}] = \Lambda\mathcal{H}^N_{\mathrm{TIAM}} + \frac{t_N}{\mathcal{D}_N}(f^\dagger_{N+1}f_N + \mathrm{H.c.}), \quad (4.18)$$

which takes the Hamiltonian $\mathcal{H}^N_{\mathrm{TIAM}}$ to $\mathcal{H}^{N+1}_{\mathrm{TIAM}}$. A fixed point results when the truncated Hamiltonian parameters $\varepsilon_d/\mathcal{D}_N$, $\mathcal{U}/\mathcal{D}_N$ e $\Gamma/\mathcal{D}_N$ have special values, such as 0 or $\pm\infty$. In these limits, the system become scale invariant under τ^2 transformation.

4.3.1 Free-electron Hamiltonian

A fixed point Hamiltonian obtained under τ^2 transformation can always be written in terms of non-interacting free-electron Hamiltonian plus a scattering potential. The single-particle Hamiltonian is defined by

$$\mathcal{H}_{W,N} = \frac{1}{\mathcal{D}_N}\left(2W f_0^\dagger f_0 + \sum_{n=0}^{N-1} t_n(f_n^\dagger f_{n+1} + \mathrm{H.c.})\right) \quad (4.19)$$

where the first and second terms are, respectively, a scattering potential with amplitude W and a non-interacting, half-filled conduction band with half-width D. As the Hamiltonian is quadratic, the eigenvalues and eigenvectors can be easily obtained by standard numerical diagonalization procedure. For odd N, the eigenvalues have the form

$$\eta_{j\pm} = \pm\Lambda^{j\mp\delta/\pi} \qquad (j = 0, 1, ..., (N-1)/2), \quad (4.20)$$

where δ is the phase shift induced by the scattering potential W. The connection between both quantities is

$$\tan\delta = -\pi\rho W, \tag{4.21}$$

with ρ being the density of state of the free-electron gas. For each fixed point, the eigenvalues of the single-particle Hamiltonian can be obtained by adjusting W so that one of the eigenvalues become identical to the first excited state obtained in the NRG run at a given iteration.

4.3.2 Fixed points for the two-impurity Anderson Hamiltonian

Table 2 summarizes the fixed points of the two-impurity Anderson model. All the fixed points were identified taking the asymptotic limit of the physical parameters Γ and the excitation amplitudes $\Delta_1 = -\varepsilon_d$ and $\Delta_2 = \varepsilon_d + \mathcal{U}$. The last two energies are, respectively, the energy to create a hole and a particle in each quantum dot orbital measured from the single-occupation configuration. Even though these two excitation energies were defined in terms of the parameters of the two quantum dots, all fixed points are explained in the bonding and antibonding basis.

A fixed point can be associated with a single-particle Hamiltonian with an (i) even and (ii) odd number of sites. To avoid redundancy, the number of sites in a single-particle Hamiltonian is not specified.

4.3.2.1 Weak coupling fixed points

The weak coupling fixed points are obtained whenever Γ is equal or approximately zero. Such limits are achieved in the high-temperature regime.

Free orbitals

Suppose that Γ, Δ_1 and Δ_2 are set equal to zero. The fixed point Hamiltonian $\mathcal{H}^*_{\mathrm{FO},N}$ is composed by a free electron gas plus two resonant states with zero energy. In this fixed point, each orbital can be empty, singly occupied with spin $\uparrow$ or $\downarrow$ or doubly occupied. These four configurations of each orbital generate 16 degenerate states. This results in a magnetic susceptibility with amplitude 1/4. In addition, this fixed point holds two BICs, because $\Gamma = 0$.

Local moments

Now suppose that $\Gamma = 0$, $\Delta_1 = \Delta_2 = \infty$. The fixed point Hamiltonian $\mathcal{H}^*_{\mathrm{LM},N}$ is composed by a free electron gas plus two singly occupied orbital. This configuration is a consequence of the strong intra-orbital Coulomb interaction and the high charge negativity of the bonding and antibonding orbitals. These two effects suppress the empty and doubly

Table 2 – Two-impurity Anderson Hamiltonian fixed points of the τ^2 Renormalization Group transformation.

Fixed point	Hamiltonian	Γ	Δ_1	Δ_2	$\frac{k_B T\chi}{(g\mu_B)^2}$
Free orbitals	$\mathcal{H}^*_{\mathrm{FO},N}$	0	0	0	1/4
Valence fluctuations	$\mathcal{H}^*_{\mathrm{VF},N}$	0	∞	0	1/3
Local moments	$\mathcal{H}^*_{\mathrm{LM},N}$	0	∞	Δ_1	1/2
Spin triplet	$\mathcal{H}^*_{\mathrm{ST},N}$	$\to 0$	∞	Δ_1	2/3
Frozen impurity orbitals	$\mathcal{H}^*_{\mathrm{FI},N}$	0	∞	$-\Delta_1$	0
Free antibonding orbital	$\mathcal{H}^*_{\mathrm{FAO},N}$	∞	0	0	1/8
Valence-fluctuation antibonding orbital	$\mathcal{H}^*_{\mathrm{AFV},N}$	∞	∞	0	1/6
Local-moment antibonding orbital	$\mathcal{H}^*_{\mathrm{ALM},N}$	∞	∞	Δ_1	1/4
Frozen impurity antibonding orbital	$\mathcal{H}^*_{\mathrm{AFI},N}$	∞	∞	$-\Delta_1$	0

Source: By the author.

occupied configurations. In addition, due to the strong inter-orbital interaction, the orbitals recombine in a quadruplet, equivalent to a degenerate spin singlet and a spin triplet state.

Spin triplet

For $\Delta_1 = \Delta_2 = \infty$ and infinitesimal Γ, the fixed point Hamiltonian $\mathcal{H}^*_{\mathrm{ST},N}$ is composed by a free electron gas plus a triplet state formed via ferromagnetic interaction between bonding and antibonding orbitals. In contrast with the local-moment fixed point, the hybridization between the bonding orbital and the continuum split up the singlet and triplet states, taking $k_B T\chi/(g\mu_B)^2 \to 2/3$.

Valence fluctuations

The Valence-fluctuation fixed point, labeled $\mathcal{H}^*_{\mathrm{VF},N}$, characterizes the limit in which two charge configurations of each orbital are degenerate. For example, setting $\Gamma = 0$, $\Delta_1 = \infty$ and $\Delta_2 = 0$, the simple and double occupied configuration become degenerate. Another configuration is defined by $\Gamma = 0$, $\Delta_1 = 0$ and $\Delta_2 = \infty$, where the empty and simply occupied configuration are degenerated.

Frozen impurity orbitals

For $\Gamma = 0$, $\Delta_1 = \infty$ and $\Delta_2 = -\infty$, $\mathcal{H}^*_{\mathrm{FI},N}$ is described by a free-electron Hamiltonian plus two frozen orbitals in the doubly occupied configuration. The same fixed point is described by the set of parameter $\Gamma = 0$, $\Delta_1 = -\infty$ e $\Delta_2 = \infty$. However, the orbitals are frozen in the empty configuration.

Strong coupling fixed point

The strong-coupling fixed point is described by $\Gamma \to \infty$. This limit is reached in the low-temperature limit, for $k_BT \ll \Gamma$, $\Gamma \gg \mathcal{U}$ and $\Gamma \gg \varepsilon_d$ or $k_BT \ll k_BT_K$ and $\mathcal{U} \gg |\varepsilon_d| \gg \Gamma$, for $\varepsilon_d < 0$.

Free antibonding orbital

The Free antibonding orbital fixed point is defined by $\Gamma = \infty$, $\Delta_1 = 0$ e $\Delta_2 = 0$. At this fixed point, the bonding orbital is diluted in the continuum due to the strong coupling between them. Therefore, $\mathcal{H}^*_{\mathrm{FAO},N}$ is described by a free electron gas with the antibonding orbital decoupled from the continuum, i.e., the antibonding orbital becomes a BIC.

Local-moment antibonding orbital

$\Gamma = \Delta_1 = \Delta_2 = \infty$ defines the local-moment antibonding orbital fixed point, which can also be called as spin-BIC fixed point. $\mathcal{H}^*_{\mathrm{ALM},N}$ describes a free electron gas plus the decoupled antibonding orbital, or just a spin-BIC. These conclusions are ratified in Sec. 4.4.

Frozen impurity antibonding orbital

In the frozen-impurity antibonding orbital fixed point only the antibonding orbital is frozen in an empty or doubly occupied configuration. This fixed point is defined by $\Gamma = \infty$, $\Delta_1 = \infty$ e $\Delta_2 = -\infty$ for the doubly occupied antibonding orbital or $\Gamma = \infty$, $\Delta_1 = -\infty$ and $\Delta_2 = \infty$ for the empty antibonding orbital. Even though the bonding orbital is diluted into the continuum, the antibonding orbital still coupled to the continuum due to the isospin-isospin interaction defined in Eq. 4.6. Therefore, $\mathcal{H}^*_{\mathrm{AFI},N}$ is composed by a free electron Hamiltonian plus an extra scattering potential induced by the doubly occupied antibonding orbital.

Valence-fluctuation antibonding orbital

Suppose that $\Gamma = \infty$, $\Delta_1 = \infty$ and $\Delta_2 = 0$. The resulting Hamiltonian, which is donated by $\mathcal{H}^*_{\mathrm{AVF},N}$, is a free electron Hamiltonian plus an extra scattering potential. The particle-hole asymmetry is a result of the degenerescence between the singly and doubly

occupied configurations of the antibonding orbital. In contrast, for $\Gamma = \infty$, $\Delta_1 = 0$ and $\Delta_2 = \infty$, the empty and single occupied configuration are degenerate.

4.3.3 Crossover mechanisms and fixed point instability

The truncated Hamiltonian shown in Eq. 4.14 can cross over: (I) from the weak to strong coupling fixed points; (II) from the free-orbital fixed points to the other four fixed points shown on Table 2 with $\Gamma = 0$; and (III) from the free antibonding-orbital fixed points to the other three fixed points on Table 2 with $\Gamma = \infty$.

The first type of crossover is governed by the renormalization of the hybridization operator of the truncated Hamiltonian. For $\Gamma \gg |\varepsilon_d|$ and $\Gamma \gg \mathcal{U}$, the hybridization goes to infinity as soon as $k_B T \ll \Gamma$. In this regime, the bonding orbital is hybridized into the continuum. In the opposite regime, for $\Gamma \ll |\varepsilon_d| \ll \mathcal{U}$ and $\varepsilon_d < 0$, the crossover is driven by a Kondo-type Hamiltonian that screens the local moment of the bonding orbital, for $k_B T \lesssim k_B T_K$.

In the weak coupling regime, the truncated Hamiltonian shown in Eq. 4.14 can only cross over from the free orbitals to the other four fixed points with $\Gamma = 0$ shown on Table 2. This crossover is driven by renormalization of the parameters ε_d and $\mathcal{U}$ of the truncated Hamiltonian. In the opposite coupling regime, as the bonding orbital was coupled to the conduction band, the parameters ε_d and $\mathcal{U}$ only modifies the energy configurations of the antibonding orbital. Therefore, the renormalization of these parameters drives the system from the free antibonding orbital to the other three fixed points on Table 2 with $\Gamma = \infty$.

4.4 Numerical results

In this section we analyze the magnetic susceptibility and spectral density of the bonding and antibonding orbitals calculated in the various NRG runs. As the cross-orbital Hamiltonian is the only mechanism that couples the antibonding orbital with the continuum, in this section we fix ε_d and Γ and vary $\mathcal{U}$ from 0 to $-2\varepsilon_d$. This set of parameters provides an initial configuration that holds a BIC ($\mathcal{U} = 0$) and includes the correlation effects for finite $\mathcal{U}$. In addition, we investigate the weak ($\Gamma \ll |\varepsilon_d|$) and strong ($\Gamma \gg |\varepsilon_d|$) coupling regime, for $\varepsilon_d < 0$.

Table 3 summarizes the representative cases investigated in this section. We fix the energy level $\varepsilon_d = -2 \times 10^{-5} D$ and the amplitude of the coupling energy $\Gamma = 5 \times 10^{-7} D$ and $\Gamma = 5 \times 10^{-3} D$ for the weak and strong coupling regime, respectively. The choice of the small amplitudes of the physical parameters was motivated by the precision of the numerical calculations of the spectral density. As pointed out in Sec. 3.1, the logarithmic discretization of the conduction band provides a precise spectrum for $\varepsilon \ll D$. We should emphasize that all results presented in this section are general and can be reproduced for larger parameters if the ratio between ε_d, $\mathcal{U}$ and Γ are kept constant.

The NRG calculations in this section were carried out with $\Lambda = 5$ and the ultraviolet-cut 30. For the magnetic susceptibility, we have averaged two NRG runs for $z = 0.5$ e $z = 1.0$ in order to minimize the artificial oscillations introduced by the logarithmic discretization. The continuum limit of the spectral density was achieved by integrating z from 0 to 1, for $\Delta z = 0.1$.

Table 3 – Representative cases studied in the weak and strong coupling regime for fixed ε_d and Γ. Setting $\varepsilon_d = -2 \times 10^{-5} D$, $\Gamma = 5 \times 10^{-7} D$ and $\Gamma = 5 \times 10^{-3} D$ defines, respectively, the weak (W) and strong (S) coupling regime.

$\Gamma \ll \lvert\varepsilon_d\rvert$		$\Gamma \gg \lvert\varepsilon_d\rvert$	
Runs	$10^5 \times \mathcal{U}/D$	Runs	$10^5 \times \mathcal{U}/D$
W_a	0.00	S_a	0.00
W_b	2.10	S_b	2.66
W_c	2.20	S_c	2.67
W_d	2.50	S_d	4.00
W_e	4.00		

Source: By the author.

4.4.1 Non-interacting regime: Friedrich-Wintgen bound state in the continuum

In the non-interacting regime, the intra and inter-orbital interaction vanishes in Eqs. 4.4-4.6 and the bonding and antibonding orbital become resonant states with semi-width 2Γ and 0, respectively. The spectral density shown in Panels (a) and (b) of Fig. 15 for the set of parameters W_a and S_a confirms this behavior. In both cases, the spectral function of the bonding orbital is a Lorentzian

$$\rho_b(\varepsilon) = \frac{1}{\pi} \frac{\Gamma}{(\varepsilon - \varepsilon_d)^2 + \Gamma^2}, \tag{4.22}$$

with halfwidth 2Γ, while the antibonding orbital is a Dirac delta function $\rho_a = \delta(\varepsilon - \varepsilon_d)$. The delta-function behavior proves that the antibonding orbital is decoupled from the rest of the system. The decoupling occurs because the cross-orbital Hamiltonian $\mathcal{H}_{ab}$ vanishes for $\mathcal{U} = 0$. This result can be also illustrated taking $\tilde{\mathcal{U}} = 0$ in Panel (b) of Fig. 14. As the antibonding orbital is in the continuum energy region, we conclude that the antibonding orbital is a Friedrich-Wintgen BIC.

This is not a surprising result, since in the non-interacting limit the TIAM reduces to the Friedrich and Wintgen's model.[13] However, it provides an excellent starting point

for investigating the correlation effects in the emergence of a BIC, because the cross-orbital Hamiltonian $\mathcal{H}_{ab}$ is the only mechanism that couples the antibonding orbital to the rest of the system, for $\mathcal{U} \neq 0$.

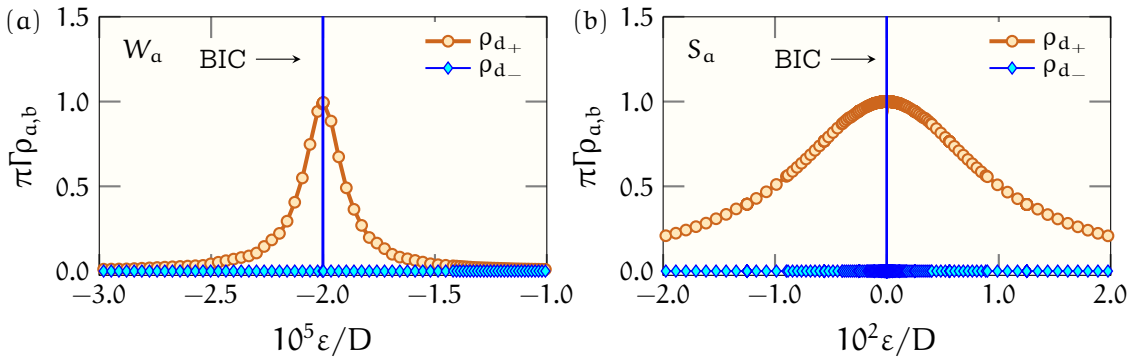

Figure 15 – Panels (a) and (b) displays, respectively, the bonding and antibonding spectral density for the cases W_a and S_a.
Source: By the author.

4.4.2 Interacting regime

The bonding and antibonding representation provides a clear interpretation of the correlation effects in the formation of BICs. The intra-orbital interaction on the right-hand sides of Eqs. 4.4 and 4.5 corrects the energy levels and favor the formation of local moments in the bonding and antibonding orbitals. The cross-orbital Hamiltonian is the only mechanism that couples the antibonding to the bonding orbital and hence, indirectly, to the conduction state. Therefore, as $\mathcal{U}$ grows, the inter-orbital Hamiltonian intensifies the coupling between the antibonding orbital and the continuum.

4.4.2.1 Bonding and antibonding spectral density in the weak coupling regime

In the weak coupling regime, the Coulomb interaction: (I) favors the formation of local moment in both orbitals; (II) induces the Kondo effect in the bonding orbital; (III) indirectly connects the antibonding orbital with the continuum; and (IV) results in threshold behavior in the spectral density of the antibonding orbital. The latter is discussed in Subsec. 4.4.2.3.

Fig. 16 shows the bonding orbital spectral density for the representative cases W_b-W_e. As the bonding orbital is directly connected to the continuum, it follows the same behavior as the single-impurity Anderson model. As $\mathcal{U}$ grows, the resonant state displayed in Panel (a) of Fig. 15 is spit in two states with energy $\Delta_{b_1} = -\varepsilon_{d_b}$ and $\Delta_{b_2} = \varepsilon_{d_b} + \mathcal{U}_b$, where ε_{d_b} is the effective energy and $\mathcal{U}_b$ is the effective intra-orbital Coulomb interaction in the bonding orbital. Both parameters can be identified in the plots. Δ_{b_1} and Δ_{b_2} are the excitation energy of a hole and an particle from the simple occupied configuration in the bonding orbital. For $\mathcal{U} \neq 0$, the excitation energies become different and appear as

two Lorentzians. In addition, if $\mathcal{U}_b$ is strong enough to inhibit the weight of the doubly occupied configuration, the Kondo peak pinned at zero energy pops up. Although the bonding orbital is the source of a rich physics produced by strong correlation effects, it does provide no information about the BIC physics, because the bonding and antibonding orbitals have opposite parity symmetry.

Painel (a) in Fig. 16 displays run W_b, which is the only representative case in which the Kondo peak is absent because the ground state has even-parity symmetry. For this set of parameters, the bounding orbital is in the valence-fluctuation regime, where the simply and double occupied configuration are quasi-degenerate, i.e., $\Delta_{b_2} \approx 0$. As the excitation energy decreases, the doubly occupied configuration becomes less energetic, as a result of the renormalization of the bonding orbital energy by the Haldane effect.[104] As only the isospin-isospin iteration between the orbitals is relevant when one of them is doubly occupied, the ground state becomes a non-magnetic isospin singlet.

The Hubbard peaks in runs W_c, W_d and W_e are similar to the peak in to run W_b. As $\mathcal{U}$ grows, only Δ_{b_2} increases and takes the second Hubbard peak to higher energies. However, as the Coulomb interaction lowers the single occupied configuration, a local moment is formed in the bonding orbital. At low temperature, the conduction states strongly couple to this local moment in order to cancel it out. This effect originates the Kondo peak at zero energy. Even though the Kondo peaks in the runs W_c, W_d and W_e look like a delta function, they have halfwidth of the same order as the Kondo temperature. Specifically, the Kondo temperature are, respectively, $k_B T_K/|\varepsilon_d| = 6.3 \times 10^{-4}$, 7.6×10^{-7} and 6.9×10^{-15} for runs W_c, W_d and W_e.

Panels (a)-(d) in Fig. 17 display the spectral density of the antibonding orbital for runs W_b-W_e. The plots show that the delta-function behavior previously observed in Panel (a) of Fig.15 in the non-interaction regime is absent, due to the action of the cross-orbital Hamiltonian $\mathcal{H}_{ab}$. As a result of the broadening of the antibonding spectral density, we conclude that cross-orbital Hamiltonian $\mathcal{H}_{ab}$ destroys the BIC. We must emphasize that this behavior is expected even for infinitesimal amplitudes of the Coulomb interaction, because $\mathcal{H}_{ab}$ mixes the subspaces with even and odd parity. Such conclusion follows from the definition of a BIC as a state with zero width.

In addition, the antibonding orbital splits into two resonant states with energy $\Delta_{a_1} = -\varepsilon_{d_a}$ and $\Delta_{a_2} = \varepsilon_{d_a} + \mathcal{U}_a$ as shown in the four panels of Fig. 17. By definition, ε_{d_a} is the effective energy and $\mathcal{U}_a$ is the effective amplitude of the Coulomb interaction of the antibonding orbital. These two parameters are obtained numerically and describe the excitation processes that creates a hole and an electron in the antibonding orbital.

Finally, the antibonding orbital spectral function also displays a singular behavior, followed by an abrupt drop for $|\varepsilon| < \varepsilon_T$. The threshold energy ε_T is given by the energy difference between the ground state and the lowest energy excited state with symmetry

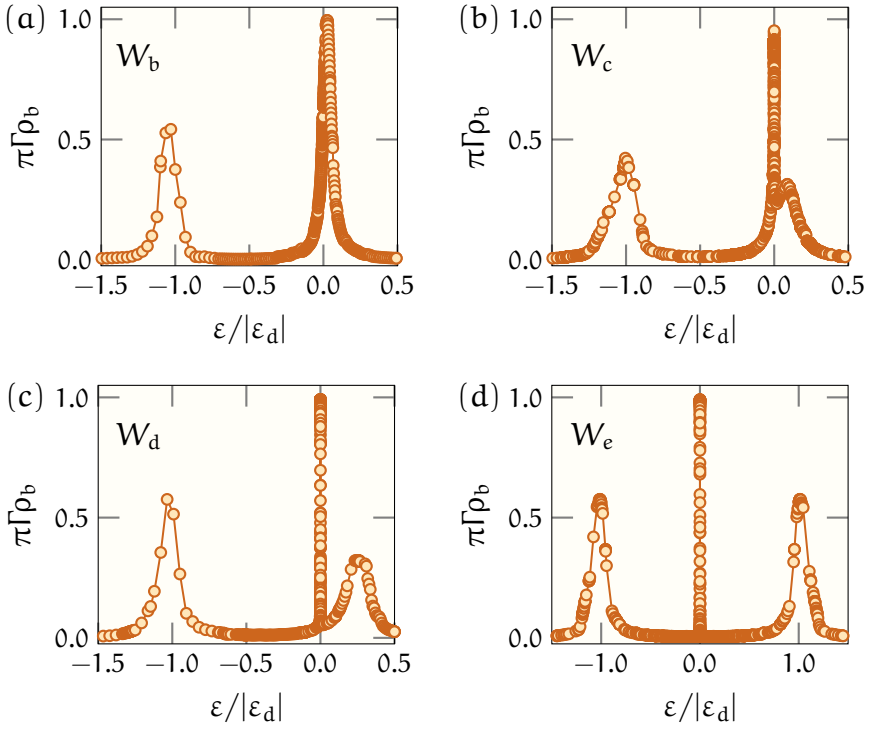

Figure 16 – Panels (a)-(d) shows the spectral density of the bonding orbital for the representative cases W_b, W_c, W_d and W_e.
Source: By the author.

opposite. This behavior, similar to the x-ray singularity problem and emerges due to the existence between two orthogonal subspaces in the TIAM Hamiltonian. More details about that in Subsec. 4.4.2.3.

4.4.2.2 Bonding and antibonding spectral density in the strong coupling regime

In the strong coupling regime, the bonding orbital is invariant under the effect of the intra-orbital Coulomb interaction on the right-hand side of Eq. 4.4. Therefore, it is always described by a resonant state as the one displayed in the inset of Panel (a) of Fig. 18 for the run S_b. The spectral densities of the bonding orbital for runs S_c and S_d are not shown because they are identical to case S_b. In addition, they do not bring any insight concerning BIC physics.

Even though the inter-orbital Coulomb interaction defined in Eq. 4.3 be much smaller than Γ, this Hamiltonian mixes the antibonding orbital with the continuum. Panels (a)-(c) in Fig. 18 shows the broadening in the antibonding spectral density originated by the inter-orbital Coulomb interaction. Another characteristic of this limit is that the excitation energies of the antibonding orbital are only due to $\mathcal{H}_a$ in Eq. 4.5. Therefore, the numerical data confirms that $\Delta_{1_a} = -(\varepsilon_d + \mathcal{U}/4)$ e $\Delta_{2_a} = \varepsilon_d + 3\mathcal{U}/4$, as set by the singly occupied configuration.

Finally, a threshold behavior, similar to the one discussed in Subsec. 4.4.2.2, is

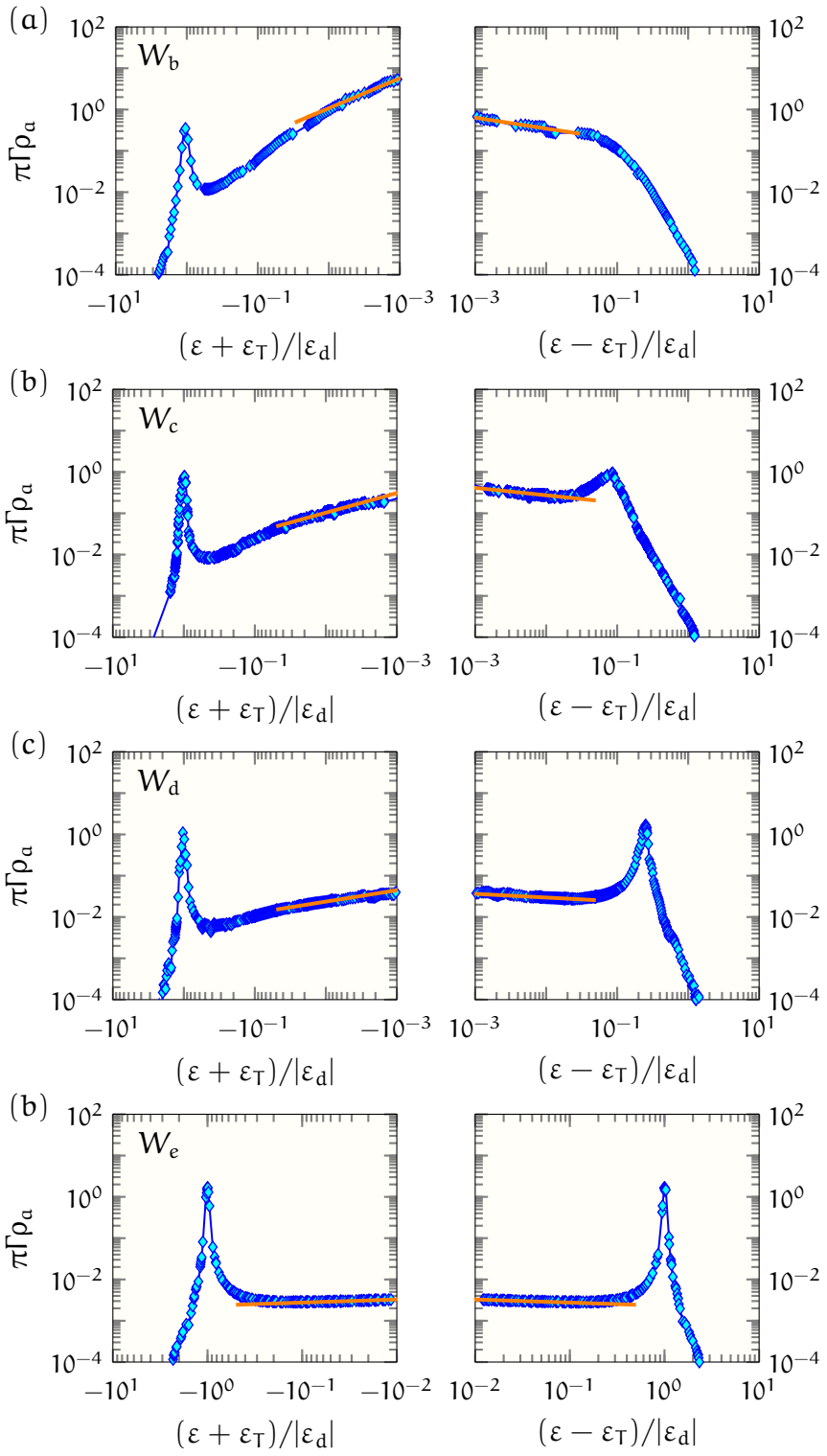

Figure 17 – Antibonding orbital spectral density in the weak coupling regime. Panels (a)-(d) shows the antibonding spectral function for the representative cases W_b, W_c, W_d e W_e. Solid orange lines describes the power law behavior $\rho_a(\varepsilon \to \varepsilon_T) = A/(|\varepsilon| - \varepsilon_T)^{\alpha_N}$ for a set of parameters summarized in Table 4.
Source: By the author.

observed in the antibonding spectral function for energy lower than $\varepsilon_T = \Delta_{2_a}$. More details

are given in the next subsection.

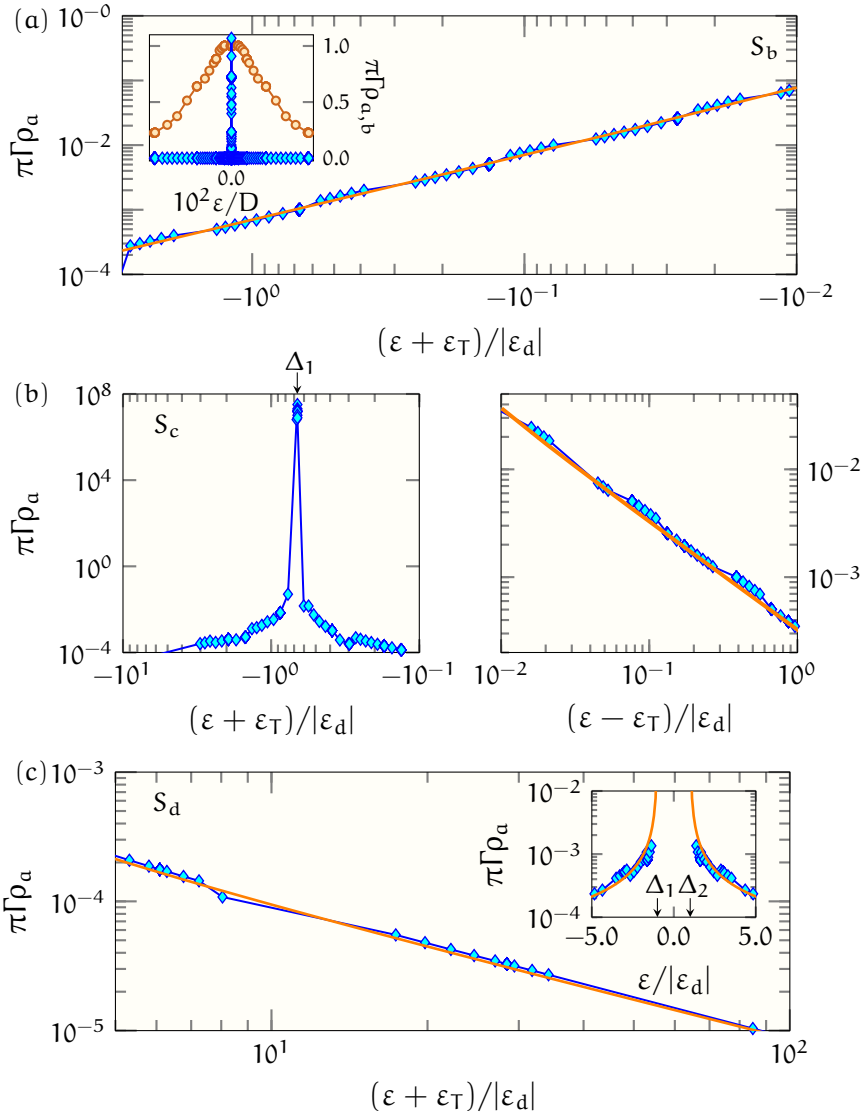

Figure 18 – Panels (a)-(c) display the spectral density of the antibonding orbital in the log-log scale for the cases S_b, S_c e S_d. The solid orange lines reproduces the singular described by $\rho_a(\varepsilon \to \varepsilon_T) = A/(|\varepsilon| - \varepsilon_T)$ for a set of parameters summarized in Table 5. The inset in the upper-left side of Panel (a) shows the bonding (orange circles) and antibonding (blue diamonds) spectral density in the linear-linear scale.
Source: By the author.

4.4.2.3 X-ray singularity: Nozières-De Dominicis and Doniach-Sunjic power laws

In the previous subsections, the singular behavior, followed by an abrupt decay resulted from the division of the eigenstates of the TIAM Hamiltonian in sub-spaces with even and odd parities. This division is related to the spin conservation $\vec{S}_a^2$ of the antibonding orbital and, consequently, the parity symmetry. The connection between these

two sub-spaces is given by $\rho_a(\varepsilon)$, in which $\langle \mathrm{N}| \, d_a^\dagger \, |\mathrm{GS}\rangle$ connects the ground state with the low-lying excited states with opposite symmetry.

For example, let us take the non-interacting regime. As the antibonding orbital is doubly occupied, the ground state has even parity. Therefore, the matrix element $\langle \mathrm{N}| \, d_a^\dagger \, |\mathrm{GS}\rangle$ connects the ground state with the first excited state with an extra particle in the antibonding orbital. Because the antibonding orbital is a BIC, there is only one nonzero matrix element, at energy $\varepsilon = \varepsilon_d$. This example can be extended to the interacting regime. As $\mathcal{U}$ grows, the cross-orbital Hamiltonian $\mathcal{H}_{ab}$ mix both subspace and, consequently, new finite matrix elements pop up in $\rho_a(\varepsilon)$. The threshold behavior happens when the excitation energy ε is not high enough to excite an electron or a hole in the antibonding orbital. As all excited states with odd parity symmetry vanish for $|\varepsilon| < \varepsilon_T$, the spectral function abruptly drops to zero. This mechanism creates a gap in the antibonding orbital spectral density. We can conclude that in the limit $\varepsilon \to 0$, there is only a single component of the antibonding orbital in ground state. By contrast, $\rho_b(\varepsilon)$ is continuous at $|\varepsilon| = \varepsilon_T$ because $\langle \mathrm{N}| \, d_b^\dagger \, |\mathrm{GS}\rangle$ connects states with same symmetry, and the bonding orbital is directly connected to the continuum.

For $|\varepsilon| > \varepsilon_T$, the antibonding orbital spectral density mimics the singularities observed in the photoemission and photoabsorption x-ray problems. The singular behavior can be reproduced by the equation

$$\rho_a(\varepsilon) = \begin{cases} A/(\varepsilon - \varepsilon_T)^\alpha & |\varepsilon| > \varepsilon_T \\ 0 & |\varepsilon| < \varepsilon_T \end{cases} \tag{4.23}$$

where A and α are non-universal parameters obtained from the fit of the antibonding orbital spectral density in Figs. 17 and 18.

In the weak coupling regime, the singular behavior is associated with Nozières-De Dominicis expression, where the critical exponent is given by

$$\alpha \equiv \alpha_N = 2\beta(1-\beta) \tag{4.24}$$

for $\beta \equiv (\bar{\delta} - \delta)/\pi$. δ and $\bar{\delta}$ are, respectively, the phase shifts of a single particle Hamiltonian, as the one shown in Eq. 4.19, that reproduces the excited states $|\mathrm{N}\rangle$ and the ground state $|\mathrm{GS}\rangle$. Nozières-De Dominicis power law tells that α_N can vary from 0 to 1 for positive β due to the strong interaction between the antibonding orbital and the continuum. The numerical data in Table 4 agrees with that theory.

Even though the singular behavior follows the same form shown in Eq. 4.23 in the strong coupling regime, the critical exponent is given by Doniach-Sunjic power law, where

$$\alpha \equiv \alpha_D = 1 - 2\beta^2 \tag{4.25}$$

and $\beta \equiv (\bar{\delta} - \delta)/\pi$. In the Doniach-Sunjic formulation, the x-ray singularity is a consequence of a state decoupled from the continuum. In this formulation, $\beta \approx 0$ and $\alpha_D = 1$. As

Table 4 – Set of parameters used in Eq. 4.23 to fit the spectral density of the antibonding orbital in the weak coupling regime.

	Negative energy		Positive energy		
Runs	A	α_N	A	α_N	ε_{T}
W_a	–	–	–	–	–
W_b	1.5×10^{-5}	0.725	6.0×10^{-3}	0.263	3.5×10^{-8}
W_c	6.8×10^{-5}	0.475	1.7×10^{-2}	0.180	4.0×10^{-8}
W_d	3.4×10^{-4}	0.275	7.4×10^{-3}	0.090	4.0×10^{-8}
W_e	1.3×10^{-3}	0.075	1.3×10^{-3}	0.075	3.5×10^{-8}

Source: By the author.

summarized in the Table 5, the antibonding orbital spectral density in Eq. 18 agrees with Doniach-Sunjic formulation and emphasizes that the antibonding orbital is weakly coupled to the continuum in the strong coupling regime.

Table 5 – Set of parameters used in Eq. 4.23 to fit the spectral density of the antibonding orbital in the strong coupling regime.

	Negative energy		Positive energy		
Runs	A	α	A	α	ε_{T}
S_a	–	–	–	–	–
S_b	1.3×10^{-8}	1.000	–	–	1.25×10^{-8}
S_c	–	–	6.5×10^{-9}	1.000	2.5×10^{-8}
S_d	1.8×10^{-8}	1.000	1.8×10^{-8}	1.000	1.0×10^{-5}

Source: By the author.

The threshold behavior discussed in this subsection show us that the ground state is composed by an isolated component of the antibonding orbital for $\varepsilon \to 0$. This conclusion forces us to investigate the ground state properties of the TIAM Hamiltonian at zero temperature via magnetic susceptibility, because the spectral density does not provide the necessary information. To anticipate the discussion in the next section, we figure out that the ground state can be simply or double occupied in cases W_a-W_e and S_a-S_d. In the doubly occupied configuration, the ground state has even parity and the antibonding orbital is strongly coupled to the continuum only by the isospin-isospin interaction. However, in the simply occupied configuration, the ground state is composed by the singly occupied antibonding orbital that only connects to the continuum via spin-spin interaction. As the

latter one is ferromagnetic, the simple occupied configuration of the antibonding orbital decouples from the continuum at $k_BT \to 0$. In this limit, the antibonding orbital become a bound spin state in the continuum (spin-BIC).

4.4.3 Magnetic properties

As the spectral density is unable to track the properties of antibonding orbital at zero energy, in this subsection we investigate the ground state properties of the TIAM Hamiltonian via magnetic susceptibility. Although it does not separately provide the information about each orbital, we are able to map the contribution of each orbital in the magnetic susceptibility via eigenstate analyses. In addition, this quantity unveils a quantum phase transition as a function of the Coulomb interaction and the emergence of a bound spin-state in the continuum whenever the antibonding orbital is simply occupied.

4.4.3.1 Quantum phase transition

Panels (a) and (b) of Fig. 19 display the magnetic susceptibility as a function of the Coulomb interaction in the limit $k_BT \to 0$. The abrupt jump from 0 to 1/4 characterizes a boundary QPT between a non-magnetic and magnetic phase. See Refs.[105] and[55] for more information about boundary QPT.

In the weak coupling regime, the QPT was previously studied in Refs.[54,90] and .[44] To our knowledge, it was only previously associated to the emergence of a BIC in Ref.[44] These works studied the two-impurity Kondo and Anderson Hamiltonian in their ordinary basis. Because of that, the QPT was associated with the ferromagnetic and antiferromagnetic interaction between both impurities that can be direct or intermediate by the conduction electrons. The last one is known as Ruderman-Kittel-Kasuya-Yosida (RKKY) interaction and it is associated to quantum impurities problems far apart from each other. Whenever both impurities are attached at the same spot, as shown in Fig. 14, the RKKY interaction tends to be ferromagnetic. This conclusion is always valid for the two-impurity Kondo Hamiltonian, which that always displays particle-hole symmetry. In the two-impurity Anderson model, that symmetry is achieved only for $\mathcal{U} \neq -2\varepsilon_d$. Outside this condition, the particle-hole symmetry is absent and the RKKY interaction can induce a ferro or antiferromagnetic coupling between the orbitals according the amplitude of the particle-hole asymmetry. This mechanism was discussed shown in Ref.[90]

In the bonding and antibonding basis, the boundary QPT is driven by the competition between a spin triplet and isospin singlet state defined in Eqs. 4.12 and 4.13. The isospin singlet is predominant whenever the antibonding orbital is empty or doubly occupied. As the local moment in the antibonding orbital is zero, the spin-spin interaction is inhibited. The non-magnetic phase is predominant until $\mathcal{U} < \mathcal{U}_c$, where $\mathcal{U}_c$ is the critical amplitude of the Coulomb interaction. For $\mathcal{U} > \mathcal{U}_c$, the antibonding orbital became

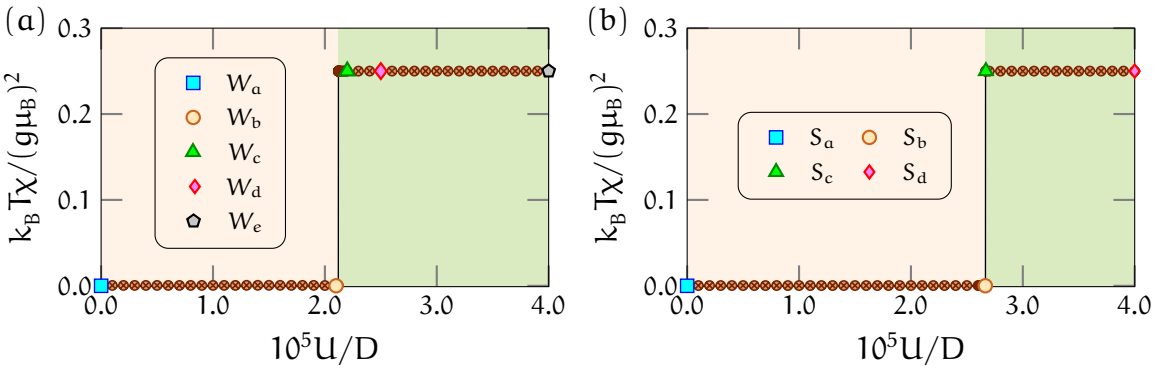

Figure 19 – Magnetic susceptibility as a function of the Coulomb interaction ($\mathcal{U}$) for $k_BT \to 0$ in the (a) weak and (b) strong coupling regime.
Source: By the author.

simply occupied and the opposite behavior is observed. The isospin-isospin interaction is suppressed and the ferromagnetic interaction between the bonding and antibonding orbitals favor the formation of a spin triplet state. The magnetic phase survives even after the bonding orbital is strongly coupled to the continuum due to the presence of a residual spin-1/2.

In the weak coupling regime, the quantum phase transition is associated with instability of the valence fluctuations fixed point. According to the amplitude of $\Delta_1 = -\varepsilon_d$ and $\Delta_2 = \varepsilon_d + \mathcal{U}$, the RG flow can crossover to Frozen impurity orbitals fixed point if the double occupied configuration is energetically favorable ($\Delta_2 < 0$). In addition, it can also flow into the frozen-impurity antibonding-orbital fixed point if the bonding orbital is simple occupied and the antibonding orbital be double occupied. In contrast, if the singly occupied configuration becomes energetically favorable, the system flow through the local-moment and spin-triplet fixed points until it reaches the stable local-moment antibonding-orbital fixed point. The last crossover is assisted by the Kondo effect, which cancels out the magnetic moment of the bonding orbital. Therefore, the residual magnetization is given by the singly occupied configuration of the antibonding orbital.

In the strong coupling regime, the instability of the system is defined by valence-fluctuation antibonding-orbital fixed point because the bonding orbital is diluted in the continuum for $k_BT \ll \Gamma$. For $\mathcal{U} < \mathcal{U}_c$, the system flows to the frozen impurity antibonding orbital fixed-point because the double occupied configuration of the antibonding orbital has the lowest energy. This configuration characterizes the non-magnetic phase. In the opposite case, for $\mathcal{U} < \mathcal{U}_c$, the TIAM Hamiltonian flows to the local-moment antibonding-orbital fixed point with residual magnetization defined by the antibonding orbital with spin-1/2.

The residual magnetization present in the local-moment antibonding orbital fixed point, is a direct consequence of the formation of an unexpected bound spin state in the continuum (spin-BIC). In the same way that the magnetic moment of the bonding

orbital is strongly coupled to the continuum via anti-ferromagnetic interaction, the indirect connection between the antibonding orbital and the continuum is ferromagnetic. Decreasing the temperature, the ferromagnetic coupling goes to zero. This results in a spin state that is decoupled from bonding orbital and the continuum.

The ferromagnetic coupling between the antibonding orbital and the continuum is confirmed via RG analyses of the local-moment antibonding orbital fixed point. Panel (a) and (b) in Fig. 20 shows the second low-lying state of the Sectors $Q = 1$ and $S = 1$ (blue squares) and $Q = 1$ and $S = 0$ (brown circles) for the cases W_e and S_d. As the cases W_c, W_d and S_c display the same behavior, we do not show them here.

In this fixed point, the antibonding orbital can be included into the system perturbatively. As only the bonding orbital is connected to the continuum, for $\Gamma \to \infty$, it is diluted into the continuum. For even N, the ground state in this fixed point is a half-filled Fermi sea with an odd number of electrons plus the antibonding orbital simply occupied. As in the magnetic phase the antibonding orbital only couples via spin-spin interaction to the continuum, the states in the sectors $Q = 1$ and $S = 1$ and $Q = 1$ and $S = 0$ are tensor products of the antibonding orbital and the continuum. Perturbatively including the ferromagnetic interaction, the energies of these states are given by

$$\mathrm{E}_{\mathrm{Tiplet}} = \eta^* - \frac{3}{2}\mathcal{J}(N) \tag{4.26}$$

and

$$\mathrm{E}_{\mathrm{Singlet}} = \eta^* + \frac{1}{2}\mathcal{J}(N), \tag{4.27}$$

with

$$\mathcal{J}(N) = \frac{-2D}{(N - N_K)\log\Lambda}. \tag{4.28}$$

In this equation η^* is a fixed point eigenvalue, D is the half-band width of the conduction band, Λ is the logarithmic discretization parameter, N is the iteration number and N_K is the iteration number that mimics the Kondo temperature of the system. The latter one can be obtained fitting the two states displayed in Panel (a) and (b) of Fig. 20. The fitting was performed using $\eta^* = 0.8907$ and N_K equal to 55 and -965 in the panels (a) and (b), respectively. The good agreement between the NRG data and the pertubative approach is a consequence of the ferromagnetic interaction that vanishes as N grows. This is the main mechanism that originates the spin-BIC in the two-impurity Anderson Hamiltonian.

As the antibonding orbital is weakly affected by the cross-orbital Hamiltonian $\mathcal{H}_{ab}$ in the strong coupling regime, $\mathcal{U}_c$ is easily calculated comparing the energy of the simple and doubly occupied configuration of the antibonding orbital. Taking into account only $\mathcal{H}_a$, the simple occupied configuration has energy $\varepsilon_d + \mathcal{U}/4$ and the double one $2\varepsilon_d + \mathcal{U}$.

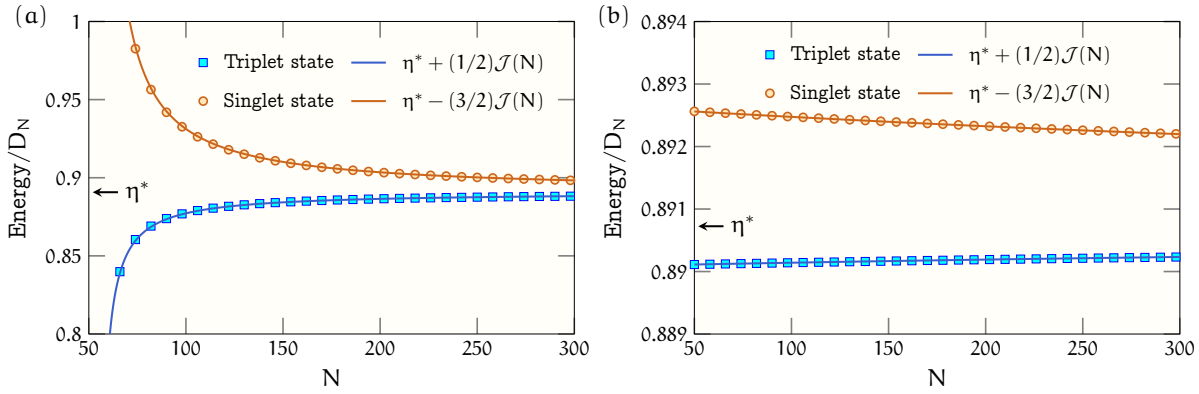

Figure 20 – Low-lying energy levels of $\mathcal{H}_N$ as a function of even N for the cases (a) W_e and (b) S_d. In both panels, the blue squares and brown circles are the second excited state of the Sector $Q = 1$ and $S = 1$ and of the Sector $Q = 1$ and $S = 0$, respectively. The solid curves were obtained with the fitting function defined on Eqs. 4.26 and 4.27.
Source: By the author.

Equating both energies,

$$\mathcal{U}_c = -\frac{4}{3}\varepsilon_d. \tag{4.29}$$

For the parameters used in the panel (b) of Fig. 19, $\mathcal{U}_c \approx 2.6667 \times 10^{-5} D$.

4.4.3.2 Magnetic susceptibility in the weak coupling regime

Fig. 21 displays the magnetic susceptibility as a function of the temperature for five representatives cases specified in the Table 3. In the weak coupling regime, the magnetic susceptibility can be explained in the approximation $\Gamma \to 0$ for $T \gg T_K$. In this framework, the magnetic susceptibility is given by

$$\frac{k_B T \chi}{(g\mu_B)^2} = 2 \times \left(\frac{1/2}{2 + e^{\varepsilon_d / k_B T} + e^{-(\varepsilon_d + \mathcal{U})/k_B T}} \right), \tag{4.30}$$

where $-\varepsilon_d$ and $\varepsilon_d + \mathcal{U}$ are the energies for creation of a hole and a particle in each orbital, respectively. Both energies are defined from the simple occupied configuration. The factor 2 in front of the equation reflects the identity of both orbitals and the parameter 1/2 is the mean value of the spin operator S_z^2 in each orbital.

In the high-temperature regime, the magnetic susceptibility is invariant in the cases W_a-W_e because the thermal excitation are much higher than the other characteristic energies. Therefore, the four orbital configurations contribute to magnetic susceptibility, resulting in an amplitude 1/4. This behavior is characteristic of the free orbital fixed points.

In the run W_a, the magnetic susceptibility as a function of temperature is given by

$$\frac{k_B T \chi}{(g\mu_B)^2} = 2 \times \left(\frac{1/2}{2 + e^{\varepsilon_d / k_B T} + e^{-\varepsilon_d / k_B T}} \right). \tag{4.31}$$

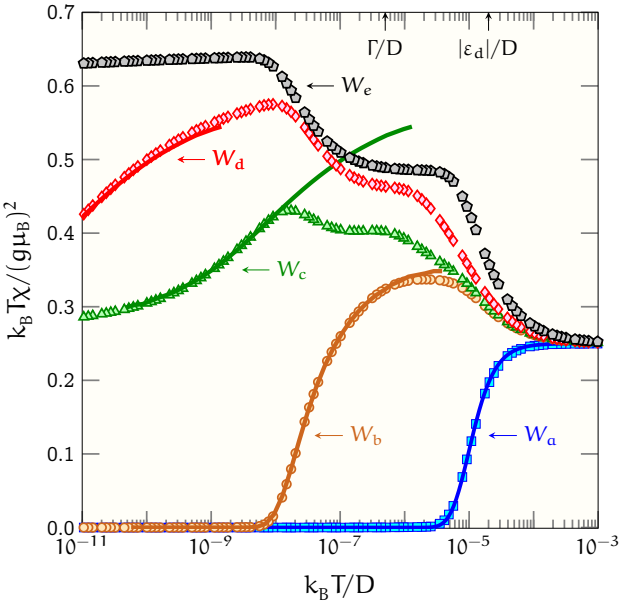

Figure 21 – Magnetic susceptibility as a function of the temperature in the weak coupling regime. The curves display the cases W_a-W_e. The solid blue and orange curves superposed to W_a and W_b were obtained via Eqs. 4.31 and 4.32, respectively. The green and red solid curves, superposed to W_c and W_d, are the universal magnetic susceptibility of the over-screened Kondo effect with spin-1 obtained via Bethe Anzats. The numerical data is specified in the Appendix A.
Source: By the author.

This equation describes the blue solid line superposed to the blue square in Fig. 21. For $k_BT > \varepsilon_d$, the ratio $\varepsilon_d/k_BT \to 0$ and the exponential in the denominator of Eq. 4.31 are close to 1. In the opposite limit, the excitation processes higher than ε_d are energetically suppressed. Specially, in the non-interacting regime the creation and annihilation of a particle and a hole into the orbitals are simultaneously inhibited. Therefore, as the doubly occupied configuration has the lowest energy, the magnetic susceptibility drops to zero. The variation from 1/4 to 0 characterizes the crossover between the free orbitals to frozen-impurity orbitals fixed points.

Run W_b shows the first effects of Coulomb interaction in the orbitals. As the temperature decreases, the empty configurations of both orbitals are frozen out. This process enhances the magnetic susceptibility from 1/4 to 1/3. This variation characterizes the crossover between the free-orbital and valence-fluctuation fixed points. Mathematically, this enhancement occurs because $\varepsilon_d/k_BT \to \infty$ and, consequently, $e^{\varepsilon_d/k_BT} \to 0$ in Eq. 4.30.

Eq. 4.30 fails to describe case W_b for $k_bT < 10^{-6}D$. The disagreement between them is a consequence of the partial emergence of a Kondo effect. In the valence fluctuation regime, the single and doubly occupied configurations are almost degenerate. As the temperature decreases, the energy separation between them is resolved and the lowest energy configuration becomes predominant. In W_b, two distinct behaviors are observed in

each orbital. The bonding orbital becomes singly occupied, due to the coupling with the continuum, while the antibonding orbital is still double occupied. Due to the formation of a local moment in the bonding orbital, a partial Kondo effect emerges. Taking into account such scenario, the NRG data has been be fitted with

$$\frac{k_B T\chi}{(g\mu_B)^2} = \text{const} \times \left(\frac{1/2}{2+e^{-(\varepsilon_d+\mathcal{U})/k_BT}}\right) \times \left(\frac{k_B T\chi_{uni}(T/T_K)}{(g\mu_B)^2}\right), \tag{4.32}$$

where $\chi_{uni}(T/T_K)$ is the universal magnetic susceptibility for the under-screened spin-1 Kondo effect. The numerical data for χ_{uni} is reproduced in Appendix A. The parameter used in this fitting are $k_BT_K = 7\times10^{-9}D$, $\varepsilon_d+\mathcal{U} = 3.1\times10^{-8}D$ and const $= 10.4$. The superposition of these two effects characterizes the crossover from, the valence-fluctuation to frozen-impurity antibonding orbital fixed points.

In run W_c, the initial growth of the magnetic susceptibility at high temperature is a consequence of the suppression of the empty configuration of both orbitals. The plateau with amplitude 0.42 results from the combination of both orbitals in the following configurations: i) a triplet spin state; ii) a single isospin state and; iii) a doublet state, defined by the bonding orbital double occupied and the single occupied antibonding orbital. Finally, as the temperature decreases, the Kondo effect emerges to screen half of the local moment of the triplet state formed by the antiferromagnetic interaction between them. The Kondo effect takes the magnetic susceptibility to 1/4, which is the signature of a spin-BIC.

Runs W_d and W_e are similar. Because of that, they are explained together. The initial increases of the magnetic susceptibility is a direct consequence of the Coulomb interaction. As the temperature decreases, the empty and doubly occupied configuration are energetically penalized, simultaneously. For these set of parameters, both configurations have approximately the same energy. Thus, the magnetic susceptibility increases from 1/4 to 1/2, which characterizes a crossover from the free orbital to the local-moment fixed points. As the temperature decreases, the ferromagnetic interaction described by the first term of the right-hand side of Eq. 4.6 locks the orbitals in a triplet state. This behavior increases the magnetic susceptibility from 1/2 to approximately 2/3. The amplitude is not exactly 2/3 (characteristic of a spin triplet) because the Kondo effects emerges before the magnetic susceptibility reaches its maximum. As a result of the emergence of the Kondo effect, the system crosses over from the spin-triplet to the local-moment antibonding orbital fixed point, in which the magnetic susceptibility is equal to 1/4. The solid curve in the W_d case is the universal magnetic susceptibility for the under-screened spin-1 Kondo effect.

4.4.3.3 Magnetic susceptibility in the strong coupling regime

In the strong coupling regime, the bonding orbital is hybridized with the continuum for $k_BT < \Gamma$, which takes the magnetic susceptibility from 1/4 to 1/8, as shown in Fig. 22. This variation describes the crossover from the free-orbital to the free antibonding-orbital fixed point. Therefore, at low temperatures ($k_BT < \Gamma$), the magnetic properties of the system only receive contribution from the antibonding orbital.

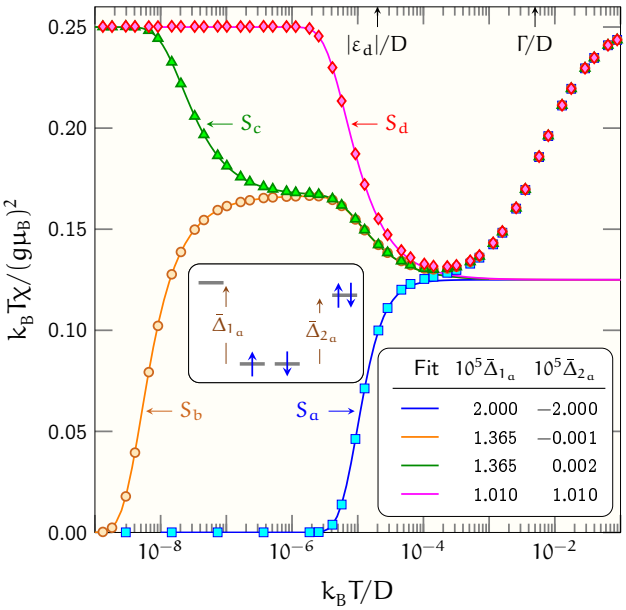

Figure 22 – Magnetic susceptibility as a function of the temperature in the strong coupling regime for the representative cases S_a-S_d. The solid lines were obtained by Eq. 4.33 for the set of parameters indicated in the right inset. The central inset sketches the four configurations of the antibonding orbital.
Source: By the author.

The central inset in Fig. 22 sketches the four configurations of the antibonding orbital and its respective excitation energies $\bar{\Delta}_{1_a}$ and $\bar{\Delta}_{2_a}$. Taking into account these four degrees of freedom, the runs S_a-S_d can be precisely described by the simple equation

$$\frac{k_BT\chi}{(g\mu_B)^2} = \left(\frac{1/2}{2 + e^{\bar{\Delta}_{1_a}/k_BT} + e^{\bar{\Delta}_{2_a}/k_BT}}\right), \tag{4.33}$$

which is the magnetic susceptibility for $\Gamma \to 0$. As shown by the solid curves in Fig. 22, Eq. 4.33 accurately reproduces the NRG data for the fit parameters in the right inset. These parameters can also be estimated from analysis of $\mathcal{H}_b$. Therefore, $\bar{\Delta}_{1_a} \approx \varepsilon_d + \mathcal{U}/4$ and $\bar{\Delta}_{2_a} \approx \varepsilon_d + 3\mathcal{U}/4$.

Run S_a shows the magnetic susceptibility in the non-interacting case. The abrupt drop from 1/8 to 0 is associated to the simultaneous inhibition of the thermal excitation processes with energy $\bar{\Delta}_{1_a}$ and $\bar{\Delta}_{2_a}$. The drop characterizes the crossover from the free antibonding-orbital to the frozen-impurity antibonding orbital fixed point.

The valence-fluctuation regime is observed in runs S_b and S_c for k_BT around 10^{-6} in Fig. 22. For this range of temperature, only the simple and double occupied configurations contribute to the magnetic susceptibility because they are almost degenerate. This unstable configuration is resolved as the temperature decreases. Specifically, if the lowest energy configuration of the antibonding orbital is given by the doubly occupied configuration (run S_b), the mangnetic susceptibility drops to zero. However, if it is simply occupied (run S_c), a magnetic phase emerges in the system, with the magnetic susceptibility 1/4.

Run S_d shows the case in which the empty and doubly occupied configuration are inhibited simultaneously. Therefore, the system flows from free antibonding orbital to the local-moment antibonding-orbital fixed point, where the residual magnetization is due to the spin-BIC.

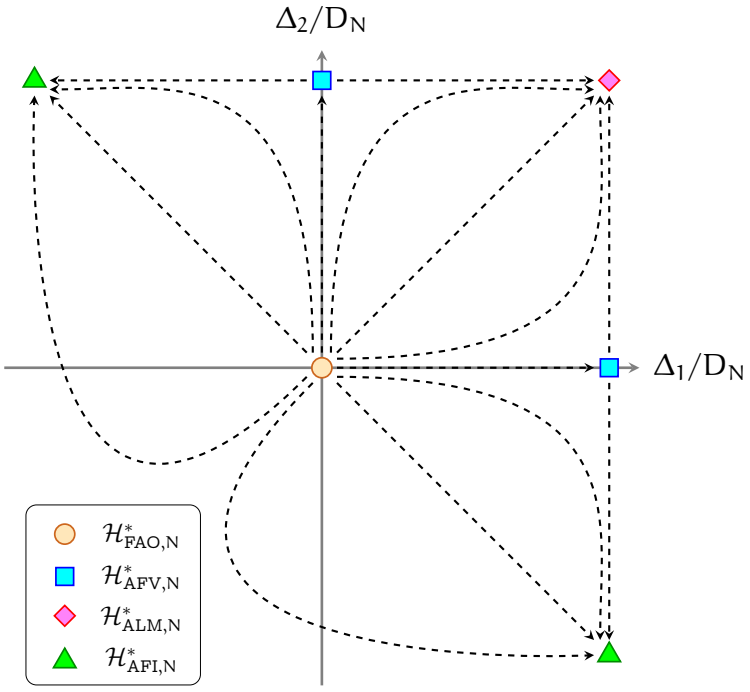

Figure 23 – Renormalization flow diagram for $\Gamma = \infty$ and $\Delta_1 = -\varepsilon_d$ and $\Delta_2 = \varepsilon_d + \mathcal{U}$. The inset displays the fixed point Hamiltonian defined in Table 2.
Source: By the author.

.

Finally, all physical properties of the strong coupling regime for $k_BT \ll \Gamma$ can be summarized in Fig. 23. As previously discussed, in this limit the bonding orbital is diluted in the continuum, i.e., the system flows to the free antibonding orbital fixed point. As this is an unstable fixed point, depending on whether $\Delta_1 = -\varepsilon_d$ or $\Delta_2 = \varepsilon_d + \mathcal{U}$ are renormalized, the truncated Hamiltonian can flow to the following fixed points: i) Frozen impurity antibonding orbital (green triangles); ii) Local-moment antibonding orbital (red diamond) and; iii) Valence-fluctuation antibonding orbital (blue squares). The non-magnetic and magnetic phase are described by the first two stable fixed points, respectively. Finally, the

latter describes the instability of the system induced by the antibonding-orbital degeneracy.

4.4.4 Hamiltonian asymmetry

The parity symmetry can be broken by three distinct mechanisms: i) detuning the energy level of the dots via gate potential; ii) changing the hybridization amplitude between each dot and the wire; and iii) by asymmetry in the intra-dot Coulomb interaction. On the bonding and antibonding basis, each source of asymmetry modifies the Hamiltonians in Eqs. 4.4-4.6 and introduces new terms that directly couple the antibonding orbital with the continuum.

To contemplate two non-identical quantum dots, the second term of the right-hand-side of Eq. 4.1 must be generalized by $\varepsilon_d \to \varepsilon_{d_j}$, with $j = 1, 2$. Following the standard bonding and antibonding transformation, the energy levels of each orbital in Eqs. 4.4 and 4.5 are generalized by $\varepsilon_d = (\varepsilon_{d_1} + \varepsilon_{d_2})/2$. In addition, a direct coupling between the orbitals is obtained via the Hamiltonian mapping. Mathematically,

$$\mathcal{H}_{\text{asy-orbital}} = \frac{1}{2}(\varepsilon_{d_1} - \varepsilon_{d_2})(d_b^\dagger d_a + d_a^\dagger d_b), \tag{4.34}$$

where the coupling amplitude between the orbitals is given by the energy difference of the quantum dots energy level. Therefore, for $\varepsilon_{d_1} = \varepsilon_{d_2}$, the direct coupling goes to zero and the energy levels of each orbital is retrieved.

The coupling asymmetry is induced by the generalization of the last term of the right-hand-side of Eq. 4.1. If the two quantum dots hybridize with the edge of the wire with different amplitudes, $\mathcal{V}$ must be substituted by $\mathcal{V} \to \mathcal{V}_1$ and $\mathcal{V}_2$. In the bonding and antibonding representation, the hybridization amplitude in Eq. 4.4 is redefined by $\mathcal{V} \to (\mathcal{V}_1 + \mathcal{V}_2)/\sqrt{2}$ and an extra coupling between the antibonding orbital and the continuum have to be included into the total Hamiltonian. This new term is expressed by

$$\mathcal{H}_{\text{asy-coupling}} = \frac{1}{\sqrt{2N}}(\mathcal{V}_1 - \mathcal{V}_2)\sum_k (c_k^\dagger d_a + \text{H.c.}), \tag{4.35}$$

where the coupling amplitude is defined by the difference between the coupling of each dot to the wire. In the non-interacting regime, the definition of the bonding and antibonding orbitals can be generalized in order to cancel the coupling in Eq. 4.35. The general definition of the bonding and antibonding orbital is given by

$$d_1 \equiv (\sin\theta d_b + \cos\theta d_a) \tag{4.36}$$

and

$$d_2 \equiv (\cos\theta d_b - \sin\theta d_a), \tag{4.37}$$

where $\tan\theta = \mathcal{V}_1/\mathcal{V}_2$. Based on this definition, the antibonding orbital will always be decoupled from the continuum. The previous transformation can be also applied in the

interacting regime. Here, however, it fails, because with $\theta \neq \pi/4$ Eqs. 4.36 and 4.37 add a term to the right-hand side of the Eq. 4.6 that effectively couples d_a to the conduction band.

Finally, intra-dot Coulomb interaction asymmetry generalizes the third term of the right-hand-side of Eq. 4.1, substituting $\mathcal{U}_j$, with $j = 1, 2$. For this generalization modifies the three components of the Hamiltonian in the bonding and antibonding representation, i.e., $\mathcal{U} = (\mathcal{U}_1 + \mathcal{U}_2)/2$, and results in the new Hamiltonian

$$\begin{aligned}\mathcal{H}_{\text{asy-Coulomb}} = &\frac{1}{4}(\mathcal{U}_1 - \mathcal{U}_2)(d^\dagger_{a\uparrow}d_{b\uparrow} + d^\dagger_{b\uparrow}d_{a\uparrow})(d^\dagger_{b\downarrow}d_{b\downarrow} + d^\dagger_{a\downarrow}d_{a\downarrow}) \\ &+ \frac{1}{4}(\mathcal{U}_1 - \mathcal{U}_2)(d^\dagger_{a\downarrow}d_{b\downarrow} + d^\dagger_{b\downarrow}d_{a\downarrow})(d^\dagger_{b\uparrow}d_{b\uparrow} + d^\dagger_{a\uparrow}d_{a\uparrow}),\end{aligned} \tag{4.38}$$

modulated by the energy between the intra-dot interaction. The new Hamiltonian directly connects both orbitals whenever one of them is simply occupied.

The previous three sources of asymmetry couples the antibonding orbital to the continuum. In other words, they mix the BIC and spin-BIC with the continuum. For the BIC, these three asymmetries act in the same way as the Coulomb interaction does for the symmetric case. As the asymmetry increases, it gradually strengthens the coupling between the antibonding orbital and the continuum. This behavior is verified by calculations of the antibonding orbital spectral density. The same behavior is observed for the spin-BIC. Specifically, it can be observed by analyzing the threshold behavior of the antibonding orbital spectral density. As the asymmetry amplitude grows, the threshold behavior is washed out, due to the mixing between the subspace with even and odd parity symmetry. This indicates that the ground state does not have anymore an isolated contribution from the antibonding orbital.

From experimental point of view, two of the three sources of asymmetries can be avoided by fine tuning the experimental parameters. The energy level of the quantum dot orbitals can be fine tuned by application of gate potential. In the same way, the hybridization asymmetry can be controlled by quantum point contacts or electrostatic gates. The asymmetry induced by the intra-dot Coulomb interaction is the most challenge variable to be experimentally controlled. To our knowledge, there is no mechanism to tune this physical parameter, since it is related to the size and geometry of the dots. To achieve the ideal limit, where both have the same intra-dot Coulomb interaction, the two quantum dots must be identical.

5 NON-LINEAR TRANSPORT FOR CHARGE-DEGENERATE TWO CHANNEL KONDO MODEL

In this chapter, we theoretically investigate the non-equilibrium transport properties of the charge-degenerate two channel Kondo (CD-2CK) model. This project was motivated by the recent experiment by Z. Iftikhar *at. al.*[1] The experimental setup emulates a single electron transistor composed by a huge metallic island. In the low-energy regime, this SET-like device reproduces Kondo physics, because two charging states emulate a pseudospin-1/2 and the charge fluctuations in the island mimic a spin-flip mechanism. The system is driven out of equilibrium by the sudden application of a bias voltage between the leads. Via time-dependent Density Matrix Renormalization Group (tDMRG), we follow the time evolution for times long enough to reproduce the transient regime, although insufficient to reach the steady state.

Even though this project is not yet concluded, important partial results have been obtained: (i) universal behavior of the differential conductance as a function of the bias voltage; (ii) crossover between a Fermi liquid and non-Fermi liquid phase; and (iii) time-dependent differential conductance characteristics explained by the energy-time uncertainty principle, in the transient regime.

We organize this chapter as follows. In Sec. 5.1, we discuss the general aspects of experiment by Z. Iftikhar *at. al.*[1] and the main mechanisms that induce the charge-degenerate two channel Kondo effect. The Hamiltonian used to describe the low-energy physics of the experiment is presented in Sec. 5.2. In that section we also discuss the different characteristic energies of the system and the quantum criticality of the model. Thereafter, we project the CD-2CK Hamiltonian on the real space representation and define the time-dependent calculation of the current, and of the differential conductance, in Sec. 5.3.

In Secs. 5.4 and 5.5, we present the quench protocol adopted in this project and discuss the interpretation of the transient regime on the basis of the energy-time uncertainty principle. In the latter section, we also compare the maximum time reached in the time-dependent experimental measurement with our tDMRG results. Finally, in Sec. 5.6, we show the time-dependent differential conductance as a function of the bias voltage in the symmetric and asymmetric regimes. The latter is defined by the charge-energy asymmetry of the metallic island, which is equivalent to the Zeeman splitting on the Kondo basis.

5.1 Experiment

In Ref.,[1] the authors investigate the equilibrium transport properties of a hybrid metal-semiconductor single-electron transistor. The experimental device is composed by

a metallic island, connected to three electrodes through quantum point contacts (QPC). Two electrodes are strongly connected to the island, acting as a source and drain. The third one is weakly connected and it is used to probe the *in situ* conductance of the other two QPCs. The charging energy on the island is controlled via a lateral gate potential. In addition, a perpendicular magnetic field spin polarizes the system and drives it into an integer quantum Hall regime. Due to the size of the island, there is no coherent transport between the spin-polarized edge channels in the opposite side of the island.

Fig. 24 sketches the experimental device implemented by Z. Iftikhar *at. al.*[1] The two golden semi-ellipses describe the leads, while the semi-circle in the middle depicts part of the huge metallic island. The red solid arrows are spin-polarized edge channels induced by the perpendicular magnetic field.

At low energy, i.e. k_BT and $eV \ll E_c$ (E_c is the charging energy on the island), the transport properties of the experimental device are governed by two charge states $|N+1\rangle$ and $|N\rangle$. As discussed in Sec. 2.3, the Coulomb blockade allows electron flow through the island only if the temperature or the bias voltage is larger than the energy difference between the two charge states or, at zero temperature and bias, when these states are degenerate. In the latter, the electron tunneling changes the occupation of the island without energy cost. To inhibit this process, the conduction channels screen the charge degenerate states of the island. If both channels compete on equal foot to screen the charge states, partial screening is achieved. However, if coupling are different, the conduction channel with larger coupling amplitude totally screens the charge states. This phenomenon is known as the charge-degenerate two channel Kondo effect and takes place at temperature lower than T_{2CK}.

The partial screening generates an entangled phase between the leads, which enhances the electronic flow through the island. This phase is known as the two channel Kondo phase. If one of the channels fully screens the charge states, the current flow is blocked due to the formation of a singlet state between the charge degrees of freedom of the island and the conduction channel with larger coupling amplitude. This behavior is characteristic of the single-channel Kondo phase. The current flow is also blocked if the charging energy separability is high enough to destroy the Kondo effect.

The two channel Kondo physics is observed in a huge spinless metallic island because the charge states define a pseudospin-1/2 and the charge fluctuation in the island emulates a spin-flip mechanism. The energy difference between the two charge states is fully equivalent to the Zeeman splitting of a magnetic Kondo impurity. The explicit mapping between the real system and the Kondo basis was done in Sec. 2.5.

In Ref.,[1] Z. Iftikhar *at. al.* verified that the charge degrees of freedom of the island reproduces the two channel Kondo physics. Specifically, they were able to: (i) reproduce the universal behavior of the zero-bias conductance as a function of the temperature; (ii)

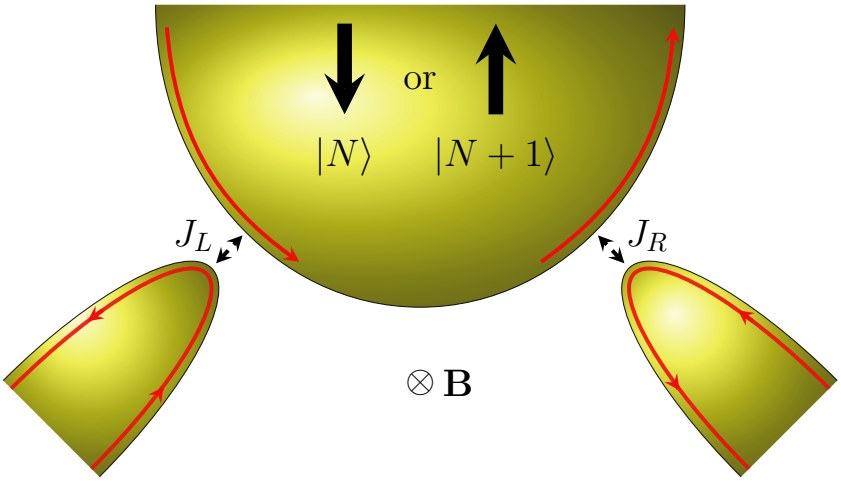

Figure 24 – Sketch of the experimental setup in Ref.[1] The two golden semi-ellipses describe the leads, while the semi-circle in the middle depicts part of the huge metallic island. To eliminate the spin degrees of freedom, a strong perpendicular magnetic field ($\mathbf{B}$) takes the system into an integer quantum Hall regime. Here, the red solid arrows represent its edge channels. At low energy, only the $|N+1\rangle$ and $|N\rangle$ charge states influence the transport, which states mimics the pseudospin-1/2 represented by the black arrows.
Source: By the author.

verify the quantum criticality of the two channel Kondo effect and the crossover from the two channel to a single-channel Kondo phase. Based on the latter one, they presented a renormalization-group flow diagram that prescribes the crossover between these two phases.

5.2 Charge-degenerate two-channel Kondo model

The electronic properties of the experimental setup sketched in Fig. 24 is given by

$$\mathcal{H}_{\text{Real}} = \sum_{k,\alpha} \varepsilon_k c^\dagger_{k\alpha} c_{k\alpha} + \sum_{p,\alpha} \varepsilon_p c^\dagger_{p\alpha} c_{p\alpha} + \sum_{k\alpha,p} \left(J_{k\alpha,p} c^\dagger_{k\alpha} c_{p\alpha} + \text{H.c.} \right) + \frac{\hat{Q}^2}{2C}. \tag{5.1}$$

where first term describes the left and right spinless leads ($\alpha = L, R$) as non-interacting, half-filled conduction bands with bandwidth $2E_c$ and linear dispersion relation ε_k. The island is defined by two non-interacting, spinless, half-filled conduction bands with bandwidth $2E_c$ and linear dispersion relation ε_p. Coherent transport between them is suppressed, due to the size of the island. The third term couples the α-side of the island with to α-lead. The final term describes the electron-electron interaction in the island, with

$$\hat{Q} = \sum_{p,\alpha} c^\dagger_{p\alpha} c_{p\alpha}, \tag{5.2}$$

and C is the capacitance of the island. The system is driven out of equilibrium by an external bias voltage eV applied to each lead. Specifically,

$$\mathcal{H}_{\text{bias}} = \frac{eV}{2} \left(\sum_k c^\dagger_{kL} c_{kL} - \sum_k c^\dagger_{kR} c_{kR} \right), \tag{5.3}$$

where eV defines the amplitude of the bias voltage.

Following the mapping discussed in Sec. 2.5, the Hamiltonian in Eq. 5.1 becomes

$$\mathcal{H}_{\text{2CK}} = \sum_{k,\alpha,\sigma} \varepsilon_k c^\dagger_{k\alpha\sigma} c_{k\alpha\sigma} + \sum_{k,p,\alpha} \left(J_{k\alpha,p} c^\dagger_{k\alpha\uparrow} c_{p\alpha\downarrow} S^- + \text{H.c.} \right) - V_g S_z, \tag{5.4}$$

which is the anisotropic Kondo Hamiltonian, or the charge-degenerate two channel Kondo (CD-2CK) Hamiltonian, as we prefer to call it. The first term describes two spin-full leads ($\alpha = L, R$) as non-interacting, half-filled conduction bands with bandwidth $2E_c$ and linear dispersion relation ε_k. The second term describes the perpendicular component of the spin-spin interaction between the magnetic moment and the conduction electrons, while the final one defines a Zeeman splitting associated with the magnetic moment. Specifically, V_g emulates the quantity eU in the last term of the right-hand side in Eq. 2.20.

Repeating the mapping in Sec. 2.5 for the Hamiltonian in Eq. 5.3, the external bias becomes

$$\mathcal{H}_{\text{bias}} = \frac{eV}{2} \left(\sum_k c^\dagger_{kL,\uparrow} c_{kL,\uparrow} - \sum_k c^\dagger_{kR,\uparrow} c_{kR,\uparrow} \right). \tag{5.5}$$

In the spin basis, the bias voltage acts as a pseudo-magnetic field that only shifts the energy levels of the leads with spin-up orientation. This term is suddenly introduced in the Hamiltonian at zero time. More details about the quench protocol discussed in Sec. 5.4.

The rules of the mapping used in this section are summarized in Table 6. We reproduce Table 1 in this chapter to help the reader.

Table 6 – Rules of the mapping of the Real system into the Kondo Hamiltonian.

Real basis	Kondo basis
Charging energy (E_c)	Half bandwidth
Hybridization amplitude (J_L and J_R)	Exchange coupling
Gate voltage (V_g)	Magnetic field on the local moment
Bias voltage (eV)	Magnetic field in the spin up electrons
Leads	Spin up electrons
Island	Spin down electrons
Occupation number	Local moment

Source: By the author.

5.2.1 Characteristic energies

Fig. 25 summarizes the characteristic energies of the CD-2CK Hamiltonian. The charging energy E_c is originated by the electron-electron interaction and defines the half-bandwidth in the spin basis. The coupling amplitudes J_L and J_R modulate the coupling between the island and the leads.

T_{2CK} is the two-channel Kondo temperature, estimated as

$$T_{2CK} \approx D(\rho J)\exp(-\pi/4\rho J), \tag{5.6}$$

where ρ is the density of state of the leads and $J = J_L = J_R$. This equation was obtained via perturbation theory by Matveev and is only valid for $J \ll E_c$.[15] This energy scale defines the half-width of the two-channel Kondo peak. The Kondo effect vanishes if the bias voltage or some asymmetry ($\Delta J = J_L - J_R$ or V_g different from zero) induces another characteristic energy larger than $k_b T_{2CK}$.

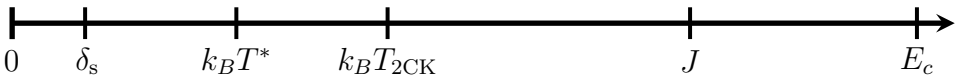

Figure 25 – Characteristic energies of the charge-degenerate two channel Kondo Hamiltonian. From left to right, δ_s is the mean level energy spacing originated by the finite size of the leads and island, T^* is the crossover temperature induced by some asymmetry, T_{2CK} is the two Channel Kondo temperature, $J_{L/R}$ is the coupling energy between the leads and the island, and E_c is the half-bandwidth or charging energy.
Source: By the author.

T^* characterizes the crossover from non-Fermi liquid (two channel Kondo limit) to Fermi liquid fixed point (single Channel Kondo effect or non-Kondo phase). The crossover temperature is defined by

$$T^* = c_1 \left(\Delta J\right)^2 T_{2CK} + c_2 \left(V_g\right)^2 / T_{2CK} \tag{5.7}$$

and is one of the two possible asymmetries in the system.[106] In the equation, $\Delta J = J_L - J_R$, c_1 and c_2 are constants to be determined numerically. This definition is only valid for small values of ΔJ and V_g.

Fig. 26 sketches the phase diagram of the charge-degenerate two-channel Kondo model. The dashed dark-orange line represents the crossover temperature that separates the Fermi liquid (blue region) from the non-Fermi liquid phase (white region). The vertical axis defines the excitation energies induced by temperature and bias voltage. The horizontal axis defines the coupling asymmetry ($\Delta J = J_L - J_R$) and gate potential V_g. For finite temperature and bias voltage, the quantum critical point that defines the non-Fermi liquid phase broadens and allows the two-channel Kondo phase to be accessed even in

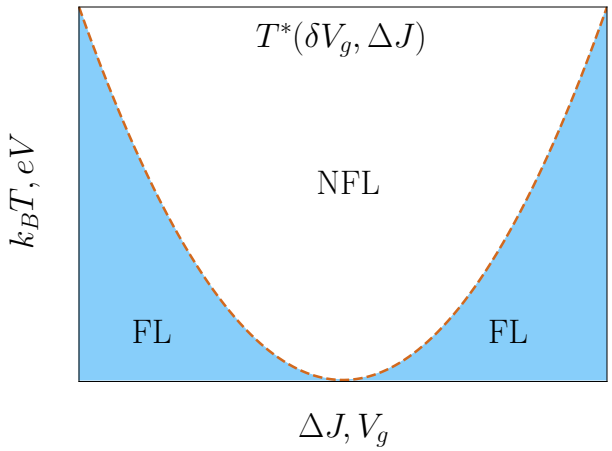

Figure 26 – Sketch of the phase diagram for the charge-denegerate two channel Kondo model. The crossover temperature T^* is defined by Eq. 5.6 and illustrated by the dark orange dashed line. The blue and white region define, respectively, a Fermi liquid and non-Fermi liquid phase.
Source: By the author.

the presence of asymmetry. In Sec. 5.6, we investigate how the system crossover from a non-Fermi liquid to Fermi-liquid phase at finite bias voltage.

The mean level spacing in the leads and island (δ_s) is the lowest energy scale. It must be much lower than all other characteristic energy for the Kondo effect to emerge. In the tight-binding approximation, the mean level energy spacing in the island and leads is approximately given by $\delta_s \approx 2E_c/N$, where N is the number of sites.

In equilibrium, the characteristic energies illustrated in Fig. 25 are accessed as a function of the temperature. Specifically, at finite temperature the particles are excited with energy proportional to k_BT, where k_B is the Boltzmann constant. Varying the temperature, different energy scales are assessed and a crossover is observed when the temperature crosses T_{2CK} or T^*.

At zero temperature, different characteristic energies are accessed when the system is driven out of equilibrium. This can be done in various ways. However, in this thesis we suddenly apply a bias voltage between the leads. As time evolves, different characteristic energies are accesses along the transient regime. The energy resolution along this process is determined by the energy-time uncertainty principle. As the time evolution reaches the steady state, only excitations of the order of eV still relevant. Specifically, the steady state is reached when all observables become time invariant.

5.3 Real-space Hamiltonian and observables

As discussed in Sec. 3.2, the tDMRG can be implemented in the framework of Matrix product states (MPS) and Matrix product operators (MPO). In this representation, the CD-2CK Hamiltonian can be described in the momentum representation, as the one

adopted in the NRG approach, or on a real-space basis. Even though the momentum representation proposed in the context of NRG gives access to excitation process with $\varepsilon \to 0$, it also adds nonphysical oscillations in the time-evolution of the observable that cannot be easily canceled out by integrating over z, as in equilibrium problems. To avoid such nonphysical oscillation, in this project we work in the real-space representation, in which the leads are described by a non-interacting tight-binding chain. The main disadvantage is the emergence of a fictitious energy scale δ_s (mean energy level space). This quantity is inversely proportional to the size of the tight-binding chain. In order to overcome this problem, we choose the coupling constant so that $\delta_s \ll T_{2\mathrm{CK}}$.

On the real space basis, the Hamiltonian CD-2CK Hamiltonian in Eq. 2.20 is rewritten as

$$\begin{aligned}\mathcal{H}_{2\mathrm{CK}} =& -\sum_{i<0,\sigma} t_i \left(c^+_{i-1,\sigma} c_{i,\sigma} + h.c.\right) - \sum_{i>0,\sigma} t_i \left(c^+_{i,\sigma} c_{i+1,\sigma} + h.c.\right) - V_g S^z_0 \\ & - J_L \left(c^+_{-1,\uparrow} c_{-1,\downarrow} S^-_0 + h.c.\right) - J_R \left(c^+_{1,\uparrow} c_{1,\downarrow} S^-_0 + h.c.\right). \end{aligned} \tag{5.8}$$

Specifically, this Hamiltonian is a one dimensional tight-binding chain with $2N+1$ sites, where N is the number of sites in each lead. The left (right) lead is described by the sequence of sites $-N \leq i < 0$ ($0 > i \geq N$), as indicated by the first (second) term in Eq. 5.8. At the center of the chain is a spin-1/2 site with two spin configurations separated by the energy $-V_g$. Both leads are connected via spin-flip scattering with amplitude J_L and J_R. As defined by the fourth and five terms in the Hamiltonian. Finally, the bias voltage Hamiltonian become

$$\mathcal{H}_{\mathrm{bias}} = \frac{eV}{2}\left(\sum_{i<0} c^+_{i,\uparrow} c_{i,\uparrow} - \sum_{i>0} c^+_{i,\uparrow} c_{i,\uparrow}\right), \tag{5.9}$$

where the first (second) term shifts the conduction band with spin-up orientation in the left (right) lead. On the spin basis, this term induces a spin current between the leads.

In a single-electron transistor, the current is defined by the time-dependent variation of the difference between electronic occupation in the left and right leads. For the CD-2CK Hamiltonian, the current induced by Eq. 5.9 is measured by the expectation value of the operator

$$I = -\frac{e}{2}\frac{\partial}{\partial t}\sum_k \left(c^\dagger_{kL\uparrow} c_{kL\uparrow} - c^\dagger_{kR\uparrow} c_{kR\uparrow}\right). \tag{5.10}$$

Calculating the time-derivative and projecting the result in the real-space representation, the current operator becomes

$$I = \frac{e}{2}\frac{i}{\hbar}\left[\left(J_L c^\dagger_{-1\uparrow} c_{-1\downarrow} - J_R c^\dagger_{1\uparrow} c_{1\downarrow}\right) S^- - \left(J_L c^\dagger_{-1\downarrow} c_{-1\uparrow} - J_R c^\dagger_{1\downarrow} c_{1\uparrow}\right) S^+\right]. \tag{5.11}$$

This operator measures the charge variation that goes in and out at each side of the central region. The time-dependent current is calculated by measuring the expectation value of this operator for each time step along the time evolution.

The differential conductance is directly obtained from the calculation of the expectation value of the current operator. By definition,

$$\mathcal{G}(eV) = \frac{\partial I}{\partial eV} \tag{5.12}$$

where I is the current operator defined in the Eq. 5.11. In order to yield accurate numerical derivatives, the conductance is calculated by

$$\mathcal{G}(eV) = \frac{I(eV + \Delta eV) - I(eV)}{\Delta eV} \tag{5.13}$$

with $\Delta eV/E_c = 0.001$. Note that each point of the differential conductance involves two runs of tDMRG.

The expectation values of the current $I(eV)$ is determined by averaging the time-dependent expectation value of the current in a specified interval. In this chapter, the time interval is labeled t_M. The averaging smooths the current oscillations over two current measurements and improves the quality of the numerical derivative.

5.4 Quench protocol

The quantum quench is a non-equilibrium process that time-evolves the ground state of a system under the influence of the initial Hamiltonian plus an external perturbation. In nanostructures, such as a single-electron transistor, the system is driven out of equilibrium by the sudden introduction of an external potential difference across the leads. This perturbation creates an electrical field and, consequently, electronic transport through the nanostructure.

Fig. 27 sketches the quench protocol for the CD-2CK model. For $t < 0$, $\mathcal{H}_{\text{2CK}}$ is in equilibrium and the ground state can be calculated by GS-DMRG. At $t = 0$, a sudden potential is applied between the leads, as illustrated by the upper right scheme in Fig. 27. For $t \geq 0$, tDMRG follows the time evolution of the ground state of the system based on the Hamiltonian $\mathcal{H}_{\text{2CK}} + \mathcal{H}_{\text{bias}}$.

We should emphasize that the quench protocol is a generic procedure and it can be done following any strategy. For example, the CD-2CK model could be prepared as a two biased leads decoupled from the central region and then, to drive the system out of equilibrium, the coupling would be turned on. The latter quench protocol and the one sketched in Fig. 27 may reach the same steady-state at $t \to \infty$. However, the transient regime cases will be different in the two protocols. For the CD-2CK model, the steady state regime can be defined by t much bigger than the inverse of all characteristic energies discussed in Subsec. 5.2.1. Outside this condition, the system is found in the transient regime.

In the protocol where the central region is connected to the leads, the system starts out in the two-channel Kondo phase and the electronic transport induced by the quench

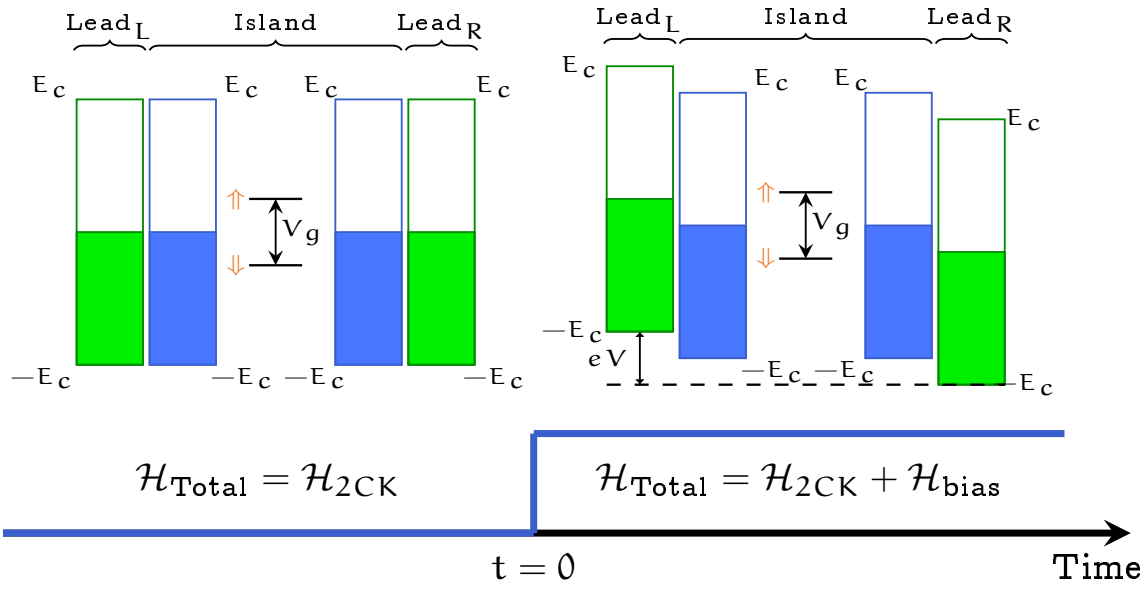

Figure 27 – Sketch of the quench protocol of the charge-degenerate two channel Kondo effect. For $t < 0$, the ground state is described by $\mathcal{H}_{2\text{CK}}$, as represented by the left scheme. For time $t \geq 0$, the time evolution is driven by the perturbed Hamiltonian $\mathcal{H}_{2\text{CK}} + \mathcal{H}_{\text{bias}}$ via tDMRG. The right scheme illustrates the biased leads.
Source: By the author.

is assisted by the Kondo effect. In the second one, as the leads are decoupled from the continuum, the Kondo effect is absent. Therefore, as the coupling is turned on, two effects is observed simultaneously (i) the formation of the Kondo cloud, which takes a times proportional to $1/T_{2\text{CK}}$, plus (ii) electronic transport thought the central region. As the two process are co-dependent, the transient regime is definitely different.

5.5 Transient regime and time measurement resolution

The energy resolution of the time-dependent measurement is given by the uncertainty principle

$$\Delta E \Delta t \geq \frac{1}{2}, \tag{5.14}$$

for $\hbar = 1$. In our theoretical model, Δt defines the time interval of the current measurement and ΔE the energy resolution of the excitation processes assessed in the time interval Δt. As time evolves, the energy resolution of the time-dependent measurement increases in such a way that it is able to capture lower energy excitation processes. Precisely, the energy-time uncertainty principle show us that the energy resolution of the time-dependent measurement is given by $\Delta E \propto 1/\Delta t$. The numerical data shown in Sec. 5.6 ratifies this interpretation.

As an example, let us consider the configuration sketched in the right scheme of

Fig. 27 and, for simplicity, we assume that the leads are equally coupled to the central region. As the system is initially in the Kondo phase, four characteristic energies have an effect on the time-dependent measurement: i) the applied bias voltage (eV); ii) the gate potential V_g; iii) the Kondo ($T_{2\mathrm{CK}}$); and iv) the crossover T^* temperature. Assuming that $eV > V_g > T_{2\mathrm{CK}} > T^*$, the time-dependent measurement gradually solves the effects of each characteristic energy for a specific range of time. If $t < 1/eV$, the physical properties of the system are identical to the ones obtained at zero-bias regime because the time-dependent measurement does not have resolution to resolve the extra energy due to the applied bias and the other characteristic energies. For $1/eV > t > 1/V_g$, the energy resolution of the measurement only captures the effects of the bias voltage. The same explanation can be extended to the other time intervals.

Experimental measurements are also restricted to the energy-time uncertainty principle. The maximum time reached in an experiment is given by the temperature of the system. As the system is immersed in a thermal reservoir with temperature k_BT, as soon as the measure time is long enough to be inversely proportional to $1/k_BT$, the energy uncertainty is resolved and the reservoir includes or takes out energy of the system to keep it in thermal equilibrium. As the conductance measurement in the SET studied by Z. Iftikhar in Ref.[1] was performed at $T = 11.5$ mK and $T = 22$ mK, the maximum times reached for these two temperatures are 33.2 ns and 17.3 ns, respectively. These two maximum times were estimated by Eq. 5.14.

In order to compare the maximum time of our theoretical model with the experiment, we apply the energy-time uncertainty principal for δ_s, that is the smallest energy scale of our system. Specifically,

$$\Delta t \geq 1/2\delta_s \cong E_c/N, \tag{5.15}$$

with $\delta_s \approx N/2E_c$. This approximation is done considering the leads as a non-interacting tight-binding chain with N sites and semi-bandwidth E_c. As in the experiment $E_c \approx k_B \times 290$ mK and $N = 249$ in our theoretical model, the maximum time reached by our model is $\Delta t \geq 1.64$ ns. Therefore, we conclude that the maximum time in our theoretical calculation is between 10 to 20 times smaller than maximum experimental time.

5.6 Numerical results

The non-equilibrium results of this section were obtained by a theoretical setup composed by 498 spin-full sites plus an extra spin-1/2. Each lead is composed by 249 sites in order to satisfy the condition $\delta_s \ll T_{2\mathrm{CK}}$ for all cases investigated in this section. Following the quench protocol sketched in Fig. 27, the results were achieved in two steps: first, the optimum ground state is obtained via GS-DMRG; and, second, ii) the ground state is evolves in time via tDMRG under a finite bias voltage. The optimum ground state was obtained requiting the truncation error to be equal to 10^{-5} and $\left|\langle\mathcal{H}^2\rangle - \langle\mathcal{H}\ \rangle^2\right| \leq 10^{-8}$.

The time evolution was performed in the framework of 4-th Suzuki-Trotter decomposition with time step $\delta t = 0.125$ and truncation error 10^{-4}. The maximum time obtained in our time evolution is approximately $249 \times E_c$. For longer times, the sign of the current is inverted due to the finite boundary conditions, i.e., $t_{\text{mas}} \approx E_c/\delta_s$.

Two cases are discussed in this section: i) the symmetric coupling regime ($J_L = J_R = J$ and $V_g = 0$); and ii) the asymmetric regime for finite gate voltage ($J_L = J_R = J$ and $V_g \neq 0$).

5.6.1 Symmetric coupling regime

In the symmetric-coupling regime, the system is initially prepared in the two channel Kondo phase and it is driven out-of-equilibrium by the sudden introduction of a bias voltage. In this setup, the bias voltage shifts the energy of the Fermi level of the two leads. Consequently, it divides the Kondo peak in two new resonances. The splitting of the Kondo peak generates two different transport regimes in the system. For $eV \ll T_{2\text{CK}}$, the current increases linearly as a function of the bias voltage. For $eV \gg T_{2\text{CK}}$, non-linear contributions arises such as eV^2. In addition, as eV increases, the Kondo effect is gradually destroyed.

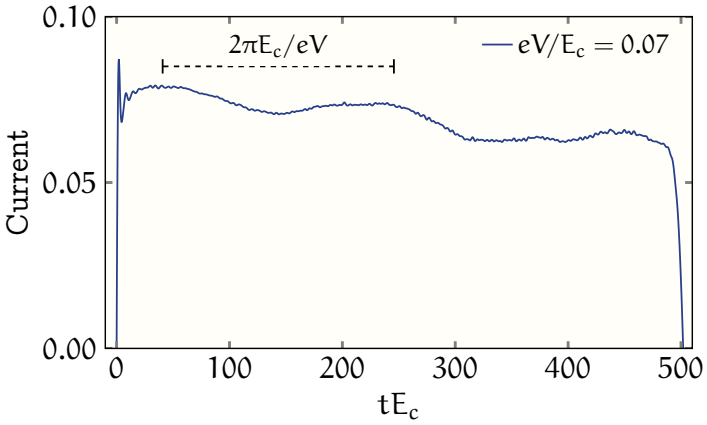

Figure 28 – Current as a function of time in the symmetric coupling regime for $J/E_c = 0.4$, $V_g = 0$ and $eV/E_c = 0.07$. The dashed horizontal line indicates a period of the current oscillation induced by the sudden application of the bias voltage. Source: By the author.

In the symmetric coupling regime, we calculate the differential conductance for $J/E_c = 0.3$, 0.35 and 0.4. In these cases, the 2CK temperature is given by $T_{2\text{CK}}/E_c = 0.009$, 0.025 and 0.061, where the T_{2CK} were calculated as the half-height of the T-matrix computed by NRG. We recall that the expression of the Kondo temperature in Eq. 5.6 fails for large J.

Fig. 28 displays the current as a function of time for finite bias voltage ($eV/E_c = 0.07$) in the symmetric coupling regime ($J/E_c = 0.4$). Right after the quench ($t/E_c \ll 1$),

the current abruptly increases to approximately eV and oscillates with period $2\pi E_c/eV$. As we are investigating the symmetric coupling regime, the time-dependent current must not deviate from the expected amplitude eV, even in the non-linear regime. The dropping of the current around $tE_c \approx 500$ is a consequence of the finite size of the lattice. Specifically, it means that the current flows from the center to the edge of the tight-binding chain and is then reflected back by the finite boundary conditions. When the electron current reaches the site where the current is being measured, the sign of the current is inverted. The inversion time is approximately $1/\delta_s$.

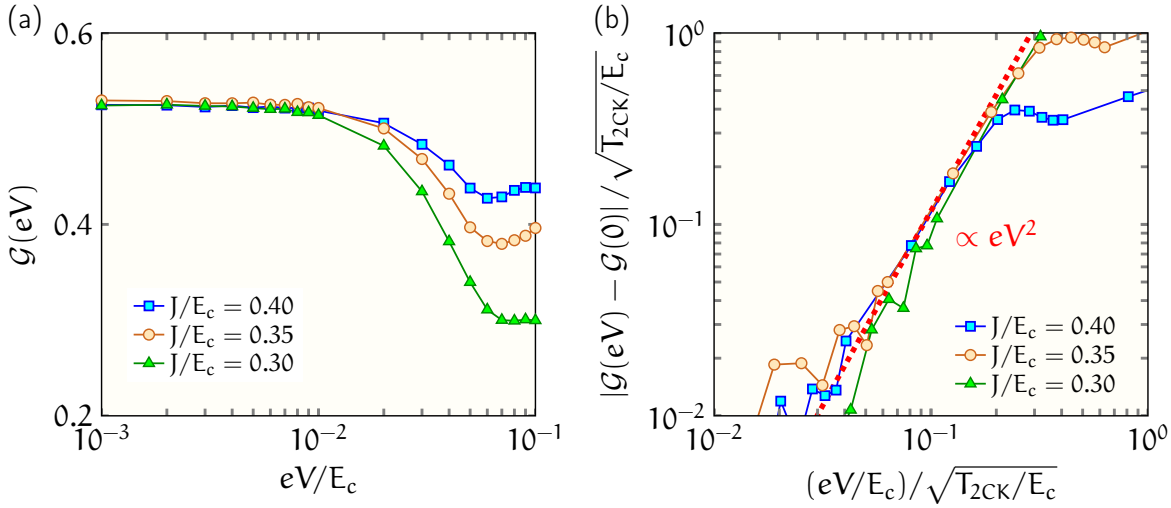

Figure 29 – Panel (a): Conductance as function of the bias voltage for $J/E_c = 0.3$, 0.35 and 0.4. Panel (b): Rescaled conductance as a function of the bias voltage. The dashed red line emphasizes the non-linear behavior of the conductance. In both panels, each data point was calculated by averaging the current in the time interval $20 \leq t/E_c \leq 50$.
Source: By the author.

Panel (a) of Fig. 29 shows the conductance as a function of the bias voltage for $J/E_c = 0.3$, 0.35 and 0.4. In the plot, each point corresponds to the average of the current in the time interval $20 \leq t/E_c \leq 50$. From Eq. 5.14, the lowest energy accessed in the time-dependent measurement is $0.01E_c$, which is lower than ($J/E_c = 0.35$ and 0.4) or approximately equal to ($J/E_c = 0.30$) the Kondo temperature for the three cases displayed in the Panel. For $eV/E_c < 0.01$, the system is found in the linear regime with characteristic conductance amplitude $\mathcal{G}(eV) = 0.5$. In the opposite regime, for $eV/E_c > 0.01$, the conductance is non longer linear. In this regime, the conductance varies with eV^2. The differential conductance behavior does not change if the current is measured for longer times, i.e., $t/E_c > 50$.

Panel (b) of Fig. 29 plots the difference between $\mathcal{G}(eV)$ displayed in the panel (a) and $\mathcal{G}(0)$, that is the conductance for $eV/E_c = 0.001$. Rescaling this quantity by $\sqrt{T_{2CK}/E_c}$, the conductance displays universal behavior as a function of the bias voltage. In addition, we verify that $\mathcal{G}(eV) - \mathcal{G}(0)$ increases with eV^2, which is therefore the first correction to

the linear behavior of the current. This is expected, because the current must be an odd function of eV.

5.6.2 Finite gate voltage regime

Fig. 27 sketches the effective system in the presence of a finite gate voltage (V_g). As discussed in Secs. 5.1 and 5.2, the gate potential V_g splits the charging energy states of the island. In the Kondo basis, this is fully equivalent to the Zeeman splitting. As V_g grows, two effects are expected: i) the Kondo peak broads for $T^* \ll T_{\mathrm{2CK}}$, and vanishes for $V_g \approx T_{2CK}$; and ii) for $T^* \gg T_{\mathrm{2CK}}$, the Kondo effect is destroyed and the electronic transport though the island is suppressed.

Different from Subsec. 5.6.1, the applied bias enhances electronic transport through the island when it has the same amplitude as the gate voltage. When the Fermi levels of both leads resonate with V_g, the electronic transport through the island increases again. This explanation is valid for $T^* \leq T_{\mathrm{2CK}}$.

For finite V_g, the transient regime becomes more complex. In this case, three characteristic energies directly play an important role in time-dependent measurements: i) the gate potential V_g; ii) the crossover temperature T^*; and iii) the two channel Kondo temperature T_{2CK}. For example, Fig. 31 displays the current as a function of time for $J/E_c = 0.4$, $eV/E_c = 0.01$ and $V_g/E_c = 0.02$. In the short time regime, defined by the highlighted blue area describing $t \ll E_c/eV$, the current divided by the bias voltage has amplitude around 0.5, which characterizes the linear regime for $V_g = 0$. This regime is attained because the energy-time uncertainty principle allows us to capture only high-energy excitations. Therefore, the energy resolution of the time-dependent measurement is unable to capture the level splitting induced by V_g. The time-dependent measurement starts to capture effect of the gate potential for $t = E_c/eV$, as displayed by the orange highlighted area defined in the time t_{M_2}. Finally, for $t \gg E_c/eV$, as shown by the green highlighted area, the time is long enough to resolve the energy separation introduced by V_g.

The color plot on Panel (b) in Fig. 31 displays an overview of the energy resolution of the time-dependent measurement of the conductance as a function of time and gate potential for $J/E_c = 0.4$ and $eV/E_c = 0.01$. In this plot, t_M is the average between $t_i < t_M/E_c < t_i + 5$, where t_i is the initial time. In the short time regime, the system is found in the linear regime and, as longer times are reached, lower-energy excitation processes are assessed. The blue dashed line delimits the energy resolution in the time-dependent measurement. Note that only the large values of gate potential are quickly energetically solved by the time-dependent measurement.

Panel (a) in Fig. 31 shows three horizontal cuts in the color plots. As previously explained, for $t_M = 0.2/eV$, the system is found in the 2CK phase. In this short time

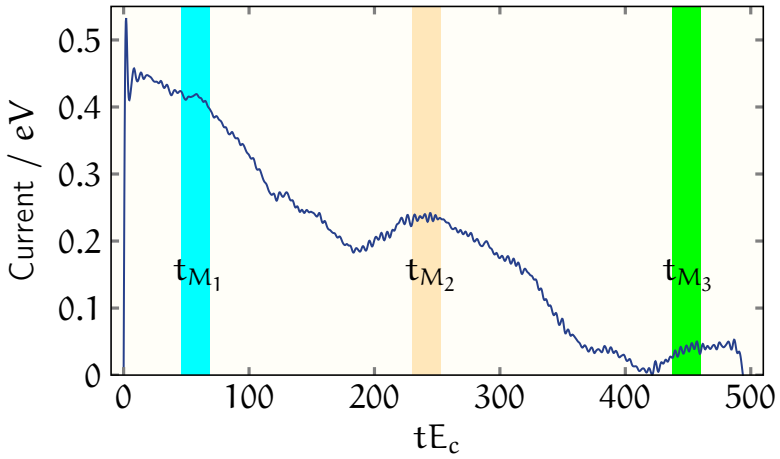

Figure 30 – Current as a function of time for $J/E_c = 0.4$, $eV/E_c = 0.01$ and $V_g/E_c = 0.02$. The three color regions defined by t_{M_1}, t_{M_2} and t_{M_3} emphasizes the limits $t \ll E_c/eV$, $t = E_c/eV$ and $t \gg E_c/eV$, respectively.
Source: By the author.

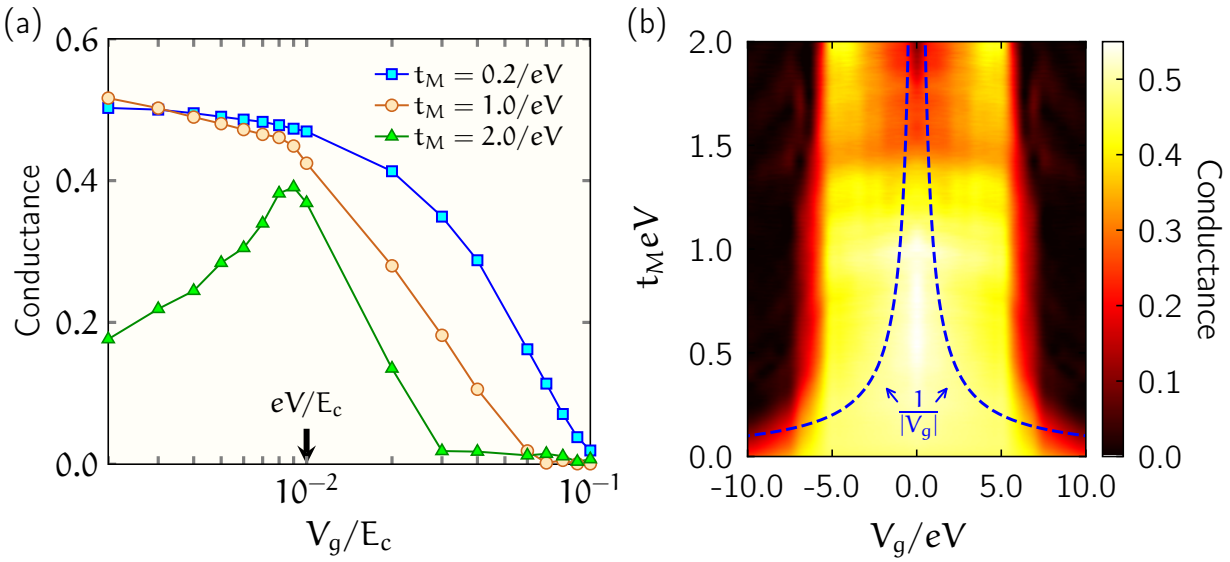

Figure 31 – Panel (a): Conductance as a function of the gate potential V_g for $J/E_c = 0.4$ and $eV/E_c = 0.01$. t_M defines the time range where the current was average. Panel (b): Colorplot of the Conductance as a function of gate potential (V_g) and time t_M. The blue dashed line delimits the energy resolution of the current measurement.
Source: By the author.

regime, the energy resolution only takes into account high-energy excitation processes. In the intermediate regime defined by $t_M = 1.0/eV$, the energy resolution of the time-dependent measurement is only able to detect the effects of V_g for $V_g/eV \geq 1$. Therefore, the conductance keeps constant for $V_g/eV < 1$ while its quickly decreases in the opposite regime. Finally, for $t_M = 2.0/eV$, the time is long enough to energetically resolve all values of V_g. The green curve shows the enhancement of the conductance when the eV and V_g

has the same amplitude.

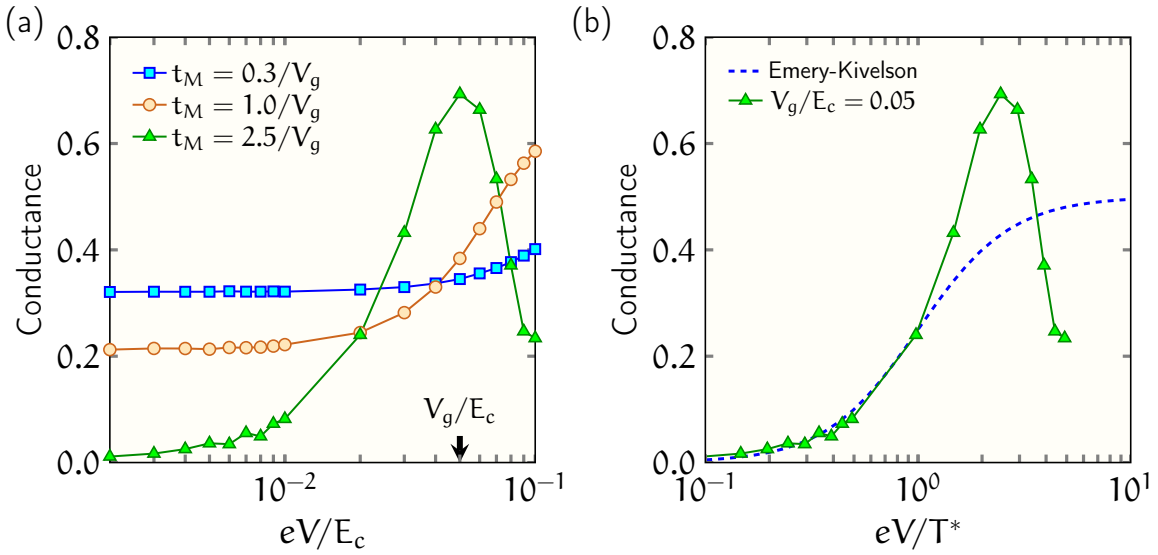

Figure 32 – Panel (a): Conductance as a function of bias voltage for $J/E_c = 0.4$ and $V_g/E_c = 0.05$ for three different time limits. The three curves were obtained by $T_M \ll 1/V_g$, $T_M = 1/V_g$ and $T_M \gg 1/V_g$. Panel (b): Conductance as a function of the bias voltage. The plot compares the green case in Panel (a) with the Emery-Kivelson solution from Ref.[2] The crossover temperature for the green curve is $T^*/E_c = 0.021$.
Source: By the author.

The energy resolution of the time-dependent measurement also influences the conductance as a function of the bias voltage $J/E_c = 0.4$ and $V_g/E_c = 0.05$. As displayed in Panel (a) of Fig. 32, in the short time regime $t_M = 0.3/V_g$ the energy resolution is not small enough to respond to the action of the gate potential and the bias voltage eV. However, as longer times are accessed, the conductance drops to zero at low bias voltage and forms a resonant peak round V_g/E_c. The resonant peak emerges due to the action of the bias voltage that is aligned the Fermi level of both leads. Finally, Panel (b) in Fig. 32 compares the green curve of the Panel (a) with the Emery-Kivelson solution from Ref.[2] Shortly, the Emery-Kivelson solution maps the asymmetric two channel Kondo model upon a non-interacting system for a specific set of parameters. This solution is similar to the one proposed to Toulouse in the context of single-channel Kondo problem. Therefore, the solution is only valid only for $T \ll T_{2\mathrm{CK}}$ and $eV \ll T_{2\mathrm{CK}}$ and, because of that, cannot capture the Kondo peak splitting. Surprisingly, our results coincides with Emery-Kivelson solution up to $eV/T^* \approx 1$.

6 CONCLUSION

In the first part of the thesis, we have studied correlation effects in the emergence of a bound state in the continuum in a two identical quantum dot device coupled to a quantum wire. This experimental device is precisely modeled by the two-impurity Anderson Hamiltonian. Taking advantage of the quantum dot symmetry, we have projected the two-impurity Anderson model upon the bonding and antibonding representation given by the symmetric and antisymmetric linear combinations between the quantum dots. This representation has shown that the antibonding orbital is a Friedrich-Wintgen BIC in the non-interacting regime, but is effectively coupled to the continuum via isospin-isospin and spin-spin interactions with the bonding orbital for $\mathcal{U} > 0$.

To ratify the physical interpretation of the two-impurity Anderson Hamiltonian, we have calculated the spectral density and the magnetic susceptibility of the bonding and antibonding orbital via the Numerical Renormalization group approach. As the Coulomb interaction grows, we have shown that the spectral density of the antibonding orbital changes as a result of the indirect coupling of this orbital with the continuum. The coupling is assisted by the electron-electron interaction between the bonding and antibonding orbital. The antibonding orbital displayed threshold behavior in the weak and strong coupling regime that follows, respectively, the Nozières-De Dominicis and Doniach-Sunjic power laws. The threshold behavior indicates that the ground state of the system is composed by an isolated component of the antibonding orbital.

To examine the ground state properties of the system, we have studied the magnetic susceptibility of the two orbitals as a function of the temperature. At zero temperature, the magnetic susceptibility has unveiled a boundary quantum phase transition between a non-magnetic and magnetic phase. The phase transition is due to the competition between two ground states defined composed by a (i) singlet isospin state and (ii) a triplet spin state between the orbitals. The sudden change in the ground state is due to the conservation of the spin of the antibonding orbital.

In the non-magnetic phase the antibonding orbital has zero spin. Therefore, only the isospin-isospin interaction between the bonding and antibonding interaction acts on this subspace and the ground state is a isospin singlet. The magnetic phase arises when the ground state has the antibonding orbital with spin-1/2. As a result, only the ferromagnetic spin interaction acts in this subspace and the ground state is given by a triplet spin state. At zero temperature, a fixed point analysis has shown that the spin component of the antibonding orbital in the triplet spin state effectively coupled with the conduction band via a ferromagnetic interaction. As the ferromagnetic coupling goes to zero at zero temperature, the spin component of the antibonding orbital decouples from the continuum

and creates a spin-BIC at zero temperature.

These results shed light on the understanding of correlation effects in the emergence of BICs and unveil the emergence of a spin-BIC induced by strong correlation effects. Furthermore, they have shown another perspective in explaining the quantum phase transition present in two-impurity Anderson model. Finally, this project has allowed us to improve the spectral density calculation via z-interleaved approach.

In the second part of this thesis, we have investigated the non-equilibrium transport properties of the charge-degenerate two channel Kondo model. We have driven the system out of equilibrium due to a sudden applied bias voltage. Based on time-dependent Density Matrix Renormalization group, we have followed the time evolution long enough to describe the transient regime, although not long enough to reach the steady state. Even though we have not concluded this project yet, we have been able to capture: (i) the universal behavior of the charge-degenerate two-channel Kondo effect as a function of the bias voltage; (ii) the crossover between a Fermi liquid and non-Fermi liquid phase; (iii) the understanding of the time-dependent differential conductance via the energy-time uncertainty principle.

To conclude the second project, we will calculate and analyze the time-dependent differential conductance for finite bias voltage and asymmetry. Specifically, we intend to observe the universal crossover between a Fermi liquid and non-Fermi liquid phase due to the coupling asymmetry (ΔJ) and finite gate potential (V_g). In addition, we intend to use other time-dependent methods, such as time-dependent NRG, to describe the electronic properties in the steady state regime.

REFERENCES

1 IFTIKHAR, Z. *et al.* Two-channel kondo effect and renormalization flow with macroscopic quantum charge states. **Nature**, Nature Publishing Group, v. 526, p. 233, Oct. 2015. DOI: 10.1038/nature15384.

2 MITCHELL, A. K. *et al.* Universality and scaling in a charge two-channel kondo device. **Physical Review Letters**, American Physical Society, v. 116, n. 15, p. 157202, Apr. 2016.

3 ANDERSON, P. W. Localized magnetic states in metals. **Physical Review**, American Physical Society, v. 124, n. 1, p. 41–53, Oct. 1961.

4 KONDO, J. Resistance minimum in dilute magnetic alloys. **Progress of Theoretical Physics**, v. 32, n. 1, p. 37–49, July 1964.

5 GOLDHABER-GORDON, D. *et al.* Kondo effect in a single-electron transistor. **Nature**, v. 391, n. 6663, p. 156–159, Jan. 1998.

6 WIEL, W. G. van der *et al.* The kondo effect in the unitary limit. **Science**, v. 289, n. 5487, p. 2105–2108, Sept. 2000.

7 GROBIS, M. *et al.* Universal scaling in nonequilibrium transport through a single channel kondo dot. **Physical Review Letters**, American Physical Society, v. 100, n. 24, p. 246601, June 2008.

8 POTOK, R. M. *et al.* Observation of the two-channel kondo effect. **Nature**, Nature Publishing Group SN -, v. 446, p. 167 EP –, Mar. 2007. DOI: 10.1038/nature05556.

9 KELLER, A. J. *et al.* Universal fermi liquid crossover and quantum criticality in a mesoscopic system. **Nature**, v. 526, n. 7572, p. 237–240, Oct. 2015.

10 IFTIKHAR, Z. *et al.* Tunable quantum criticality and super-ballistic transport in a "charge" kondo circuit. **Science**, American Association for the Advancement of Science, v. 360, n. 6395, p. 1315–1320, May 2018.

11 FANO, U. Effects of configuration interaction on intensities and phase shifts. **Physical Review**, American Physical Society, v. 124, n. 6, p. 1866–1878, Dec. 1961.

12 MIROSHNICHENKO, A. E.; FLACH, S.; KIVSHAR, Y. S. Fano resonances in nanoscale structures. **Review Modern Physics**, American Physical Society, v. 82, n. 3, p. 2257–2298, Aug. 2010.

13 FRIEDRICH, H.; WINTGEN, D. Interfering resonances and bound states in the continuum. **Physical Review A**, American Physical Society, v. 32, n. 6, p. 3231–3242, Dec. 1985.

14 HSU, C. W. *et al.* Bound states in the continuum. **Nature Reviews Materials**, Springer Science and Business Media LLC, v. 1, n. 9, July 2016.

15 MATVEEV, K. A. Quantum fluctuations of the charge of a metal particle under the coulomb blockade conditions. **Journal of Experimental and Theoretical Physics**, ZhETF, v. 99, n. 5, p. 1598, May 1991.

16 SAKURAI, J. J.; NAPOLITANO, J. **Modern quantum mechanics.** 2nd ed. San Francisco, CA: Addison–Wesley, 2011.

17 COHEN-TANNOUDJI, C. *et al.* **Quantum mechanics**. New York: Wiley, 1977. v.1. (Wiley – Interscience publication).

18 GRIFFITHS, D. J.; SCHROETER, D. F. **Introduction to quantum mechanics**. Cambridge: Cambridge University Press, 2018.

19 BALLENTINE, L. **Quantum mechanics:** a modern development. New York: World Scientific, 1998.

20 NEUMANN, J. von; WIGNER, E. über merkwürdige diskrete eigenwerte. **Physikalische Zeitschrift**, v. 30, p. 465–467, 1929.

21 STILLINGER, F. H.; HERRICK, D. R. Bound states in the continuum. **Physical Review A**, American Physical Society, v. 11, n. 2, p. 446–454, Feb. 1975.

22 HERRICK, D. R. Construction of bound states in the continuum for epitaxial heterostructure superlattices. **Physica B+C**, Elsevier BV, v. 85, n. 1, p. 44–50, Nov. 1976.

23 STILLINGER, F. Potentials supporting positive-energy eigenstates and their application to semiconductor heterostructures. **Physica B+C**, Elsevier BV, v. 85, n. 2, p. 270–276, Dec. 1976.

24 CAPASSO, F. *et al.* Observation of an electronic bound state above a potential well. **Nature**, v. 358, n. 6387, p. 565–567, Aug. 1992.

25 COBELLI, P. J. *et al.* Experimental observation of trapped modes in a water wave channel. **Europhysics Letters**, IOP Publishing, v. 88, n. 2, p. 20006, Oct. 2009.

26 LINTON, C.; MCIVER, P. Embedded trapped modes in water waves and acoustics. **Wave Motion**, Elsevier BV, v. 45, n. 1-2, p. 16–29, Nov. 2007.

27 VOO, K.-K. Trapped electromagnetic modes in forked transmission lines. **Wave Motion**, Elsevier BV, v. 45, n. 6, p. 795–803, June 2008.

28 HSU, C. W. *et al.* Observation of trapped light within the radiation continuum. **Nature**, v. 499, n. 7457, p. 188–191, July 2013.

29 SADRIEVA, Z. *et al.* Multipolar origin of bound states in the continuum. **Physical Review B**, American Physical Society, v. 100, n. 11, p. 115303, Sept. 2019.

30 JAIN, A.; SHASTRY, C. Study of theS-matrix near bound states in the continuum. **Pramana**, Springer Science and Business Media LLC, v. 9, n. 3, p. 311–320, Sept. 1977.

31 GUESSI, L. H. *et al.* Catching the bound states in the continuum of a phantom atom in graphene. **Physical Review B**, American Physical Society, v. 92, n. 4, p. 045409, July 2015.

32 GUESSI, L. H. *et al.* Quantum phase transition triggering magnetic bound states in the continuum in graphene. **Physical Review B**, American Physical Society, v. 92, n. 24, p. 245107, Dec. 2015.

33 AZZAM, S. I.; KILDISHEV, A. V. Photonic bound states in the continuum: from basics to applications. **Advanced Optical Materials**, Wiley, v. 9, n. 1, p. 2001469, Nov. 2020.

34 KOSHELEV, K.; BOGDANOV, A.; KIVSHAR, Y. Engineering with bound states in the continuum. **Optics and Photonics News**, The Optical Society, v. 31, n. 1, p. 38, Jan. 2020.

35 HUANG, L. *et al.* Trends in quantum nanophotonics. **Advanced Quantum Technologies**, Wiley, v. 3, n. 4, p. 1900126, Apr. 2020.

36 JEONG, K.-Y. *et al.* Recent progress in nanolaser technology. **Advanced Materials**, Wiley, v. 32, n. 51, p. 2001996, Sept. 2020.

37 RICCO, L. S. *et al.* Decay of bound states in the continuum of majorana fermions induced by vacuum fluctuations: Proposal of qubit technology. **Physical Review B**, American Physical Society, v. 93, n. 16, p. 165116, Apr. 2016.

38 MARQUES, Y. *et al.* Antibonding ground state of adatom molecules in bulk dirac semimetals. **Physical Review B**, American Physical Society, v. 96, n. 4, p. 041112, July 2017.

39 GUESSI, L. H. *et al.* Encrypting majorana fermion qubits as bound states in the continuum. **Physical Review B**, American Physical Society, v. 96, n. 4, p. 041114, July 2017.

40 GONZÁLEZ, J. W. *et al.* Bound states in the continuum in graphene quantum dot structures. **Europhysics Letters**, IOP Publishing, v. 91, n. 6, p. 66001, Sept. 2010.

41 VALLEJO, M.; GUEVARA, M. L. de; ORELLANA, P. Triple rashba dots as a spin filter: Bound states in the continuum and fano effect. **Physics Letters A**, Elsevier BV, v. 374, n. 48, p. 4928–4932, Nov. 2010.

42 GUEVARA, M. L. Ladrón de; ORELLANA, P. A. Electronic transport through a parallel-coupled triple quantum dot molecule: fano resonances and bound states in the continuum. **Physical Review B**, American Physical Society, v. 73, n. 20, p. 205303, May 2006.

43 RAMOS-ANDRADE, J. P.; ORELLANA, P. A.; VERNEK, E. Majorana bound state in the continuum: coupling between a majorana bound state and a quantum dot mediated by a continuum energy spectrum. **Physical Review B**, American Physical Society, v. 101, n. 11, p. 115403, Mar. 2020.

44 ŽITKO, R.; MRAVLJE, J.; HAULE, K. Ground state of the parallel double quantum dot system. **Physical Review Letters**, American Physical Society, v. 108, n. 6, p. 066602, Feb. 2012.

45 SACHDEV, S. **Quantum phase transitions**. Cambridge: Cambridge University Press, 2009.

46 CARR, L. (ed.). **Understanding quantum phase transitions**. Boca Raton: CRC Press, 2010.

47 SELA, E. *et al.* Fractional shot noise in the kondo regime. **Physical Review Letters**, American Physical Society, v. 97, n. 8, p. 086601, Aug. 2006.

48 PICCIOTTO, R. de *et al.* Direct observation of a fractional charge. **Nature**, Springer Nature, v. 389, n. 6647, p. 162–164, Sept. 1997.

49 SAMINADAYAR, L. *et al.* Observation of the $e/3$ fractionally charged laughlin quasiparticle. **Physical Review Letters**, American Physical Society, v. 79, n. 13, p. 2526–2529, Sept. 1997.

50 LEFLOCH, F. *et al.* Doubled full shot noise in quantum coherent superconductor-semiconductor junctions. **Physical Review Letters**, American Physical Society, v. 90, n. 6, p. 067002, Feb. 2003.

51 NOZIÈRES, P.; BLANDIN, A. Kondo effect in real metals. **Journal De Physique**, v. 41, n. 3, p. 193–211, 1980.

52 COX, D. L.; ZAWADOWSKI, A. Exotic kondo effects in metals: magnetic ions in a crystalline electric field and tunnelling centres. **Advances in Physics**, Informa UK Limited, v. 47, n. 5, p. 599–942, Sept. 1998.

53 HEWSON, A. C. **The Kondo problem to heavy fermions**. Cambridge: Cambridge University Press, 1993. (Cambridge studies in magnetism).

54 VOJTA, M.; BULLA, R.; HOFSTETTER, W. Quantum phase transitions in models of coupled magnetic impurities. **Physical Review B**, American Physical Society, v. 65, n. 14, p. 140405, Apr. 2002.

55 VOJTA, M. Impurity quantum phase transitions. **Philosophical Magazine**, Informa UK Limited, v. 86, n. 13-14, p. 1807–1846, May 2006.

56 COLEMAN, P.; IOFFE, L. B.; TSVELIK, A. M. Simple formulation of the two-channel kondo model. **Physical Review B**, American Physical Society, v. 52, n. 9, p. 6611–6627, Sept. 1995.

57 LANDAU, L. A.; CORNFELD, E.; SELA, E. Charge fractionalization in the two-channel kondo effect. **Physical Review Letters**, American Physical Society, v. 120, n. 18, p. 186801, May 2018.

58 EMERY, V. J.; KIVELSON, S. Mapping of the two-channel kondo problem to a resonant-level model. **Physical Review B**, American Physical Society, v. 46, n. 17, p. 10812–10817, Nov. 1992.

59 CRONENWETT, S. M.; OOSTERKAMP, T. H.; KOUWENHOVEN, L. P. A tunable kondo effect in quantum dots. **Science**, American Association for the Advancement of Science, v. 281, n. 5376, p. 540–544, 1998.

60 KOUWENHOVEN, L.; GLAZMAN, L. Revival of the kondo effect. **Physics World**, IOP Publishing, v. 14, n. 1, p. 33–38, Jan. 2001.

61 OREG, Y.; GOLDHABER-GORDON, D. Two-channel kondo effect in a modified single electron transistor. **Physical Review Letters**, American Physical Society, v. 90, n. 13, p. 136602, Apr. 2003.

62 TARAPHDER, A.; COLEMAN, P. Heavy-fermion behavior in a negative-u anderson model. **Physical Review Letters**, American Physical Society, v. 66, n. 21, p. 2814–2817, May 1991.

63 PUSTILNIK, M.; GLAZMAN, L. I. Kondo effect induced by a magnetic field. **Physical Review B**, American Physical Society, v. 64, n. 4, p. 045328, July 2001.

64 KELLER, A. J. *et al.* Emergent SU(4) kondo physics in a spin–charge-entangled double quantum dot. **Nature Physics**, v. 10, n. 2, p. 145–150, Dec. 2013.

65 MAKAROVSKI, A. *et al.* Su(2) and su(4) kondo effects in carbon nanotube quantum dots. **Physical Review B**, American Physical Society, v. 75, n. 24, p. 241407, June 2007.

66 FURUSAKI, A.; MATVEEV, K. A. Theory of strong inelastic cotunneling. **Physical Review B**, American Physical Society, v. 52, n. 23, p. 16676–16695, Dec. 1995.

67 MATVEEV, K. A. Coulomb blockade at almost perfect transmission. **Physical Review B**, American Physical Society, v. 51, n. 3, p. 1743–1751, Jan. 1995.

68 MATVEEV, K. A. Quantum smearing of coulomb blockade. *In*: KULIK, I. O.; ELLIALTIOGLU, R. **Quantum mesoscopic phenomena and mesoscopic devices in microelectronics**. Netherlands: Springer, 2000. p. 129–143.

69 MITCHELL, A. K. *et al.* Universality and scaling in a charge two-channel kondo device. **Physical Review Letters**, American Physical Society, v. 116, n. 15, p. 157202, Apr. 2016.

70 DALUM, G. A. R. van; MITCHELL, A. K.; FRITZ, L. Electric and heat transport in a charge two-channel kondo device. **Physical Review B**, American Physical Society, v. 102, n. 20, p. 205137, Nov. 2020.

71 SCHILLER, A.; HERSHFIELD, S. Exactly solvable nonequilibrium kondo problem. **Physical Review B**, American Physical Society, v. 51, n. 18, p. 12896–12899, May 1995.

72 SCHILLER, A.; HERSHFIELD, S. Toulouse limit for the nonequilibrium kondo impurity: currents, noise spectra, and magnetic properties. **Physical Review B**, American Physical Society, v. 58, n. 22, p. 14978–15010, Dec. 1998.

73 SCHILLER, A.; HERSHFIELD, S. Out-of-equilibrium kondo effect: response to pulsed fields. **Physical Review B**, American Physical Society, v. 62, n. 24, p. R16271–R16274, Dec. 2000.

74 MAJUMDAR, K.; SCHILLER, A.; HERSHFIELD, S. Nonequilibrium kondo impurity: perturbation about an exactly solvable point. **Physical Review B**, American Physical Society, v. 57, n. 5, p. 2991–2999, Feb. 1998.

75 SCHOLLWÖCK, U. The density-matrix renormalization group. **Review Modern Physics**, American Physical Society, v. 77, n. 1, p. 259–315, Apr. 2005.

76 SCHOLLWöCK, U. The density-matrix renormalization group in the age of matrix product states. **Annals of Physics**, Elsevier BV, v. 326, n. 1, p. 96–192, Jan. 2011.

77 ASHIDA, Y. *et al.* Variational principle for quantum impurity systems in and out of equilibrium: application to kondo problems. **Physical Review B**, American Physical Society, v. 98, n. 2, p. 024103, July 2018.

78 SILVA, L. G. G. V. Dias da *et al.* Transport properties and kondo correlations in nanostructures: time-dependent dmrg method applied to quantum dots coupled to wilson chains. **Physical Review B**, American Physical Society, v. 78, n. 19, p. 195317, Nov. 2008.

79 HAAS, W. J. de; BOER, J. de; BERG, G. J. van dën. The electrical resistance of gold, copper and lead at low temperatures. **Physica**, v. 1, n. 7, p. 1115–1124, May 1934.

80 SARACHIK, M. P.; CORENZWIT, E.; LONGINOTTI, L. D. Resistivity of mo-nb and mo-re alloys containing 1% fe. **Physical Review**, American Physical Society, v. 135, n. 4A, p. A1041–A1045, Aug. 1964.

81 WILSON, K. G. The renormalization group: Critical phenomena and the kondo problem. **Review Modern Physics**, American Physical Society, v. 47, n. 4, p. 773–840, Oct. 1975.

82 ANDREI, N.; FURUYA, K.; LOWENSTEIN, J. H. Solution of the kondo problem. **Review Modern Physics**, American Physical Society, v. 55, n. 2, p. 331–402, Apr. 1983.

83 AFFLECK, I.; LUDWIG, A. W. W. Exact conformal-field-theory results on the multichannel kondo effect: single-fermion green's function, self-energy, and resistivity. **Physical Review B**, American Physical Society, v. 48, n. 10, p. 7297–7321, Sept. 1993.

84 EMERY, V. J.; KIVELSON, S. Mapping of the two-channel kondo problem to a resonant-level model. **Physical Review B**, American Physical Society, v. 46, n. 17, p. 10812–10817, Nov. 1992.

85 GOGOLIN, A.; NERSESYAN, A.; TSVELIK, A. **Bosonization and strongly correlated systems**. Cambridge: Cambridge University Press, 2004. ISBN 9780521617192.

86 NOZIÉRES, P. A "fermi-liquid" description of the kondo problem at low temperatures. **Journal of Low Temperature Physics**, Springer Science and Business Media LLC, v. 17, n. 1-2, p. 31–42, Oct. 1974.

87 TERNES, M.; HEINRICH, A. J.; SCHNEIDER, W.-D. Spectroscopic manifestations of the kondo effect on single adatoms. **Journal of Physics:** condensed matter, IOP Publishing, v. 21, n. 5, p. 053001, Dec. 2008.

88 ANDERSON, P. W. A poor man's derivation of scaling laws for the kondo problem. **Journal of Physics C:** solid state physics, IOP Publishing, v. 3, n. 12, p. 2436–2441, Dec. 1970.

89 SCHRIEFFER, J. R.; WOLFF, P. A. Relation between the anderson and kondo hamiltonians. **Physical Review**, American Physical Society, v. 149, n. 2, p. 491–492, Sept. 1966.

90 ŽITKO, R.; BONČA, J. Multiple-impurity anderson model for quantum dots coupled in parallel. **Physical Review B**, American Physical Society, v. 74, n. 4, p. 045312, July 2006.

91 JONES, B. A.; VARMA, C. M.; WILKINS, J. W. Low-temperature properties of the two-impurity kondo hamiltonian. **Physical Review Letters**, American Physical Society, v. 61, n. 1, p. 125–128, July 1988.

92 SILVA, J. B. *et al.* Particle-hole asymmetry in the two-impurity kondo model. **Physical Review Letters**, American Physical Society, v. 76, n. 2, p. 275–278, Jan. 1996.

93 CAMPO, V. L.; OLIVEIRA, L. N. Thermodynamics for the two-impurity kondo model. **Physical Review B**, American Physical Society, v. 70, n. 15, p. 153401, Oct. 2004.

94 MITCHELL, A. K.; SELA, E. Universal low-temperature crossover in two-channel kondo models. **Physical Review B**, American Physical Society, v. 85, n. 23, p. 235127, June 2012.

95 KRISHNA-MURTHY, H. R.; WILKINS, J. W.; WILSON, K. G. Renormalization-group approach to the anderson model of dilute magnetic alloys. i. static properties for the symmetric case. **Physical Review B**, American Physical Society, v. 21, n. 3, p. 1003–1043, Feb. 1980.

96 BULLA, R.; COSTI, T. A.; PRUSCHKE, T. Numerical renormalization group method for quantum impurity systems. **Review Modern Physics**, American Physical Society, v. 80, n. 2, p. 395–450, Apr. 2008.

97 PINTO, J. W. M.; OLIVEIRA, L. N. Recursive computation of matrix elements in the numerical renormalization group. **Computer Physics Communications**, Elsevier BV, v. 185, n. 4, p. 1299–1309, Apr. 2014.

98 YOSHIDA, M.; WHITAKER, M. A.; OLIVEIRA, L. N. Renormalization-group calculation of excitation properties for impurity models. **Physical Review B**, American Physical Society, v. 41, n. 13, p. 9403–9414, May 1990.

99 CAMPO, V. L.; OLIVEIRA, L. N. Alternative discretization in the numerical renormalization-group method. **Physical Review B**, American Physical Society, v. 72, n. 10, p. 104432, Sept. 2005.

100 OLIVEIRA, W. C.; OLIVEIRA, L. N. Generalized numerical renormalization-group method to calculate the thermodynamical properties of impurities in metals. **Physical Review B**, American Physical Society, v. 49, n. 17, p. 11986–11994, May. 1994.

101 ROSCH, A. Wilson chains are not thermal reservoirs. **The European Physical Journal B**, Springer Science and Business Media LLC, v. 85, n. 1, Jan. 2012.

102 WHITE, S. R.; NOACK, R. M. Real-space quantum renormalization groups. **Physical Review Letters**, American Physical Society, v. 68, n. 24, p. 3487–3490, June 1992.

103 WHITE, S. R. Density matrix formulation for quantum renormalization groups. **Physical Review Letters**, American Physical Society, v. 69, n. 19, p. 2863–2866, Nov. 1992.

104 HALDANE, F. D. M. Scaling theory of the asymmetric anderson model. **Physical Review Letters**, American Physical Society, v. 40, n. 6, p. 416–419, Feb. 1978.

105 VOJTA, M. Quantum phase transitions. **Reports on Progress in Physics**, IOP Publishing, v. 66, n. 12, p. 2069–2110, Nov. 2003.

106 PUSTILNIK, M. *et al.* Quantum phase transition in a two-channel-kondo quantum dot device. **Physical Review B**, American Physical Society, v. 69, n. 11, p. 115316, Mar. 2004.

107 TSVELICK, A.; WIEGMANN, P. Exact results in the theory of magnetic alloys. **Advances in Physics**, Informa UK Limited, v. 32, n. 4, p. 453–713, Jan. 1983.

Appendix

APPENDIX A – UNIVERSAL MAGNETIC SUSCEPTIBILITY

This appendix shows the numerical data for the universal magnetic susceptibility for the spin-1 and one channel Kondo effect, used in Chapter 4.

Table 7 – Values of the universal magnetic susceptibility of the spin-1 and one channel Kondo effect versus T/T_K.

$\ln T/T_K$	T/T_K	$S = 1$
-6.6	0.0013	213.02547
-6.3	0.0018	158.47150
-6.0	0.0024	117.95038
-5.7	0.0033	87.84407
-5.1	0.0045	65.46840
-4.8	0.0082	36.45573
-4.5	0.0111	27.24411
-4.2	0.0149	20.38286
-3.9	0.0202	15.26821
-3.6	0.0273	11.45817
-3.3	0.0368	8.60222
-3.0	0.0497	6.47145
-2.7	0.0672	4.87638
-2.4	0.0907	3.68064
-2.1	0.1224	2.78280
-1.8	0.1652	2.10739
-1.5	0.2231	1.59830
-1.2	0.3011	1.21377
-0.9	0.4065	0.92269
-0.6	0.5488	0.70189
-0.3	0.7408	0.53409
0.0	1.0000	0.40637
0.3	1.3498	0.30906
0.6	1.8221	0.23488
0.9	2.4596	0.17833
1.2	3.3201	0.13523
1.5	4.4816	0.10242
1.8	6.0496	0.07746
2.1	8.1661	0.05850
2.4	11.0231	0.04412
2.7	14.8797	0.03323
3.0	20.0855	0.02500
3.3	27.1126	0.01878
3.6	36.5982	0.01409
3.9	49.4024	0.01056
4.2	66.6863	0.00791
4.5	90.0171	0.00592
4.8	121.5104	0.00442
5.1	164.0219	0.00330
5.4	221.4064	0.00246
5.7	298.8674	0.00184
6.0	403.4287	0.00137
6.3	544.5719	0.00102
6.6	735.0951	0.00070

Source: Adapted from TSVELICK, A. *et al.*[107]